ADVANCEMENTS IN NAVIGATION OF UNTETHERED SMALL-SCALE HELICAL DEVICES

Chuang Li

university of groningen

Advancements in Navigation of Untethered Small-Scale Helical Devices

PhD thesis

to obtain the degree of PhD at the
University of Groningen
on the authority of the
Rector Magnificus Prof. J.M.A. Scherpen
and in accordance with
the decision by the College of Deans.
This thesis will be defended in public
on xxxxxxx the xxth of March 2024 at xx.xx hours

by

Chuang Li

born on the 15th of December 1992
in Liaoning, China

Graduation Committee:

Promoter:

Prof. Dr. S. Misra	*University of Groningen* *and University Medical Center Groningen* *University of Twente*

Supervisor:

Dr. I. S. M. Khalil	*University of Twente*

Assessment Committee:

Prof. Dr. R. Schirhagl	*University of Groningen* *and University Medical Center Groningen*
Prof. Dr. S. Yin	*Norwegian University of Science and Technology*
Prof. Dr. X. Yang	*Harbin Institute of Technology*

This work is part of the research project MAESTRO.

This work was supported by the European Research Council (ERC) under the European Union's Horizon 2020 Research and Innovation programme under grant 866494 project-MAESTRO, and financial support from the China Scholarship Council (CSC No. 201908210341) is acknowledged.

This dissertation has been approved by:

Prof. Dr. Sarthak Misra
Dr. Islam S. M. Khalil

Cover design: Chuang Li
Lay-out: Sumit Mohanty
Printed by: Ipskamp
ISBN: xxx-xx-xxx-xxxx-x

In memory of my grandparents

Samenvatting

Vasculaire ziekten hebben een diepgaande invloed op de menselijke gezondheid en vormen aanzienlijke uitdagingen voor zowel patiënten als zorgverleners. Deze ziekten kunnen leiden tot complicaties zoals arteriële blokkades, aneurysma's en vasculaire misvormingen die levensbedreigende risico's kunnen vormen als ze niet effectief worden behandeld. Conventionele behandelingsbenaderingen omvatten vaak invasieve procedures, die niet alleen inherente risico's met zich meebrengen, maar ook lange herstelperiodes met zich meebrengen. Met de voortdurende vooruitgang van de wetenschap en technologie hebben magnetische helicale apparaten (MHAen) een groot potentieel als een minimaal invasief chirurgisch hulpmiddel voor de behandeling van vasculaire ziekten. Door minimaal invasieve ingrepen, precisie-navigatie, real-time beeldvorming en uitgebreide behandelingsmogelijkheden te combineren, hebben MHAen het potentieel om het veld van vasculaire geneeskunde te veranderen, de resultaten voor patiënten te verbeteren en de last die gepaard gaat met vasculaire ziekten te verminderen. Er blijven echter tal van uitdagingen bestaan in de medische toepassingen van MHAen. Bijvoorbeeld, de variaties in bloedstroomsnelheden als gevolg van verschillende segmenten van bloedvaten of variërende diameters van bloedvaten kunnen onzekere effecten hebben op de beweging en navigatie van de MHA binnen het circulatiesysteem. Daarom is het begrijpen van de implicaties van variërende bloedstroomsnelheden voor de bewegingscontrole van MHAen van cruciaal belang voor toekomstige ontwikkelingen in medische toepassingen. Bovendien vertonen bloedvaten heterogeniteit in hun geometrie, diameter en vertakkingspatronen. Navigeren door dergelijke complexe en diverse vasculaire structuren stelt uitdagingen aan het nauwkeurig lokaliseren en besturen van de MHA binnen de vasculaire netwerken. Daarom is het de moeite waard om een effectieve en stabiele besturingsmethode te verkennen die de veiligheid van het menselijk lichaam tijdens de bewegingscontrole van MHAen in de bloedvaten waarborgt.

Het belangrijkste doel van dit promotie onderzoek is de bewegingsbesturing van niet-verbonden kleine helicale apparaten (NKHAen) binnen bloedvatfantomen met dynamische stroomsnelheden. **Hoofdstuk 1** begint met een introductie over de ontwikkeling van MHAen en de medische

toepassingen ervan en bespreekt de uitdagingen in de medische toepassingen. Vervolgens worden de onderzoeksdoelstellingen en de lijst van publicaties die voortvloeien uit dit onderzoek beschreven. Bovendien onderzoeken we eerst de helicale voortstuwing van de NKHA binnen het bloedvatfantoom met verschillende stroomsnelheden. **Hoofdstuk 2** presenteert het aantrekkingsgebied van een NKHA aangedreven door twee gesynchroniseerde roterende permanente magneten binnen een met vloeistof gevulde lumen rond een evenwichtspunt. Het hydrodynamische model van een magnetisch aangedreven NKHA wordt gepresenteerd, dat het gedrag ervan tegen de stroming van bloedserum beschrijft. Vervolgens wordt het model gevalideerd via 1-D frequentieresponskarakterisering, waarbij wordt aangetoond dat het in staat is de gemeten lineaire relatie tussen de aandrijffrequentie en de voortstuwingskracht over verschillende stroomvelden vast te leggen.

Na het onderzoek naar de spiraalvormige voortstuwing van de NKHA concentreren we ons op het onderzoek naar echogeleide gesloten lusbewegingscontrole van de NKHA in een vasculair model met een dynamische stroomsnelheid. **Hoofdstuk 3** omvat het modelleren, ontwerpen van een robotsysteem met permanente magneten (PMR), het vaststellen van een aantrekkingsgebied en het implementeren van een gesloten regelstrategie gebaseerd op ultrasone feedback voor de NKHA in dynamische stroming. Bovendien demonstreert het de gesloten-luscontrolekarakterisering van de NKHA tegen en langs fysiologische vloeistof in een 1-D bloedvatfantoom op verschillende penetratiediepten en een bloedvatfantoom met een vertakking. Anders dan **Hoofdstuk 3**, betreft **Hoofdstuk 4** de controle van de NKHA binnen een 3D-vasculair model dat anatomische structuren nauwkeurig weergeeft. **Hoofdstuk 4** is ook gebaseerd op echografie: De gesloten-lus bewegingscontrole van de NKHA, aangestuurd door het PMR-systeem, wordt in het 3D-vasculaire model met dynamische bloedstroom uitgevoerd. Eerst wordt een 3D-vasculair model geconstrueerd door gebruik te maken van de 2D-echografiebeelden, en de waypoints van het 3D-vasculaire modelpad worden verschaft als referentiepaden van de NKHA. Vervolgens wordt een controlemethode met robuustheid geconstrueerd met behulp van het PMR-systeem onder echografie. De voorgestelde aanpak is in staat om de NKHA door complexe en kronkelende paden van het 3D-vasculaire model te sturen om de doelpositie te bereiken. Ten slotte evalueert dit werk de voortbewegingsprestaties van de NKHA binnen het

3D-vasculaire model onder verschillende bloedstroomsnelheden. Deze beoordeling biedt inzicht in het gedrag van de NKHA onder verschillende stromingsomstandigheden. Deze bijdrage vergroot ook ons begrip van de mogelijkheden en beperkingen van de voorgestelde controlemethode.

Ter afsluiting van dit proefschrift bespreken we de resultaten van de drie onderzoeken die in dit onderzoek zijn uitgevoerd die worden behandeld in **Hoofdstukken 2-4**. **Hoofdstuk 5** begint met het uiteenzetten van de conclusies en concentreert zich op drie hoofdthema's: 1) optimalisatie van het aandrijfsysteem, 2) biologische afbreekbaarheid en veiligheid, 3) *ex vivo* en *in vivo* experimenten. Ten slotte worden aanwijzingen voor toekomstig onderzoek en een vooruitblik gegeven. Hoewel de reikwijdte van dit doctoraatsonderzoek beperkt is tot laboratoriumexperimenten, maakt het de weg vrij weg voor toekomstige *ex vivo* en *in vivo* experimenten. Bovendien legt het de basis voor toekomstige medische toepassingen.

Summary

Vascular diseases have a profound impact on human health, presenting considerable challenges for patients and healthcare providers alike. These diseases can lead to complications such as arterial blockages, aneurysms, and vascular malformations, which can pose life-threatening risks if not effectively treated. Conventional treatment approaches often involve invasive procedures, which not only carry inherent risks but also entail lengthy recovery periods. With the continuous advancements in science and technology, magnetic helical devices (MHDs) hold great potential as a minimally invasive surgical tool for treating vascular diseases. By combining minimally invasive interventions, precision navigation, real-time imaging, and expanded treatment options, MHDs have the potential to change the field of vascular medicine, improving patient outcomes and reducing the burden associated with vascular diseases. However, numerous challenges persist in the medical applications of MHDs. For instance, the variations in blood flow velocities resulting from different segments of blood vessels or varying diameters of blood vessels can have uncertain effects on the movement and navigation of the MHD inside the circulatory system. As a result, understanding the implications of varying blood flow velocities on motion control of MHDs is paramount for future advancements in medical applications. In addition, blood vessels exhibit heterogeneity in their geometry, diameter, and branching patterns. Navigating through such complex and diverse vascular structures poses challenges in accurately localizing and driving the MHD inside the vascular networks. Hence, it is worthwhile to explore an effective and stable control method that ensures the safety of the human body during motion control of MHDs inside the blood vessel.

The main objective of this doctoral research is the motion control of untethered small-scale helical devices (USHDs) inside blood vessel phantoms with dynamic flow rates. **Chapter 1** begins by introducing the development of MHDs, and the medical applications of MHDs, and discusses the challenges in the medical applications. Then the research objectives and the list of publications resulting from this research are then described. Furthermore, we first investigate the helical propulsion of the USHD inside the blood vessel phantom with different flow rates. **Chapter 2** presents the

region of attraction of a USHD driven by two synchronized rotating permanent magnets inside a fluid-filled lumen around an equilibrium point. The hydrodynamic model of a magnetically-driven USHD is presented, which describes its behavior against the flow of blood serum. Subsequently, the model is validated through 1-D frequency response characterization, demonstrating its ability to capture the measured linear relationship between the actuation frequency and propulsive thrust across different flow fields.

Following the research on the helical propulsion of the USHD, we focus on the investigation of ultrasound-guided closed-loop motion control of the USHD inside a vascular model with a dynamic flow rate. **Chapter 3** involves modeling, designing a permanent-magnet robotic (PMR) system, establishing a region of attraction, and implementing a closed-loop control strategy based on ultrasound feedback for the USHD in dynamic flow. Additionally, it demonstrates closed-loop control characterization of the USHD against and along physiological fluid inside a 1-D blood vessel phantom at different penetration depths and a blood vessel phantom with a bifurcation. Different from **Chapter 3**, **Chapter 4** involves the control of the USHD inside a 3-D vascular model that accurately represents anatomical structures. **Chapter 4** is also based on ultrasound guidance, the closed-loop motion control of the USHD driven by the PMR system in the 3-D vascular model with dynamic blood flow is performed. First, a 3-D vascular model is constructed by utilizing the 2-D ultrasound images, and waypoints of the 3-D vascular model path are provided as reference paths of the USHD. Next, a control method with robustness is constructed using the PMR system under ultrasound guidance, and the proposed approach is able to drive the USHD through complex and winding paths of the 3-D vascular model to reach the target position. Lastly, this work evaluates the locomotion performance of the USHD inside the 3-D vascular model under various blood flow velocities. This assessment offers insights into the behavior of the USHD under various flow conditions. This contribution also enhances our understanding of the capabilities and limitations of the proposed control method.

To conclude this doctoral thesis, we discuss the results of the three studies conducted in this research, which are covered in **Chapters 2-4**. **Chapter 5** begins by laying out the conclusions and focusing on three key themes: 1) actuation system optimization, 2) biodegradability and safety,

3) *ex vivo* and *in vivo* experiments. Finally, directions on future research and an outlook are provided. While the scope of this doctoral research is limited to laboratory experiments, it paves the way for future *ex vivo* and *in vivo* experiments. Furthermore, it lays the foundation for future medical applications.

Contents

1

Introduction

Vascular diseases, such as atherosclerosis, thrombosis, and aneurysms, pose significant challenges in healthcare due to their prevalence and potentially life-threatening consequences [1]–[4]. These diseases affect the blood vessels, leading to restricted blood flow, clot formation, and structural abnormalities. Conventional treatments for vascular diseases often involve invasive procedures such as angioplasty, stent placement, or open-heart surgery

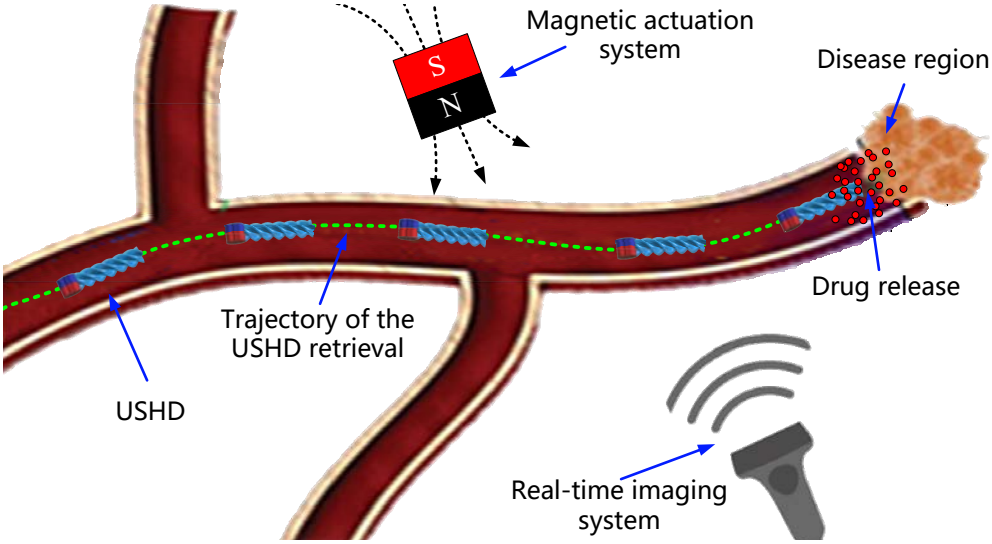

Figure 1.1: The untethered small-scale helical device (USHD) is driven through a magnetic actuation system to reach the disease region to release drugs, and a real-time imaging system can be utilized to track the position of the USHD.

[5]–[8]. However, these interventions carry risks and may not always be feasible for patients with complex vascular conditions. Therefore, in the past few decades, the emergence of micro- or small-scale robotic technology has provided a promising avenue for addressing these challenges [9]–[16], as shown in Fig. 1.1. Because of the complex and dynamic nature of human vasculature, researchers have been developing miniature robots capable of navigating through the intricate network of blood vessels with precision and delivering targeted interventions directly at the site of the disease. The goal of this doctoral research is to develop a closed-loop control system that can control the untethered small-scale helical device (USHD) to navigate inside the vascular model. This chapter begins with the development of magnetic helical devices (MHDs), followed by the introduction of biomedical applications and the associated challenges. Thereafter, research objectives are presented and analyzed, and a list of publications is provided that resulted as part of this doctoral study.

1.1 Development of the Magnetic Helical Device

Taking inspiration from the behaviors and functions observed in biological active matter found in nature, such as motor proteins, bacteria (Fig. 1.2(A,B)), and sperm, researchers have developed both rigid and soft devices capable of performing a wide range of tasks [17]–[25]. These devices have been designed to mimic and replicate the remarkable capabilities exhibited by living organisms. These devices, whether rigid or soft, have been developed across different scales to fulfill various tasks in fields such as healthcare, manufacturing, exploration, and environmental monitoring [26]–[28]. By drawing inspiration from the biological world, researchers have leveraged the unique characteristics and functionalities observed to create innovative robotic systems for medical applications.

Among them, MHDs have shown great promise in medical applications. Their ability to navigate through complex anatomical structures, such as water, blood, or urine, to more complex environments, such as cerebrospinal fluids, gastrointestinal tract, or brain matter, offers the potential for minimally invasive procedures. As a result, these devices have the potential for delivering targeted therapies, performing precise surgeries, assisting in diagnostics, reducing patient trauma, and improving treatment outcomes [31]–[33]. In order to realize these medical applications, researchers have

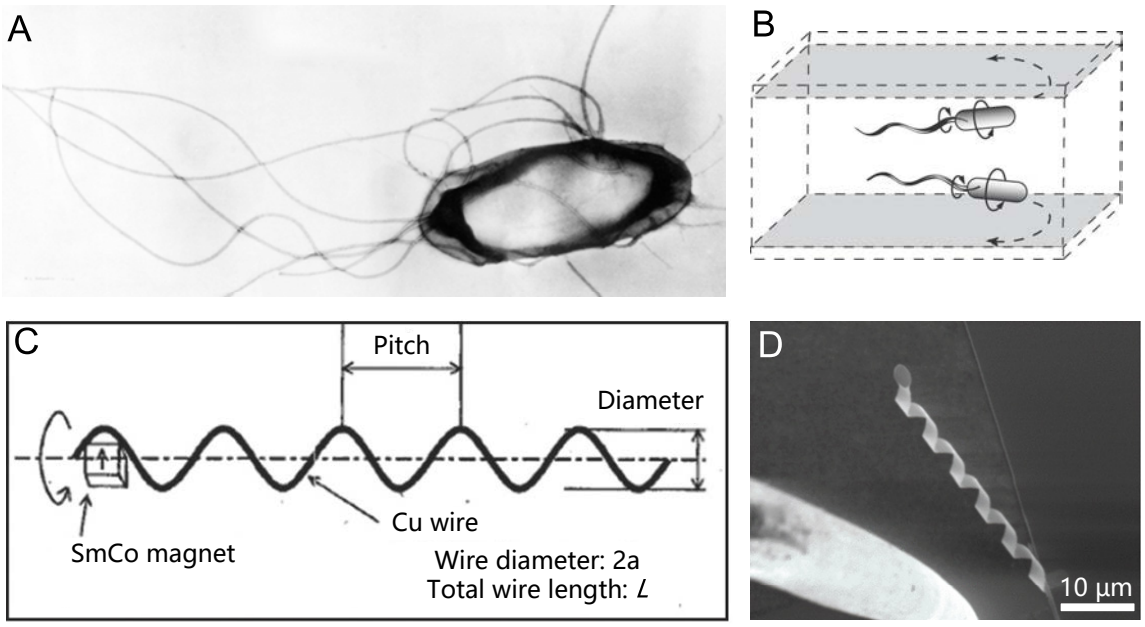

Figure 1.2: Helical propulsion. (A) The optical image of an Escherichia coli bacteria [17]. (B) Escherichia coli bacteria can swim by rotating its flagella in a helical wave [18]. (C) The first prototype of a magnetic helical device (MHD) on a centimeter scale [29]. (D) The first microscale prototype of the MHD [30].

done a lot of research on MHDs. For instance, in 1996, the first magnetically actuated helical prototype in the millimeter range has been presented by Honda *et al.* from Tohoku University, as shown in Fig. 1.2(C) [29]. They have published numerous papers demonstrating the application of these helices or screw-type structures in muscle tissue or inside the gastrointestinal tract [34], [35]. In 2007, Nelson *et al.* have presented a novel propulsion system for microrobots (Fig. 1.2(D)) that mimics the size and motion of bacterial flagella [30]. This system comprised a magnetic nanocoil and a configuration of macro coils used to generate electromagnetic fields. Since then, MHDs have garnered significant attention and have been the subject of extensive research by numerous research groups [36]–[43]. In order to improve the swimming performance of the MHD, the geometry of the MHD has been extensively studied [44]–[57]. Moreover, during the swimming of the MHD, an open-loop algorithm for velocity control with gravity compensation has been presented for the MHD [58]. This algorithm allowed a human operator or automated controller to intuitively command

the desired velocity of the MHD, instead of directly controlling its orientation and rotation speed. In addition, modeling and simulation based on the resistive force theory [59] have been presented for the MHD when it swims inside channel flow. This modeling considered various forces on the MHD, including propulsive thrust, hydrodynamic drag, contact force, and the force due to gravity [60], [61].

As the theory of the MHD continues to evolve and refine, significant progress has been achieved in various research aspects. These research efforts have expanded the possibilities for the application of MHDs and have driven the development of micro- and small-scale MHD technology. The outcomes of these studies have provided a greater understanding of MHD dynamics and control methods. This, in turn, has paved the way for enhanced capabilities, such as improved perception and intelligent control, by combining MHDs with sensors, wireless communication, and image processing. In general, advancements in MHD theory and research hold promise for future medical applications and the development of micro- and small-scale MHD.

1.1.1 Actuation and Control

The actuation and control of MHDs play a crucial role in enabling their locomotion and manipulation capabilities. Actuation and control are also essential components in facilitating the locomotion and manipulation capabilities of MHDs in various medical applications.

In many actuation systems, Helmholtz coils can generate adjustable magnetic fields with high control capabilities [62]–[64]. This enables the magnetic field generated by Helmholtz coils to exert precise forces and torques on MHDs, allowing for accurate motion control of the MHD. Therefore, Helmholtz coils are used by many researchers to drive and control MHDs. For instance, Xu *et al.* have presented three orthogonally arranged Helmholtz coil pairs (Fig. 1.3(A)) to generate a uniform rotating field to steer the MHD in the 3-D space with viscous liquid [65]. For the MHD, an Image-Based Visual Servoing control method for arbitrary planar path following has been proposed under a uniform magnetic field generated by Helmholtz coils, where features presented in the image space were directly utilized as feedback [66]–[68]. In order to further improve the control accuracy of the MHD driven by a 3-D Helmholtz coil system, an adaptive

orientation compensation control strategy using the radial basis function networks has been designed to guide the MHD to fellow the 3-D path [69]. For the MHD swimming driven by a 3-D Helmholtz coil system in a 3-D space with obstacles, the path-planning algorithm called optimal Bidirectional Rapidly-exploring Randomized Tree * has been formulated to explore the shortest route in this space, and a proxy-based sliding mode control approach has been developed to design stable controllers based on the error model in the Serret–Frenet frame [70].

For animal experiments and future clinical trials, the current driving mechanism for acutating the MHD using Helmholtz coils may not be suitable due to space limitations and heat generation concerns. Therefore, some other magnetic actuation systems need to be considered and investigated. For instance, a magnetic manipulator cooled with liquid nitrogen has been designed and tested for the MHD [71], as shown in Fig. 1.3(B). This innovative system successfully mitigated the electrical resistance of copper wires, resulting in reduced heat generation during the operation of the magnetic field, where this system incorporated six electromagnets, and its capability to control the MHD was empirically demonstrated. Further, this innovative system has been used to design a closed-loop control method to drive the MHD in 3-D space by combining visual feedback or ultrasound feedback [74]–[79]. Meantime, Zhang *et al.* have proposed an innovative magnetic actuation device that combines a motor module and a coil module [72]. This mobile-coil system had the ability to generate dynamic magnetic fields within a large 3-D workspace, as shown in Fig. 1.3(C). To further obtain a large working space, three robotic arms have been used to move three electromagnetic coils (Fig. 1.3(D)) to drive the MHD [73]. Afterward, Zhang *et al.* have conducted extensive research on MHDs utilizing this novel driving device. For instance, a scheme based on the mobile ultrasound system and magnetic actuation system has been proposed to control the MHD in a long-distance endovascular model [80]. During the motion control of the MHD, the location of the MHD is critical to constructing the closed-loop control system. In previous studies, computer vision has been extensively employed for localizing MHDs and constructing closed-loop control systems. However, this method is not applicable to *in vivo* experimental applications. In addition, although ultrasound imaging is a powerful technique widely used for the MHD's navigation, it has a sensitivity to noises, bubbles, and the hardness of the working environment.

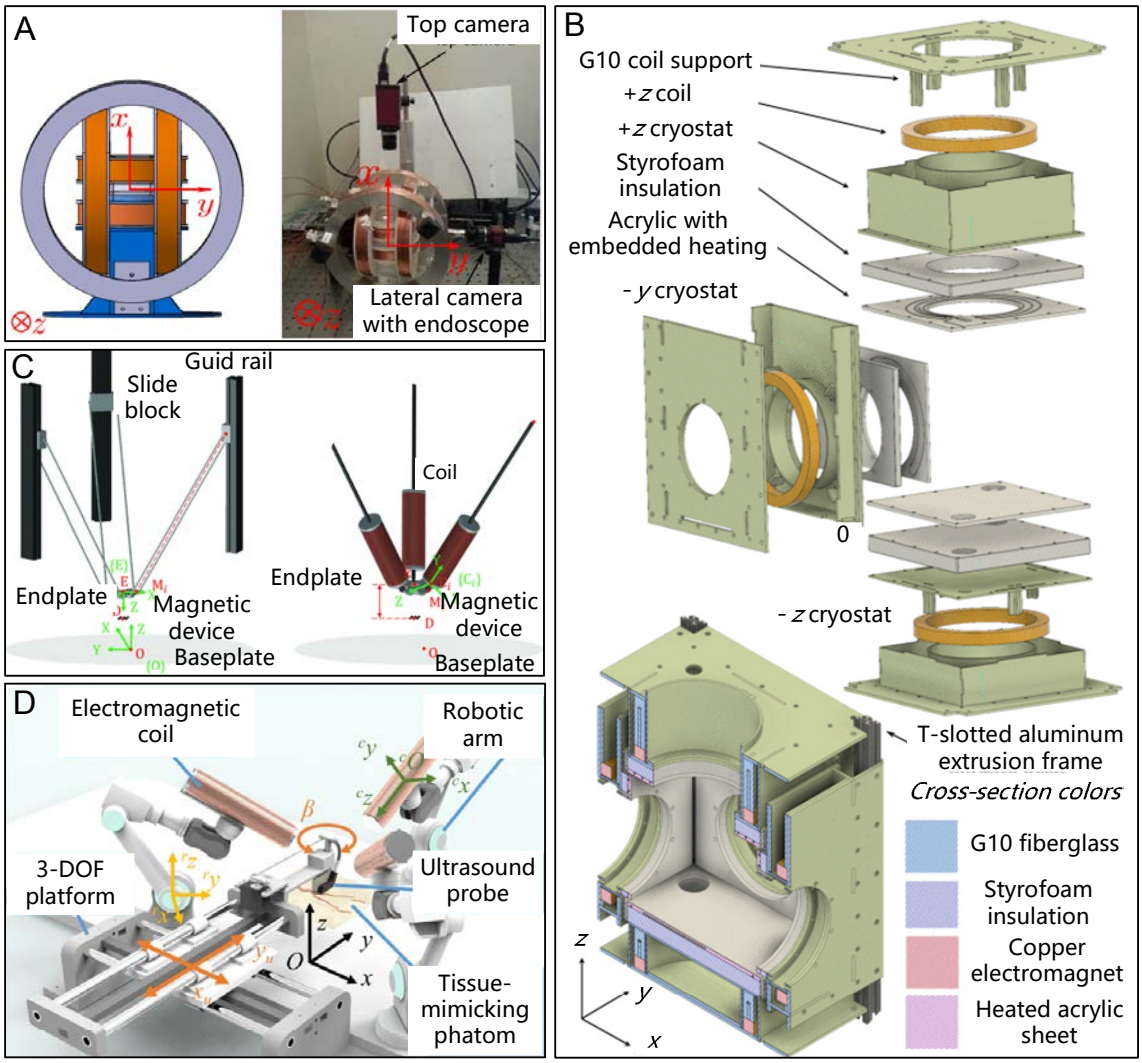

Figure 1.3: The magnetic helical devise (MHD) is driven through a rotating magnetic field generated by electromagnetic coils. (A) The three orthogonally arranged Helmholtz coil pairs are developed to generate a uniform rotating field to actuate the MHD [65]. (B) A magnetic manipulator cooled with liquid nitrogen is presented to steer the MHD [71]. (C) The mobile-coil system, combined with the motor module and the coil module, is designed to generate dynamic magnetic fields in a large 3D workspace [72]. (D) A mobile electromagnetic coils-based actuation system by combining three robotic arms is implemented for magnetic propulsion [73].

X-ray, on the other hand, is an effective localization method for MHDs,

but concerns about the hazards of ionizing radiation exposure exist among both patients and physicians. Hall-effect sensors were used to locate the MHD and further construct the closed-loop control system [81]–[83], however, the presence of an external driving magnetic field can significantly interfere with hall-effect sensors. As a result, it is imperative to select a suitable location method for the construction of the MHD's closed-loop control system.

Compared to electromagnetically driven systems, permanent magnet-based systems have also received significant attention in the MHD's research. A nonuniform magnetic field generated by a rotating permanent magnet has been utilized to control the MHD (Fig. 1.4(A)), and the theory and experiment demonstrated that the manipulator proposed was a viable option for wireless control of MHDs [84]. Furthermore, Abbott *et al.* have presented a more in-depth study of this rotating magnetic field, they have shown that they can control the necessary dipole rotation axis on a 6-DOF robotic manipulator (Fig. 1.4(B)) that allows the magnetic field at any desired point in space to rotate about any desired axis by utilizing linear algebraic techniques [85]. In order to control the MHD swarm, they further have proposed the kinematic model of the MHD swarm under a rotating permanent magnet [86]. Additionally, a rotating permanent magnet has been integrated with a robotic manipulator to actuate the MHD [87]. The focus of this study was on analyzing the open-loop response of the MHD while considering position constraints imposed on the actuating rotating permanent magnet. Under this system, the input and output bounds of the MHD have been further investigated and analyzed [88].

To mitigate the impact of the radial gradient force generated by a rotating permanent magnet on the MHD, a magnetic system employing two synchronized rotating permanent magnets has been utilized to drive the MHD [90], as shown in Fig. 1.4(C). By employing two synchronized dipole fields, the lateral oscillation of the MHD was reduced by 37% compared to using a single dipole field for radial steering, operating at an angular velocity of 31 rad/s. Additionally, the utilization of two synchronized rotating magnets enabled the MHD to achieve an average swimming speed of 2.1 mm/s, whereas using a single rotating dipole field at the same angular velocity results in an average swimming speed of 0.4 mm/s [90], this indicates that the use of two synchronized rotating permanent magnets to drive the MHD significantly increased its swimming speed. The frequency

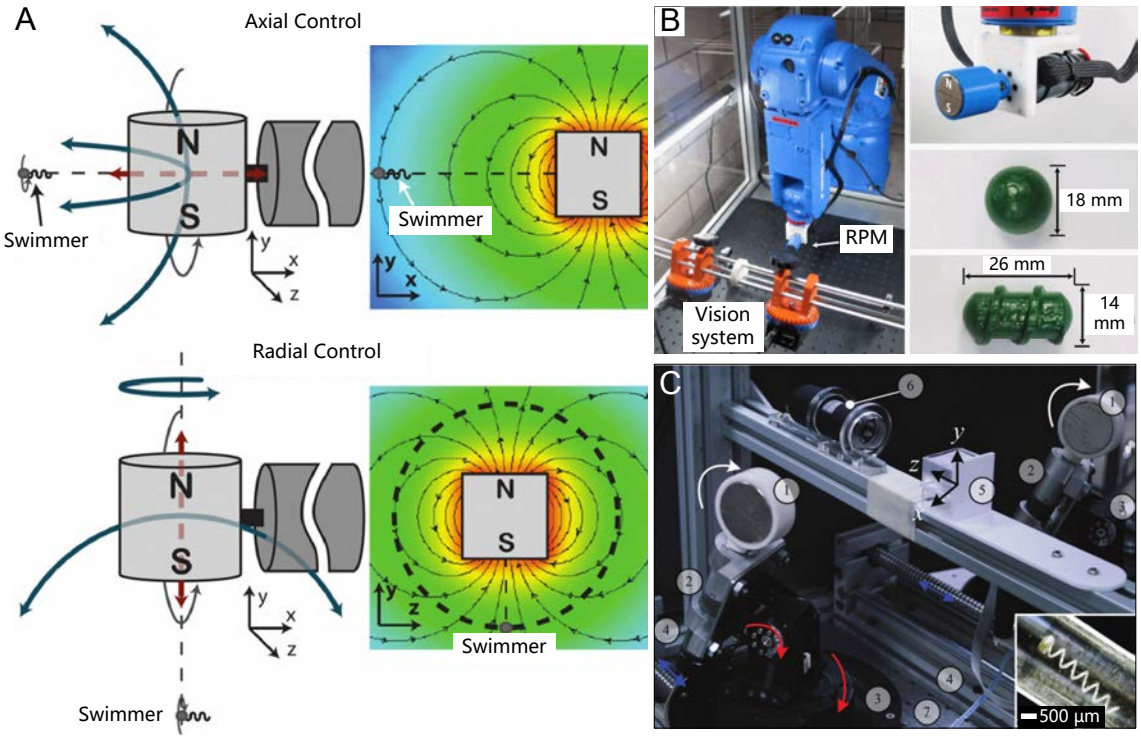

Figure 1.4: The magnetic helical devise (MHD) is driven through a rotating magnetic field generated by permanent magnet system. (A) Axial control and radial control of the MHD with a single rotating permanent magnet (RPM) system [84]. (B) The Yaskawa Motoman MH5 6-DOF robotic manipulator is used to change the position of the single RPM system [85]. (C) A magnetic-based robotic system utilizing two rotating dipole fields enables wireless motion control of the MHD in three-dimensional space [89].

characterization of the MHD has been investigated within a viscous heterogeneous medium using a permanent magnet-based robotic system with two synchronized rotating dipole fields [91]. This synchronized rotating magnetic system has been further employed to enable the steering of the MHD in 3-D space [89].

Overall, the actuation and control capabilities provided by the magnetic system show promising potential for the practical implementation and advancement of MHDs in a variety of medical applications. These advanced magnetic systems will contribute to improved performance, precise control algorithms, efficient power management, and real-time feedback sensing, ensuring the optimal functionality of MHDs in biomedical settings.

However, further advancements in actuation and control technologies are necessary to enhance the capabilities of MHDs and enable their successful integration into diverse biomedical applications.

1.1.2 Biomedical Applications and Challenges

With the rapid development of science and technology, the application of MHDs in the biomedical field has witnessed significant advancements. Researchers have made numerous attempts to explore the potential of MHDs in various biomedical applications. These applications encompass a wide range of areas, including minimally invasive surgery, targeted drug delivery, targeted gene delivery, targeted cell delivery, thrombus removal, and diagnostics [33], [92]–[96].

MHDs, with diverse fabrication and functionalization methods, have shown great potential in targeted drug delivery, targeted gene delivery, or targeted cell delivery for specific pathologies, offering promising avenues for effectively mitigating adverse side effects [97], [98]. For instance, researchers have demonstrated for the first time the successful wireless, targeted, and single-cell gene delivery to human embryonic kidney cells *in vitro*. This achievement was made possible through the utilization of the MHD loaded with plasmid DNA [99]. Furthermore, the researcher has fabricated MHDs coated with biocompatible and pH-responsive zinc-based motile metal-organic frameworks, enabling controlled swimming along predetermined tracks using weak rotational magnetic fields [100]. These multifunctional MHDs demonstrated single-cell targeting and cargo payload delivery within complex microfluidic channel networks, as shown in Fig. 1.5(A). Additionally, a novel magnetically controlled MHD fabricated through 3-D printing with a two-photon lithography system has been studied. This coated MHD, responsive to near-infrared laser light, enabled targeted delivery and photothermal killing of cancer cells [101]. A similarly coated magnetic helical carbon nanomotor has been presented utilizing a combination of microwave heating and chemical vapor deposition [102]. This helical device-coated drug can accomplish cell targeting under magnetic field control, as shown in Fig. 1.5(B). Taking this technology further, a multi-functionalized MHD (Fig. 1.5(C)) with excellent loading capabilities for controlled release of encapsulated substances has been proposed [103]. This MHD was constructed using a combination of microfluidic synthesis,

polyelectrolyte complexation, and magnetic nanoparticle coating. It exhibited wireless steering and rotational locomotion controlled by an electromagnetic system, along with stimuli-responsive behavior for controllable release of encapsulants in response to environmental cues. In addition to micron-scale MHDs, researchers presented a millimeter-scale MHD in paper [104] (Fig. 1.5(D)). This millimeter-scale MHD demonstrated helical navigation, targeted drug release, and mechanical drilling capabilities to address blockages in tubular structures. Experimental results showcased that drug-enhanced drilling was more effective at unclogging the blocked areas compared to simple drilling motion. Moreover, researchers have also introduced a millimeter-scale multifunctional MHD designed for addressing intestinal diseases [105], as shown in Fig. 1.5(E). This device demonstrated the ability to perform active locomotion, dual-drug loading, and selective drug release. This MHD addressed limitations in robot-assisted drug delivery and showed potential for enhancing intestinal disease treatment efficiency. Experimental evaluations demonstrated a high drug loading capacity, controlled locomotion, and targeted drug release without noticeable damage to the pig intestine.

Apart from disease treatment drugs, MHDs have also been utilized for various applications such as cell transfection, detection, differentiation, pathogen isolation, and antibacterial activities, by incorporating biomolecules and metal-based materials [110]. For instance, researchers have proposed the development of the MHD using microfluidics for muscle tissue engineering [111]. By encapsulating muscle cells and magnetic iron oxide nanoparticles in biocompatible helical microfibers, the MHD exhibited controllable movement under magnetic fields, enabling the assembly of cell mass constructions for tissue regeneration and artificial muscle applications. The versatility and potential of these MHDs make them promising for various fields, including cell-cultured meat production. Also using microfluidic technology, a graphene oxide-based helical micromotor has been fabricated, that has shown potential for water remediation and drug delivery applications, exhibiting high removal efficiency of pollutants and drug-loading capabilities [106], as shown in Fig. 1.6(A). Furthermore, a hydrogel-based, magnetically controlled MHD capable (Fig. 1.6(B)) of delivering theranostic cargo and responding to pathological markers in its microenvironment has been presented [107]. This MHD's double-helical architecture enables cargo loading, controlled swimming under magnetic fields, and enzymatic

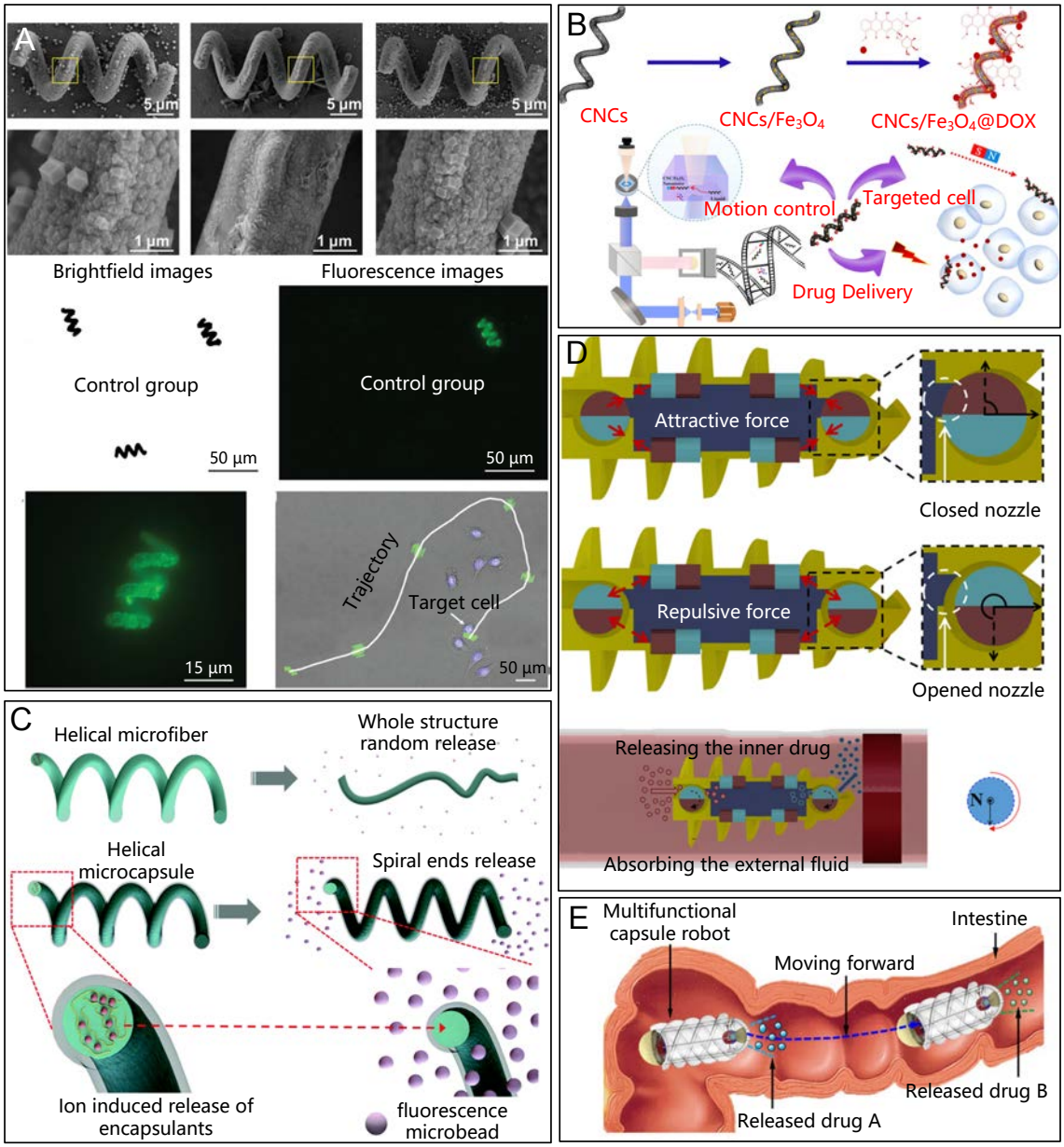

Figure 1.5: Targeted drug delivery of the magnetic helical devise (MHD). (A) A biocompatible and pH-responsive MHD coated with zeolitic imidazole framework-8 and motile metal-organic framework is fabricated, demonstrating the ability to swim along predetermined paths using weak rotational magnetic fields [100]. (B) A MHD coated with the anticancer drug doxorubicin is fabricated toward target cells to effectively kill the cells [102]. (C) The corresponding ion-induced release by the MHD and microfiber using the chelating agent is performed [103]. (D) A MHD is actuated to get the target position to release the drugs [104]. (E) In *ex vivo* experiments, locomotion and drug release tests of the MHD are conducted [105].

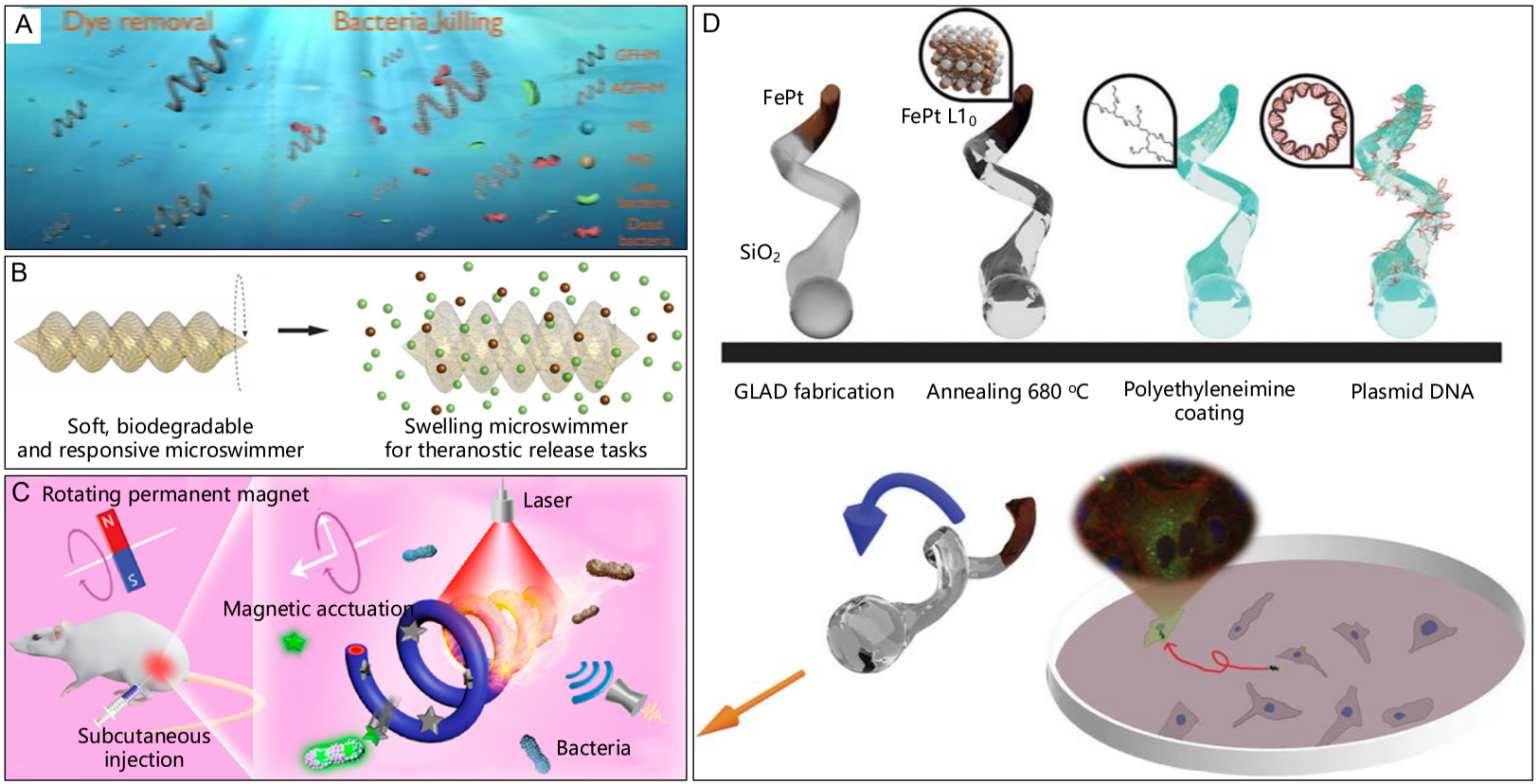

Figure 1.6: Targeted cell transfection of the magnetic helical devise (MHD). (A) A MHD is fabricated which can perform for water remediation and drug delivery applications [106]. (B) A hydrogel-based and magnetically powered MHD is reported, which can achieve the theranostic cargo delivery and release tasks [107]. (C) A MHD is presented which can be real-time image tracked and diagnose capabilities for the treatment of bacterial infections [108]. (D) The MHD is used for active cell targeting and magnetic transfection of lung carcinoma cells [109].

degradation. It demonstrated efficient cargo release in response to matrix metalloproteinase-2 enzyme levels and showcased the release of functional cargos, such as antibody-tagged magnetic nanoparticles for targeted labeling of cancer cells. In addition, a polydopamine-coated MHD based on a magnetized Spirulina matrix has been presented, offering enhanced photoacoustic imaging, photothermal therapy, and fluorescence diagnosis capabilities [108]. This MHD demonstrated real-time image tracking and theranostic capabilities for the treatment of bacterial infections, suggesting its potential as an antibacterial MHD *in vivo*, as shown in Fig. 1.6(C). The researcher has also demonstrated the fabrication of ferromagnetic FePt MHD through a single annealing step, resulting in noncytotoxic and biocompatible nanomotors with magnetic properties comparable to permanent micromagnets [109], as shown in Fig. 1.6(D). This FePt MHD was used for active cell targeting and magnetic transfection of lung carcinoma cells, exhibiting successful internalization and unaffected cell viability.

In addition to using MHDs for targeted drug delivery and targeted cell therapy, many research groups also utilized MHDs for thrombus removal due to their unique structure [113], [116], [117], as shown in Fig. 1.7. In paper [112], the author has presented a biocompatible shape memory alloy MHD (Fig. 1.7(A)) capable of precise structure transformation, enabling adjustable motion behavior and mechanical properties. This MHD offered a solution for vascular occlusion through its shape memory effect, effectively functioning as a micro-driller for unclogging and a self-propulsive stent. Other research groups have applied ultrasound to guide the MHD to the location of the thrombus and then removed the thrombus driven by an external magnetic field [14], [118], [119]. In order to further understand the removal of thrombus by the MHD, Khalil *et al.* have studied the impact of rubbing on the removal rate of blood clots *in vitro* [114], [120]. They have proposed a hydrodynamic model based on resistive force theory to analyze the rubbing behavior using the MHD driven by two rotating dipole fields. Furthermore, the MHD has been utilized to perform an *in vivo* experiment for the removal of aortic thrombus in rats [115]. During the experiments, the formation of artificial thrombi and the subsequent thrombus removal process were closely observed and monitored using X-ray imaging techniques, as shown in Fig. 1.7(D). In contrast to mechanical methods for removing blood clots, the MHD equipped with thrombolytic drugs has been developed. Utilizing an external rotating magnetic field,

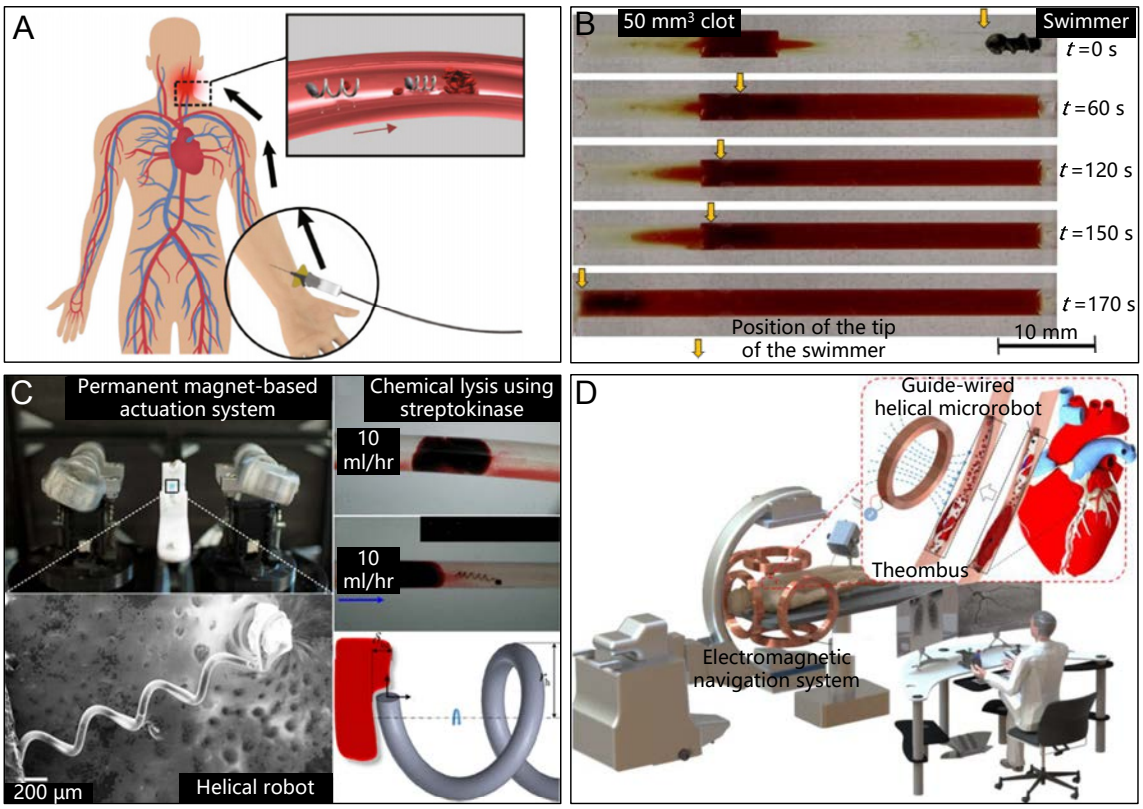

Figure 1.7: Thrombus removal using the magnetic helical devise (MHD). (A) A shape-memory MHD is proposed for thrombus removal [112]. (B) A MHD removing a human blood clot inside a poly-dimethyl siloxane channel is proposed [113]. (C) A permanent magnet-based actuation system for the MHD is used to generate rotating magnetic fields and achieve mechanical rubbing of blood clots [114]. (D) The MHD is navigated toward the target in the steering mode, after which an alternative magnetic field is applied to generate powerful drilling to break the thrombus [115].

the MHD precisely navigated to the location of the clot and subsequently released the thrombolytic drugs [121].

Although MHDs have made significant progress in biomedical applications and have achieved promising results, there are still several challenges that need to be addressed for their practical implementation in clinical surgery. Firstly, there is a need to optimize the design and control of MHDs to ensure their safe and effective operation inside the human body. This includes improving their locomotion capabilities, enhancing their ma-

neuverability in complex anatomical structures, and minimizing the risk of tissue damage or adverse reactions. Secondly, the scalability of MHDs is an important consideration. While MHDs have demonstrated successful performance in small-scale models and animal studies, the translation of their functionality to larger dimensions, such as for applications in human-sized blood vessels or organs, remains a challenge. In addition, many previous studies have explored the utilization of MHDs in vascular models, but most of them have focused on low-flow conditions [104], [122]–[125]. However, when it comes to arteries and veins with high flow velocities, the movement of MHDs is significantly influenced by the blood flow. In high-flow environments, the strong blood flow can exert turbulent flow patterns and strong hydrodynamic forces on the MHD, leading to difficulties in maintaining its desired trajectory and controllability. Therefore, the design and actuation mechanisms of MHDs need to be adapted to accommodate the size variations and physiological conditions of different patients. Thirdly, biocompatibility and biodegradability are crucial factors to be addressed. MHDs should be constructed from materials that are safe for long-term use inside the body and can eventually biodegrade or be safely expelled. It is essential to ensure that the MHD materials do not induce inflammation, immune responses, or other adverse effects on the surrounding tissues.

In addition, the integration of imaging and sensing capabilities into MHDs is crucial for real-time monitoring, feedback, and precise navigation. While magnetic resonance imaging (MRI), X-ray, and computed tomography (CT) are valuable imaging modalities in many clinical applications, they do present certain limitations and challenges when used in MHDs control [126], [127]. MRI scanners generate strong magnetic fields, which can interfere with the operation of magnetic-based robotic systems [128]. The presence of the MRI magnetic field can disrupt the control and navigation of MHDs, affecting their accuracy and stability. MRI images have a relatively slower acquisition time compared to real-time ultrasound imaging. This slower image acquisition may impact the MHD control feedback loop, making it more challenging to achieve real-time control and navigation. Furthermore, CT and X-ray imaging involve the use of ionizing radiation, which can pose potential risks to both patients and operators [129]. In contrast, ultrasound imaging offers advantages in the MHD control due to its real-time imaging capability, radiation-free nature, and wider accessibility [130]. The high frame rate of ultrasound allows for more immediate feed-

back on the MHD's position and environment. Additionally, the low cost and portability of ultrasound equipment make it suitable for integrating with robotic systems in various clinical settings. However, the presence of ultrasound image noise has an impact on the location of the MHD, which in turn affects the overall operation of the system and the motion control of the MHD. Reducing the impact of ultrasound image noise on the MHD location is indeed a significant challenge. Addressing these challenges is a crucial step towards making MHDs a practical reality in clinical settings. This adoption could lead to significant advancements in minimally invasive medical procedures, targeted drug delivery, and a range of other valuable biomedical applications.

1.2 Research Objectives

The challenges associated with motion control of the USHD inside the vascular network have been a significant motivation for the development of closed-loop control systems based on the permanent-magnet robotic (PMR) system presented in this work. The following research questions (**RQs**) are identified in the areas of control and location of the USHD in the vascular model with dynamic physiological fluid.

RQ. 1

How does the flow of a physiological fluid affect the motion of the USHD?

In the medical field, USHDs have the potential to fulfill various crucial functions, including sensing, diagnosis, fluidic manipulation, blood clot removal, and localized drug delivery. In particular, the utilization of USHD in vascular disease applications holds great promise as a wireless approach to reaching and navigating the complex network of blood vessels in the human body. These devices may enable healthcare professionals to perform tasks in areas that are otherwise difficult to access, allowing for enhanced diagnostic and therapeutic capabilities. However, a significant challenge lies in the controllable actuation of USHDs in physiological flow conditions, where they need to move effectively across a wide range of flow rates from 1 um/s to 400 mm/s. Therefore, for **RQ. 1**, we investigate the motion

characteristics of an externally actuated USHD within a fluid-filled lumen in the presence of dynamic flow. We start by developing a hydrodynamic model for the USHD, which allows us to estimate the size of the region of attraction around a desired reference position. By utilizing the concept of the region of attraction, we gain insights into how the USHD responds to various flow rates and actuation frequencies, providing a comprehensive understanding of its behavior. Furthermore, by establishing these parameters, it becomes possible to exert control over the USHD's motion and counteract the effects of the fluid flow. Particularly, the task of determining an open-loop equilibrium point and defining a region of attraction facilitates 1-D control of the USHD against the flow when the feedback signal fails.

RQ. 2

How does the penetration depth of the vascular model affect both the contrast-to-noise ratio (CNR) of ultrasound images during ultrasound guidance and the subsequent closed-loop motion characteristics of the USHD?

In our previous study, we employed computer vision to construct a corresponding closed-loop control system of the USHD. However, employing this approach in real clinical applications proved impractical. Consequently, in our subsequent investigation, we opted for an ultrasound imaging system. The ultrasound imaging system is radiation-free and provides a wider range of applications due to its low cost and relatively high frame rate. As a result, the ultrasound imaging system is utilized for the localization of the USHD inside the vascular model. Furthermore, considering that the depth of blood vessels beneath the skin differs across various locations, it is essential to understand how the USHD signal detected by the ultrasound system is affected by the increasing depth of vessel penetration. In this question (**RQ. 2**), we employ the CNR as a quantitative measure to assess the signal of a USHD detected by an ultrasound system. By utilizing CNR, we can evaluate the distinguishability and clarity of the USHD signal against the background noise. Furthermore, based on the guidance provided by ultrasound imaging, we establish a closed-loop control system for the USHD. Through this closed-loop control system, we can analyze and examine the motion characteristics of the USHD, taking into account the real-time feedback from the ultrasound imaging system.

RQ. 3

How to design a robust control system to drive a USHD in a 3-D vascular model using the PMR system under ultrasound guidance?

Achieving precise and stable control of the USHD is of paramount importance when using it for the treatment of vascular diseases. The success of the procedure heavily will rely on the USHD's ability to navigate through the intricate blood vessels. Therefore, the development of an effective and robust closed-loop control strategy is of utmost importance under ultrasound guidance. Furthermore, how to construct an effective and robust closed-loop control strategy for a USHD under ultrasound guidance is a problem worth studying. For this question (**RQ. 3**), based on the reconstructed 3-D vascular model using 2-D ultrasound images, a dynamic region of interest is proposed to eliminate the noise signal due to the surrounding environment of the vessel and the vessel wall. Then a point-to-point closed-loop control method is established based on the PMR system and ultrasound imaging. In addition, we also evaluated the effectiveness of this method under different blood flow rates.

1.3 Outline of the Thesis

This doctoral thesis is organized into five chapters to address the aforementioned research questions. **Chapter 2**, **Chapter 3**, and **Chapter 4** form part of the research studies either published or under review in international conferences or international peer-reviewed journals.

We first make major contributions to the research on the USHD against the flow of a physiological fluid. **Chapter 2** addresses **RQ. 1** and provide a 1-D model for the helical propulsion of an externally actuated USHD against blood serum. This model presents an open-loop equilibrium point that is influenced by the flow in the uniform field region between two rotating permanent magnets, and this equilibrium point shifts quadratically with the flow. To evaluate the performance of the system, we conduct tests on both open-loop and closed-loop behaviors using this model. The results demonstrate that the state of the USHD can achieve asymptotic convergence even when the USHD swims against varying flow rates.

Chapter 3 and **Chapter 4** answer **RQ. 2** and **RQ. 3**, and highlights

the real-time ultrasound guidance of USHDs in various vascular models, including 1-D, 2-D, and 3-D vascular models. These two chapters delve into the specific challenges related to using ultrasound technology for guiding the USHD within these vascular model environments. In **Chapter 3**, the focus shifts towards modeling the behavior of the USHD inside blood vessel phantoms. This modeling aims to predict the impact of several factors, including the localization gap, flow rates, and CNR, on the closed-loop control behavior. **Chapter 3** then delves into the characterization of the closed-loop control system inside a blood vessel phantom at varying penetration depths and dynamic flow rates. Additionally, it covers the motion control of the USHD inside a blood vessel phantom with a bifurcation. **Chapter 4** achieves the integration of a mobile ultrasound imaging device with the PMR system, enabling simultaneous localization and driving of the USHD. Before the motion control of the USHD, a 3-D vascular model is constructed using 2-D ultrasound images, providing reference paths for the USHD to navigate. Remarkably, the USHD successfully navigates intricate and winding pathways inside the 3-D vascular model, primarily relying on ultrasound guidance and the PMR system. Furthermore, **Chapter 4** evaluates the performance of the USHD's locomotion within a blood flow environment, considering various flow rates. This comprehensive approach combines ultrasound imaging, precise motion control, and evaluation in realistic conditions to enhance the capabilities of the USHD for navigating complex vascular structures.

Finally, we showcase the key discoveries of the doctoral research, with a specific emphasis on the modeling, feedback, and control aspects of USHDs. **Chapter 5** commences with a comprehensive summary of the contributions made throughout the research and concludes by providing valuable insights for future investigations in the field.

1.4 Research Framework Funding

All the research studies that constitute this doctoral thesis have been supported by funds from the European Research Council (ERC) under the European Union's Horizon 2020 Research and Innovation programme under grant 866494 project-MAESTRO, and financial support from the China Scholarship Council (CSC No. 201908210341). All the studies presented in this thesis have been performed with the experimental setups at the

Surgical Robotics Laboratory (SRL), in the Department of Biomedical Engineering of the University of Groningen and University Medical Center Groningen, Groningen, the Netherlands.

1.5 Scientific Output

The studies presented in this doctoral thesis have been a part of the following articles that have been published in the following journals and international conferences:

1.5.1 Peer-Reviewed Journal Articles

1. **C. Li**, S. Misra, and I.S.M. Khalil *"Closed-Loop Control Characterization of Untethered Small-Scale Helical Device in Physiological Fluid with Dynamic Flow Rates"*, Advanced Intelligent Systems, 5(5): 2200322-1–2200322-11, May 2023.

2. **C. Li**, S. Misra, and I.S.M. Khalil *"Navigation of Untethered Small-Scale Helical Devices Using Fully Automated Magnetic System and Ultrasound Guidance"*, IEEE Transactions on Medical Robotics and Bionics, vol. 5, no. 4, pp. 1093-1104, November 2023.

1.5.2 Peer-Reviewed International Conference Article

1. **C. Li**, F. R. Halfwerk, J. Arens, S. Misra, M. Warlé, and I.S.M. Khalil *"Controlled Helical Propulsion Against the Flow of a Physiological Fluid"*, Proceedings of the Annual International Conference on Manipulation, Automation, and Robotics at Small Scales (MARSS), Toronto, Canada, July 2022.

1.5.3 Abstract

1. **C. Li**, S. Misra, and I.S.M. Khalil *"Motion Control of Helical Robots in a Vascular Model of Carotid Artery under Ultrasound Guidance"*, Proceedings of the W. J. Kolff Annual Research Days, Groningen, Netherlands, April 2021.

2

Controlled Helical Propulsion Against the Flow of a Physiological Fluid

Note: *Following chapter is adapted from the article "Controlled Helical Propulsion Against the Flow of a Physiological Fluid" by* ***C. Li****, F. R. Halfwerk, J. Arens, S. Misra, Michiel Warlé, and I.S.M. Khalil, published in " Proceedings of the International Conference on Manipulation, Automation and Robotics at Small Scales (MARSS) ", pages 1-6, Toronto, Canada, 2022.*

Abstract

Untethered small-scale helical devices (USHDs) have the potential to navigate bodily fluids using permanent-magnet robotic systems for minimally invasive diagnostic and surgical procedures. These devices can be actuated by robotically moving rotating permanent magnets (RPMs) to achieve controllable steering and propulsion simultaneously in a wireless manner. To date, the vast majority of motion control systems using USHDs are constrained to operate in the absence of a dynamic flow field and prior work did not rigorously address the fundamental roles of rheological, magnetic, and geometric characteristics of the USHD and its surroundings on the resulting stability. In this work, we show how to construct the region of attraction of a USHD driven by two synchronized RPMs inside fluid-filled lumen around an equilibrium point. We first present the governing hydrodynamic model of a magnetically-driven USHD to describe its behavior against the flow of blood serum. Then we validate the model using 1-D frequency response

characterization and show that it captures the measured linear relationship between the actuation frequency and propulsive thrust at various flow fields. We find that a region of asymptotic stability can be achieved around an equilibrium point allowing a 6-mm-long USHD to overcome maximum volumetric flow field of 1.2 l/hr (i.e., 2.65 cm/s).

2.1 Introduction

There is an increasing clinical need for wireless untethered magnetic devices (UMDs) that can perform important functions such as sensing, diagnosis, locomotion, actuation, fluidic manipulation, material removal, and localized drug delivery [131], [132]. In particular, the use of untethered small-scale helical devices (USHDs) and microrobots in biomedical applications is a promising method to move wirelessly toward inaccessible regions in the body. A great deal of research has addressed the potential of these devices in static-fluid environments to characterize their behavior and enhance their locomotion strategies [133]–[136]. However, motion control of these devices *in vivo* would require them to bypass the following hurdles: first, to swim controllably along and against the flow of bodily fluids inside confined environments [137]; second, to maintain proper locomotion conditions (i.e., generating enough propulsive thrust and remaining in sync with the external field) inside physiological fluids with heterogeneous rheological properties, near wall-effects, and concentrated cells; third, to be able to swim and drill through bodily fluids and soft-tissue, respectively, enabling interventions with large proportions of the body; and last, to scale up the magnetic manipulation system to the size of an intended biomedical application such as blood clot removal.

We see in the literature that the most promising magnetic manipulation approach is one where a controlled magnetic field is generated either using a clinical magnetic resonance imaging (MRI) system or by robotically moving a continuously rotating dipole field [84], [138]–[140]. Some approaches produce controlled magnetic fields using configurations of electromagnets surrounding a workspace [141]. These configurations are mostly closed to compensate for the field that changes rapidly in space, resulting in a limited workspace suitable for *in vivo* small animal experiments only. An advantage of a clinical MRI system over any other magnetic manipulation system is their ability to simultaneously actuate and localize UMDs. However, the

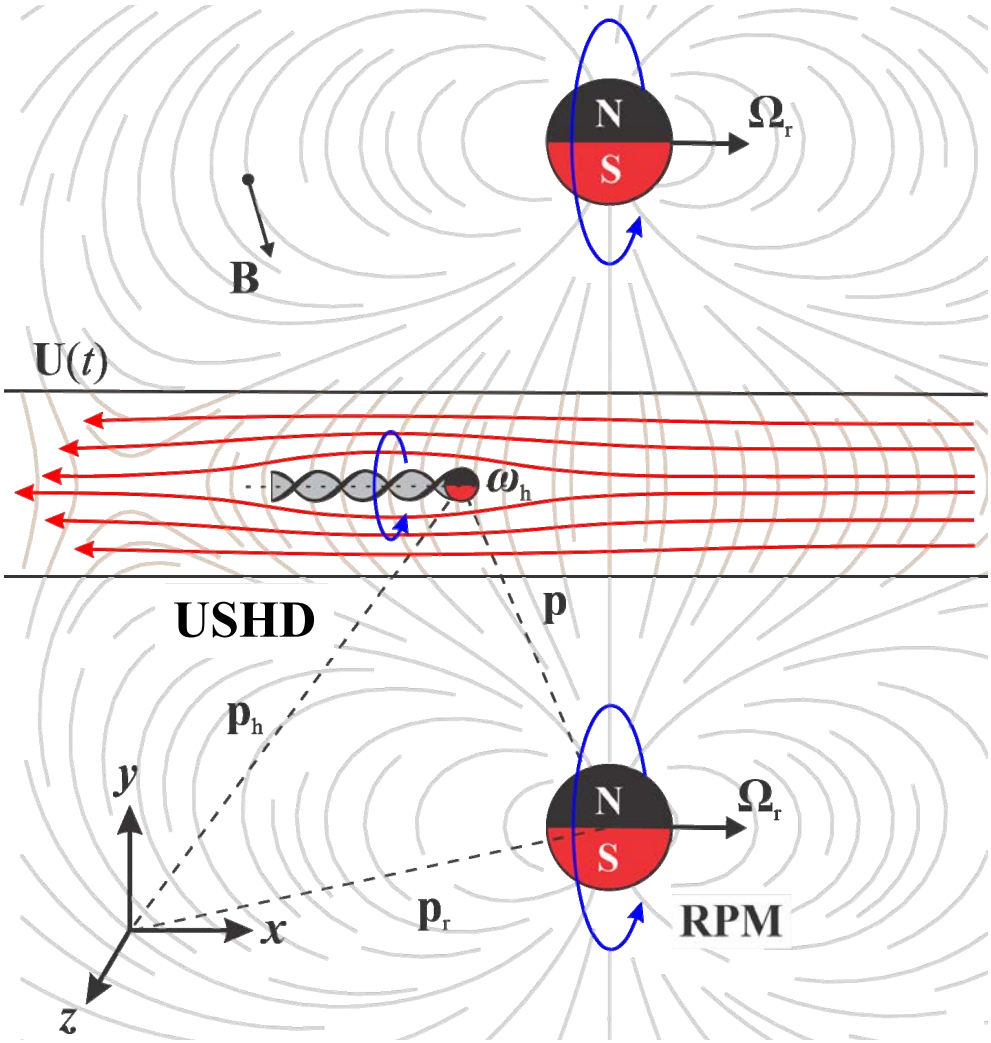

Figure 2.1: An untethered small-scale helical device (USHD) swims inside a fluid-filled lumen against the flow, $\mathbf{U}(t)$. Two rotating permanent magnets (RPMs) produce a time-periodic magnetic field, $\mathbf{B}$, applying magnetic torque on the magnetic moment of the USHD. The USHD and the RPMs are characterized by the position vectors $\mathbf{p}_\mathrm{h}$ and $\mathbf{p}_\mathrm{r}$, respectively. The USHD can be steered by controlling the RPM's rotation axis, $\widehat{\mathbf{\Omega}}_\mathrm{r}$, robotically. To align the USHD along the lumen, we set $\widehat{\mathbf{\Omega}}_\mathrm{r} = [1, 0, 0]^T$ with respect to frame of reference $\{\boldsymbol{x}, \boldsymbol{y}, \boldsymbol{z}\}$.

challenge is in the motion control of USHDs that requires manipulation of its field-rotation axis and continuously rotating the magnetic field about this axis. An MRI system cannot control the direction of the magnetic field,

thereby explicitly limiting the types of UMDs to those driven by magnetic field gradients.

If alternatively a permanent magnet (or multiple) is allowed to robotically move while rotating about a desired axis of rotation, then the magnetic force and torque can be managed to actuate and steer any type UMDs or USHDs. For example, the permanent-magnet robotic system of Mahoney *et al.* works by controlling a single rotating permanent magnet (RPM) using a robotic manipulator to manage the magnetic force and torque in a wireless fashion [142]. They have demonstrated this method by actuating rotating magnetic devices in a lumen (i.e., spherical rolling UMD and USHD). Instead of surrounding the workspace with a closed configuration of electromagnetic coils for controlled magnetic field generation [141], permanent-magnet robotic systems allow the RPM to move freely during wireless actuation of the UMDs. Niedert *et al.* have used this concept to control a tumbling UMD using a two-degree-of-freedom (DOF) rotating permanent magnet inside a murine colon *in vivo* [143]. However, the challenge is in the actuation of UMDs controllably in physiological flow conditions; that is, they must move in a wide range of flow rates with Reynolds number in the range 10-4000 [144]. In this work, we study the closed-loop motion characteristics of an externally actuated USHD inside a physiological fluid-filled lumen with a dynamic flow. We begin by providing a hydrodynamic model for the USHD and estimate the size of the region of attraction around a desired reference position. Using the region of attraction enables us to understand the response of a USHD to a wide range of flow rates and actuation frequencies. The problem of finding an open-loop equilibrium point and a region of attraction enables one-dimensional (1-D) control of the USHD against the flow without feedback.

The remainder of this paper is organized as follows: In Section 2.2, we give a brief overview of the governing equations of a USHD to explain the basic properties of flow, interactions, and actuation. Characterization of the helical propulsion and 1-D control experiments are presented in Section 2.3. Finally, Section 2.4 concludes and provides directions for our future work.

2.2 Locomotion of USHD Inside Fluid-Filled Lumen

We consider a USHD with an axis of symmetry $\widehat{\boldsymbol{\omega}}_{\mathrm{h}}$. The USHD of length L and diameter $2R$ has an average magnetic moment $\mathbf{m}$, lying orthogonal to its axis of symmetry (i.e., $\mathbf{m}_{\mathrm{h}}^{T}\widehat{\boldsymbol{\omega}}_{\mathrm{h}} = 0$). The material frame of reference of the USHD is located at its center of mass and characterized by the position vector $\mathbf{p}_{\mathrm{h}}$ with respect to a reference frame (Fig. 2.1). When the USHD is placed between two synchronized RPMs with an average magnetic moment $\mathbf{M}$, it experiences a time-periodic magnetic field $\mathbf{B}(t, \mathbf{p})$. The magnetic field is nonuniform and not force free with the exception of the region between the RPMs [145]. These RPMs are robotically moved to control the rotation axis, $\widehat{\boldsymbol{\Omega}}_{\mathrm{r}}$, of the RPM and actuate the USHD, while immersed in an inertial physiological fluid contained in a lumen. As the USHD rotates about $\widehat{\boldsymbol{\omega}}_{\mathrm{h}}$, it swims against or along fluid flow $\mathbf{U}(t)$.

2.2.1 Governing Equations of the USHD

We now develop the governing equations and discuss the theoretical background pertaining to the swimming scheme in Fig. 2.1. The two RPMs, which rotate in sync, are separated by equal distances to a fluid-filled lumen to assist the actuation of the USHD by a resultant pulling magnetic force. When the RPMs are allowed to rotate about $\widehat{\boldsymbol{\Omega}}_{\mathrm{r}}$ while their position vector $\mathbf{p}_{\mathrm{r}}$ is kept fixed, the pulling magnetic force is expected to assist the propulsive thrust only in one part of the lumen. Consider, for example, the situation where the RPMs are located halfway along the lumen, then the position of the USHD with respect to the RPM dictates the direction of the pulling magnetic force along the $\boldsymbol{x}$-axis. In the case when the USHD is located halfway along the lumen between the RPMs, we will obtain a magnetic force to assist propulsion. This force is given by $\mathbf{f}_{\mathrm{m}} = (\mathbf{m} \cdot \nabla)\mathbf{B}(t, \mathbf{p})$ and counterbalances the fluidic drag force $\mathbf{f}_{\mathrm{d}} = 0.5\rho A C_{\mathrm{d}}(\mathbf{v} - \mathbf{U}(t))^2$, where $\mathbf{v}$ is the transnational velocity of the USHD and A is its cross-sectional area. Further, ρ is the density of the fluid and C_{d} is the fluid dynamic resistance coefficient. When the USHD rotates in sync with the RPMs, a propulsive thrust, $\mathbf{f}_{\mathrm{p}} = k\boldsymbol{\omega}$, would contribute to its transnational velocity regardless of its position with respect to the RPMs. Therefore, the total

Table 2.1: The untethered small-scale helical device (USHD) contains a cylindrical Grade-N42 NdFeB magnet with magnetic moment $\mathbf{m}$. The rotating permanent magnet (RPM) is a cylindrical Grade-N52 NdFeB magnet with magnetic moment $\mathbf{M}$. Blood serum, of viscosity η and density ρ, is contained inside a cylindrical lumen of diameter D_l parallel to the rotation axis of the RPM, $\widehat{\mathbf{\Omega}}_\mathrm{r}$.

	Property	Value	Property	Value
USHD	$2R \times L$ [mm]	1.5×6	$\|\mathbf{m}\|$ [A.m^2]	6.23×10^{-4}
	Pitch [mm]	1	Helicity [°]	71
RPM	$D \times H$ [mm]	45×30	M [A.m^2]	52.26
	$\widehat{\mathbf{\Omega}}_\mathrm{r}^T$	$[1, 0, 0]$	$\mathbf{B}$ [mT]	5
Fluid	ρ [kg.m^{-3}]	906	η [mPa.s]	1.105
	Re	< 10	C_d	0.02
	D_l [mm]	4	$\|\mathbf{U}\|$ [ml/hr]	≤ 1200

forces on the USHD with a mass m is given by [146]

$$m\dot{\mathbf{v}} = \mathbf{f}_\mathrm{m} + \mathbf{f}_\mathrm{d} + \mathbf{f}_\mathrm{p} + \mathbf{f}_\mathrm{c} + \mathbf{f}_\mathrm{w}, \tag{2.1}$$

where $\mathbf{f}_\mathrm{c}$ and $\mathbf{f}_\mathrm{w}$ are the contact forces with the wall of the lumen and apparent weight of the USHD, respectively. Equation (2.1) completes the governing dynamics of the transnational motion and the rotational dynamics can be determined in a similar manner. Note that the basic properties of the flow dictate the importance of the inertial force in the left-hand side of Equation (2.1). Here, we are concerned with dynamic flow fields, $\|\mathbf{U}\| \sim 10^{-2}$ m/s and our USHD in the millimeter range, yielding Reynolds number on the order $Re \sim 10$. Therefore, the interactions between the fluid's inertia and the viscous forces cannot be ignored and the contribution of the inertial force is incorporated in the numerical analysis.

2.2.2 Numerical Solution of the 1-D Problem

Researchers have explored numerical solutions for Equation (2.1) to predict the time-averaged forces and swimming trajectories. One very good way to

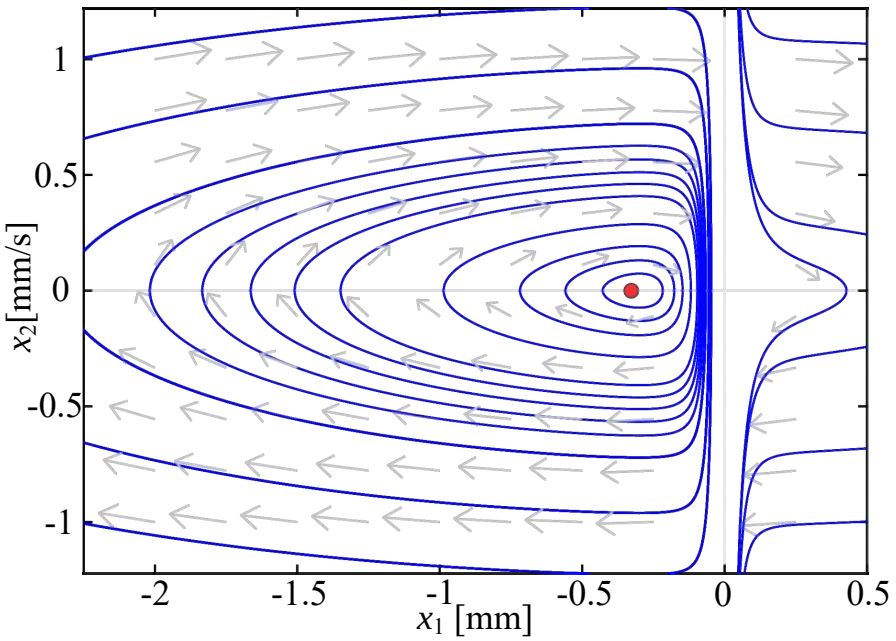

Figure 2.2: Inspection of the phase portrait of the 1-D hydrodynamics of the USHD shows that trajectories of the states, $[x_1, x_2]^T$, starting in the interval $[0, L_l/2)$ cannot stay in the same interval because the flow and the pulling magnetic force act along the same direction (negative $\boldsymbol{x}$-axis). In the interval $(-L_l/2, 0]$, where the magnetic force is opposite to the flow, the USHD can stay within a region centered at the equilibrium point (red circle). L_l represents the total length of the lumen.

gain more physical insight into the dynamics is to analyze the 1-D problem; perhaps the understanding can be used in a generalization for the full-order system. For 1-D swimming problem in the absence of contact, Equation (2.1) becomes simply

$$\begin{aligned} \dot{x}_1 &= x_2 \\ \dot{x}_2 &= 1/m\,(f_{\mathrm{m},x} + f_{\mathrm{d},x} + f_{\mathrm{p},x})\,, \end{aligned} \tag{2.2}$$

where $f_{\mathrm{m},x}$, $f_{\mathrm{d},x}$, and $f_{\mathrm{p},x}$ are the force components along the $\boldsymbol{x}$-axis. Further, the states x_1 and x_2 represent the position and velocity components of the USHD along the $\boldsymbol{x}$-axis, respectively. Physically, the magnetic force scales as $f_{\mathrm{m}} \sim 3\mu_0\|\mathbf{m}\|\|\mathbf{M}\|/2\pi x_1^4$, where μ_0 is the permeability of free space. Note that f_{m} changes sign with x_1, and qualitatively the contribution of the magnetic force is not expected to assist propulsion when the

USHD swims past the RPMs. Also since the USHD and the surrounding fluids have non-zero velocities, the drag force scales with the velocity difference as $f_{\mathrm{d}} \sim (x_2 - U_x)^2$. Therefore, for a given flow rate, U_x, the drag force is quadratic in x_2. Finally, the propulsive thrust is linear in $\boldsymbol{\omega}$ of the USHD, and subsequently linear in $\boldsymbol{\Omega}$ of the RPM, below a step-out frequency. Note that unlike the magnetic force and drag force, whose interactions with the states depend on the inverse fourth power of the position and second power of the velocity, the propulsive thrust can be controlled through the angular velocity of the RPMs.

Let us construct the phase portrait of the 1-D model using Equation (2.2) and the nominal parameters in Table 2.1. In this case, the RPM's rotation axis is set to $\widehat{\boldsymbol{\Omega}}_{\mathrm{r}} = [1, 0, 0]^T$ resulting in approximately 1-D swimming along the $\boldsymbol{x}$-axis of the lumen. Fig. 2.2 shows the constructed phase portrait when the flow field is set to $\|\mathbf{U}\| = 1200$ ml/hr and the angular frequency of the RPMs is 10 Hz. Inspection of the phase portrait shows that all trajectories starting in the interval $[0, L_1/2)$ cannot stay in the same interval. Although the USHD continuously rotates about its axis of symmetry, it cannot move against the attractive magnetic force of the RPMs and the fluid drag. In contrast, trajectories of the USHD starting in the interval $(-L_1/2, 0]$ will stay in the same interval for all future time. The trajectories spiral around an equilibrium point (red circle) and cannot stay identically in any of the closed sets that are shown by the blue curves.

All trajectories in the set $S = \{x_1 < 0, |x_2| > 0\}$ will spiral around the equilibrium point along asymmetric closed curves. This asymmetric pattern is attributed to the nonlinearity of all forces in Equation (2.2) with the exception of the propulsive thrust. The component of the pulling magnetic force along the $\boldsymbol{x}$-axis increases as the inverse fourth power of the position and falls off rapidly when the USHD swims from left to right toward the region between the RPMs where the magnetic field is more uniform. Within this region, the field is more uniform than that of any other positions along the lumen and the magnetic force vanishes by the symmetry of the RPMs with respect to the lumen and the USHD. Therefore, a USHD with trajectories starting in the set S will oscillate and remain in one of the blue closed curves in Fig. 2.2 only if all conditions remain *ideally* fixed.

Note that the oscillation of the states of the USHD is a result of energy transfer between the kinetic energy storage elements (i.e., inertia of the fluid and the USHD) and the potential energy storage element (i.e., mag-

netic field). The amplitude of this oscillation is dependent on the initial conditions and the system can have a steady-state oscillation with a small amplitude around the equilibrium point. In this case, the propulsive thrust and the pulling magnetic force will hold the USHD against the flow, but will not allow it to swim far beyond the set S. This problem can be alleviated if the RPMs are translated along the lumen, and permanent-magnet robotic systems are typically equipped with transnational DOF that can be employed to shift the equilibrium point along a prescribed path in an open-loop fashion.

2.3 Magnetic Actuation and Motion Control Against the Flow

In our experiments, a permanent-magnet robotic system is used to generate controlled rotating magnetic field to validate the results of the 1-D model. The position of the RPMs is kept fixed with respect to the lumen, as shown in Fig. 2.1.

2.3.1 Experimental Results

A lumen of 4 mm in diameter by 70 mm long is connected to a pump system (77910-55 L/S Variable-Speed Pump System, Masterflex, Illinois, USA) to regulate the flow of blood serum (F7524–500ML, Sigma-Aldrich, USA). The diameter of the lumen is comparable to the medium arteries and veins. Flow measurements inside the lumen are conducted using an ultrasound system (SonixTouch Q+, BK Medical, Quickborn, Germany). The lumen is placed in the $\boldsymbol{xy}$-plane to lie parallel to the $\boldsymbol{x}$-axis between the RPMs of the permanent-magnet robotic system (Fig. 2.1). The long axis of the lumen and the rotation axes of the RPMs are constrained to lie in the $\boldsymbol{xy}$-plane. A USHD of 6 mm in length and 1.5 mm in diameter is 3-D printed using polylactic acid and assembled to a cylinder of NdBFe magnet such that the magnetic moment is perpendicular to the long axis of the helical body (pitch of 1 mm). The NdBFe magnet is 1 mm in length and diameter and provides an average magnetic moment of 6.23×10^{-4} A.m^2.

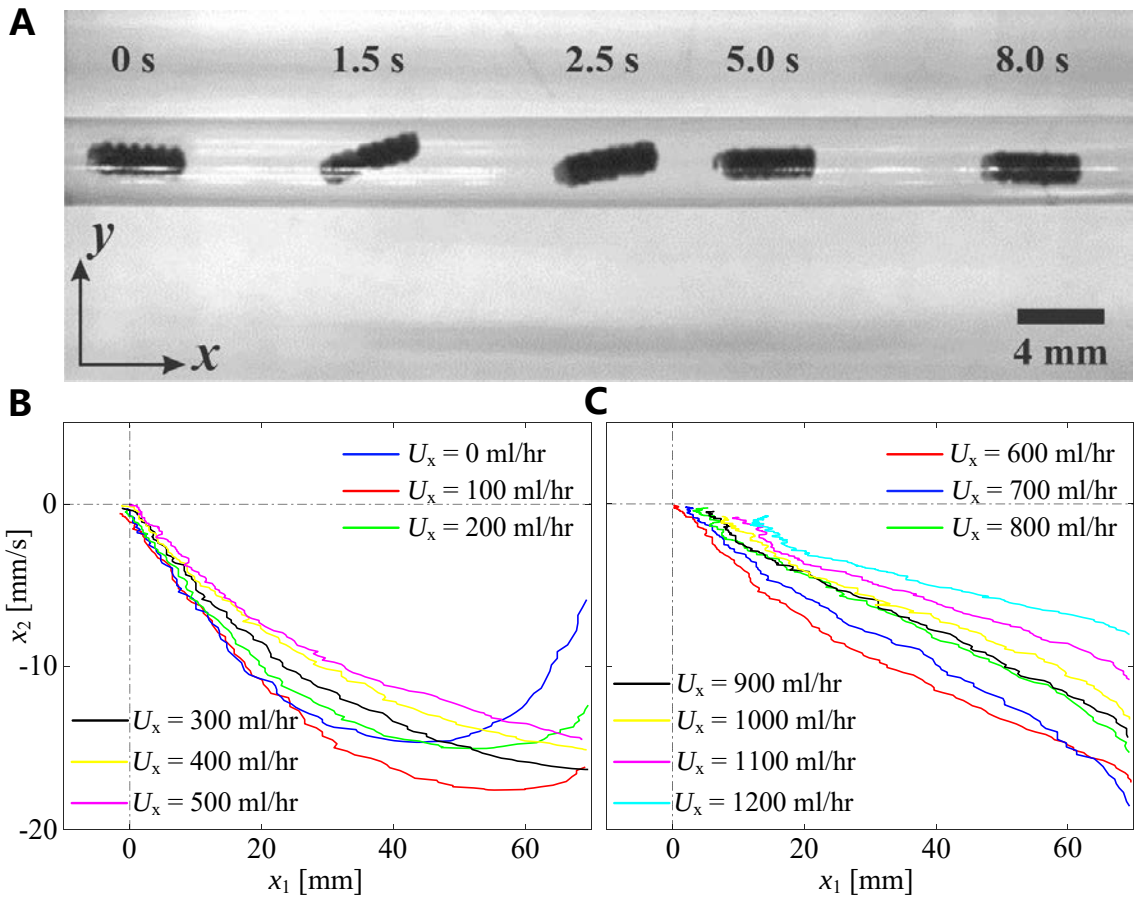

Figure 2.3: Open-loop control of a USHD against the blood serum flow. The USHD swims from left to right at $\boldsymbol{\omega} = 10$ Hz. (A) The USHD is attracted toward the equilibrium point at zero flow. (B)-(C) Convergence of the states for the flow range of $0 \leq \|\mathbf{U}\| \leq 500$ and $600 \leq \|\mathbf{U}\| \leq 1200$ ml/hr. *Please refer to the accompanying video.*

2.3.2 Open-Loop Characterization of the Region of Attraction

Below the step-out frequency of the USHD, its propulsive thrust is linearly proportional to its angular velocity, $\boldsymbol{\omega}$. This is the rotational velocity at which the USHD will trail behind the rotating magnetic field of the two RPMs. We allow the RPMs to rotate in synchrony at an angular frequency of $\|\boldsymbol{\Omega}\| = 10$ Hz. In this experiment, the USHD is initially located at one side of the lumen and allowed to swim from left to right. This is equivalent to the numerical results by setting the initial states of the USHD to the

set S. Blood serum is allowed to flow along the $-\boldsymbol{x}$-axis (from right to left) in the $0 \leq \|\mathbf{U}\| \leq 1200$ range. At $\|\mathbf{U}\| = 0$ ml/hr, the USHD is propelled and pulled toward the open-loop equilibrium point, as shown in Fig. 2.3(A). Note that, at $t = 8$ s, the USHD reaches the equilibrium point and its states become close to zero (Fig. 2.3(B)). When flow is induced for the same actuation inputs, the equilibrium point slightly shifts, as shown in Figs. 2.3(B) and 2.3(C).

To understand the significance of the flow rate, we can determine the equilibrium point in the uniform field region between the RPMs. By setting $\dot{x}_1 = \dot{x}_2 = 0$, and solve for x_1 and x_2, we have

$$(x_1, x_2) = \left(\frac{\rho A C_{\mathrm{d}}}{2k} \|\mathbf{U}\|^2, 0 \right). \tag{2.3}$$

When the fluid is static (i.e., $\|\mathbf{U}\| = 0$), the equilibrium point is at the origin, $(x_1, x_2) = (0, 0)$. For a non-zero flow, the equilibrium points shift quadratically with $\|\mathbf{U}\|$ along the x_1-axis. Note that the average magnetic moments of the USHD and the RPM do not play a role in the equilibrium point because it is located in the uniform field region. Therefore, the location of the equilibrium point depends only on the characteristics of the flow, geometric parameters of the USHD, and the relationship between the propulsive thrust and the angular velocity. Using the same open-loop data set in Fig. 2.3, we can investigate the steady-state response of each trajectory versus each flow rate. Fig. 2.4 shows the location of each equilibrium point for a given flow field. The bubble size specifies the x_2-component of the equilibrium point. We see that the x_1-component shifts approximately quadratically with $\|\mathbf{U}\|$, and therefore the equilibrium point (2.3) captures the experimental behavior of the USHD during helical propulsion against the flow in the $600 \leq \|\mathbf{U}\| \leq 1200$ ml/hr range. It is desirable to decrease the influence of the flow rate on the location of the equilibrium point. Once the USHD moves and approaches the equilibrium point, the behavior of the trajectories around the equilibrium point will depend on (2.3). This implies that when the USHD is close enough to the equilibrium point, the geometric and rheological characteristics of the USHD and the flow will only scale the effect of the flow. A smaller cross-sectional area, leads to a smaller shift in the equilibrium point regardless of the induced flow. Similarly, a steep frequency response curve (i.e., greater k), leads also to smaller shifts in the equilibrium. Finally, flow characterized with greater Re will lead to smaller

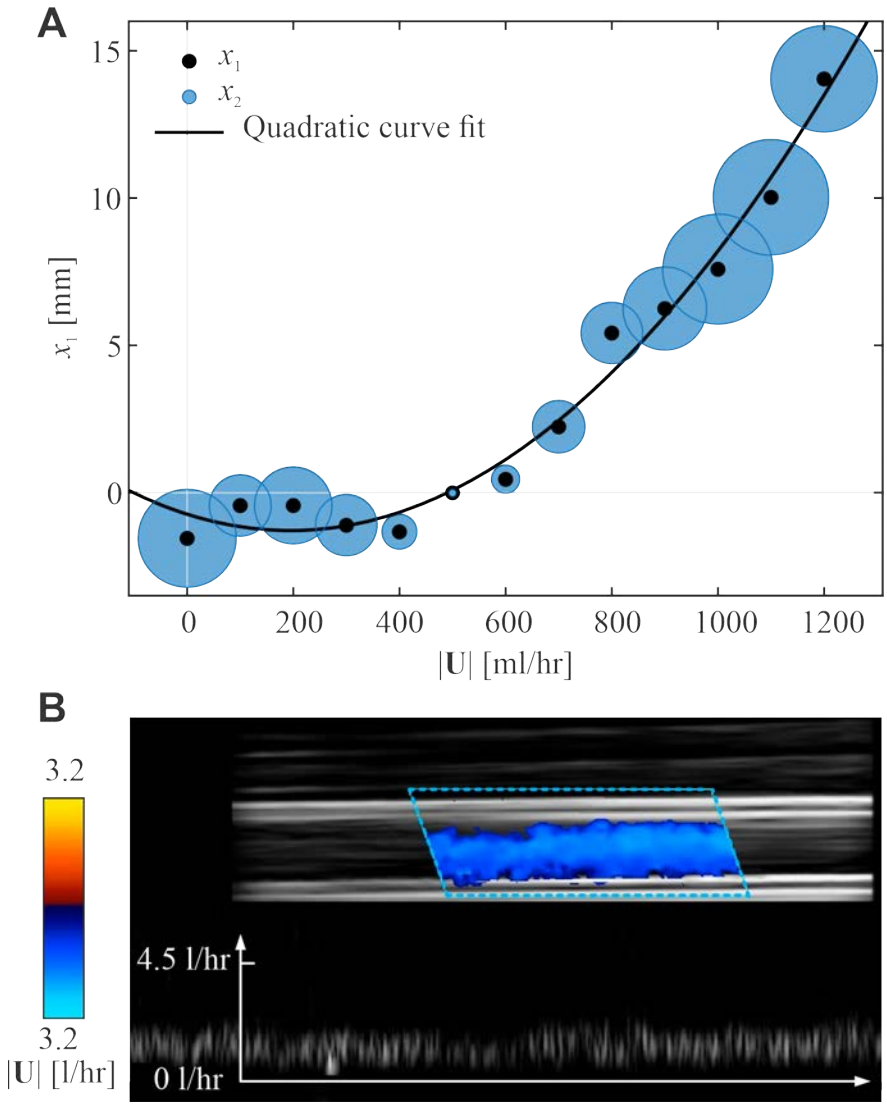

Figure 2.4: The equilibrium point, (x_1, x_2), shifts approximately quadratically with the flow rate, $\|\mathbf{U}\|$. (A) The size of the bubble represents the measured x_2-component of the equilibrium point. (B) The flow rate of blood serum is visualized and measured using Doppler data. Gelatin is used as phantom to contain the lumen with respect to the transducer at depth of 2.5 cm.

C_d, resulting in smaller shift in the equilibrium point.

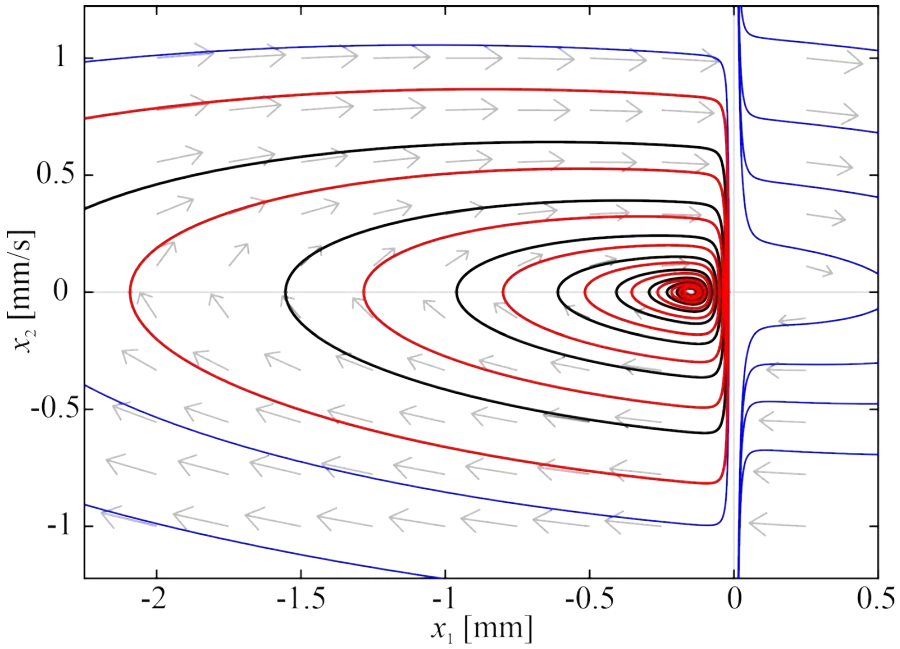

Figure 2.5: Phase portrait of the 1-D hydrodynamics of the USHD with state feedback control shows a stable equilibrium point. The black and red trajectories indicate two different sets of initial conditions starting in the interval $(-L_1/2, 0]$. These trajectories spiral toward the equilibrium point. Length of the lumen is L_1.

2.3.3 Asymptotic Regulation Against Flow

Suppose we can control the angular velocity of the RPM such that a desired state feedback control law stabilizes the equilibrium point. Setting $f_{p,x} = k_1 x_1 + k_2 x_2$ in Equation (2.2) yields a stable equilibrium point, as shown in Fig 2.5. Once again notice that all trajectories starting outside the set S would not stay in S. However, if we restrict the trajectories to start in S they will spiral toward the origin. The red and black trajectories indicate two different sets of initial conditions, both starting in S. Note that the phase portraits in Fig. 2.2 and Fig. 2.5 differ from each other in that the trajectories will not converge asymptotically in the case of open-loop actuation against the flow, while convergence to the equilibrium point is achieved when the angular velocity of the RPMs is applied as a function of the states of the USHD.

Now we implement this asymptotic regulation strategy as before for the same flow range. Fig. 2.6(A) shows the motion of the USHD from left

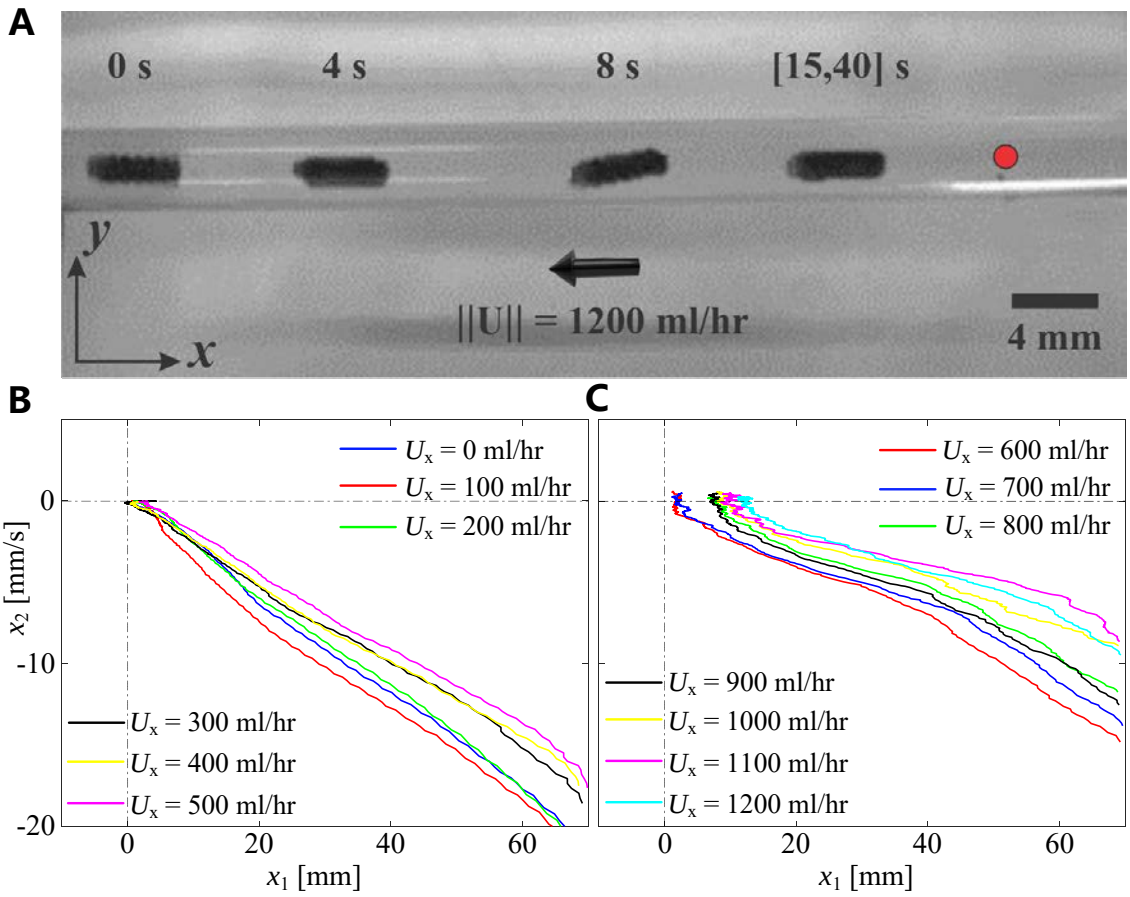

Figure 2.6: Closed-loop control of a USHD against the blood serum flow. (A) The USHD swims from left to right against flow of 1200 ml/hr toward the reference position (red circle). (B)-(C) Convergence of the states for the flow range of $0 \leq \|\mathbf{U}\| \leq 500$ and $600 \leq \|\mathbf{U}\| \leq 1200$ ml/hr. *Please refer to the accompanying video.*

to right toward a reference position (red circle). In this trial, the USHD is controlled against fluid flow of 1200 ml/hr. At $t = 15$ s, the USHD is fixed with respect to the reference position. As the USHD approaches the reference position, the pulling magnetic force decreases and becomes dependent on its propulsive thrust only. At this time instant, the propulsive thrust is large enough to hold the USHD against the flow but insufficient to reach the target. In this case, the position tracking error is measured as 2 body lengths (i.e., 12 mm).

Figs. 2.6(B) and 2.6(C) show the closed-loop behavior of the USHD for

the flow range of $0 \leq \|\mathbf{U}\| \leq 1200$. In this range, the error in absolute value is bounded by 2 body lengths and decreases to approximately 0.1 body length (i.e., 1 mm) when the flow rate is decreased to zero. There is a close agreement between the phase portrait (Fig. 2.5) and the results of this closed-loop control trial (Fig. 2.6) in that the USHD converges to the equilibrium point as t tends to infinity. The location of the equilibrium point shifts as a function of the flow rate, as shown in Fig. 2.4(A), allowing us to predict the steady-state error for a given flow rate.

Analysis of the phase portraits of the open- and closed-loop equilibria show that a state feedback input is required to achieve convergence of the trajectories. While the trajectories of the open-loop system will not approach the equilibrium, exhibiting oscillatory response with unsustained amplitude, the need to hold the USHD within a region around the equilibrium point might be useful when feedback is not available. Note that the fluid flow is restricted to be uniform in our analysis and experiments, as shown in Fig 2.4(B). A pulsatile flow is not likely to yield significant difference in the behavior since a pulling magnetic force assists the propulsive thrust in fixing the USHD around the equilibrium point. A pulsatile flow can be considered in Equation (2.2) as a uniformly bounded periodic disturbance (i.e., there exists $c > 0$, such that $\|f_{\mathrm{d},x}\| \leq c$, $\forall t \geq 0$). With the uniform boundedness of the pulsatile drag, the control problem becomes one of finding a state feedback control law to achieve exponential stability of the system with zero flow.

2.4 Conclusions

We provide a 1-D model for the helical propulsion of an externally actuated USHD against blood serum. This model provides an open-loop equilibrium point, in the uniform field region between two RPMs, that shifts quadratically with the flow. We test the open- and closed-loop behavior using this model and show that we can achieve asymptotic convergence against maximum flow rate of 1200 ml/hr. At this flow rate, the error in absolute value is bounded by 2 body lengths and reduces significantly to 0.1 body length when the flow is decreased to zero. The gained physical insights and correspondence between theoretical and experimental results motivate the use of our system to test USHDs in clinical physiological flow conditions in future research.

Chapter Overview

In **Chapter 2**, we delved into the analysis of the 1-D helical propulsion of the USHD. We explore how the USHD responds to different flow rates and actuation frequencies. While in this study, we establish a closed-loop control system by combining visual feedback, it's worth noting that in clinical applications, relying on visual feedback can often be impractical. With the advent of cutting-edge technologies, the integration of ultrasound guidance with medical robots has propelled medical interventions to unprecedented levels of precision and efficiency. Ultrasound guidance enables medical professionals to access real-time imaging and navigation capabilities, allowing them to visualize vascular networks within the human body. This imaging modality provides invaluable insights into anatomical structures, aiding in the diagnosis of diseases and the planning of minimally invasive procedures.

Therefore, in **Chapter 3** of this thesis, our primary focus is on utilizing ultrasound images to guide the USHD within the vascular model. In **Chapter 3**, we model the dynamic flow and consider the influence of ultrasound image noise on measurements. We also design the closed-loop control system for the USHD based on bifurcation analysis of a 1-D hydrodynamic model. Furthermore, we provide analysis for characterizing the closed-loop control of USHDs within both 1-D and 2-D blood vessel phantoms. This characterization is carried out using a PMR system under the guidance of ultrasound technology.

3

Closed-Loop Control Characterization of Untethered Small-Scale Helical Device in Physiological Fluid with Dynamic Flow Rates

Note: *Following chapter is adapted from the article "Closed-Loop Control Characterization of Untethered Small-Scale Helical Device in Physiological Fluid with Dynamic Flow Rates" by* ***C. Li****, S. Misra, and I.S.M. Khalil (2023), published in " Advanced Intelligent Systems", volume 5, issue no. 5, pages 2200322-1–2200322-11.*

Abstract

Untethered small-scale helical devices (USHDs) have the potential to navigate blood vessels and treat vascular occlusive diseases. However, there are still many challenges in translating this method into clinical practice, both in terms of localization and wireless motion control. In this paper, we show closed-loop control characterization of the USHD against and along physiological fluid inside a blood vessel phantom at different penetration depths. We first model the dynamic flow and ultrasound images noise affecting the measurement, and design the control system of the USHD based on bifurcation analysis of a one-dimensional (1-D) hydrodynamic model. Then we construct a region of attraction of a USHD driven by a permanent-magnet robotic (PMR) system inside a blood vessel phantom around an

equilibrium point. Further, the point-to-point closed-loop control strategy is implemented based on the magnetic point-dipole approximation and kinematic control of the PMR system and ultrasound feedback inside a physiological bodily fluid, blood vessel, and soft-tissue. The frequency response of the USHD is characterized against and along the flowing streams of fetal bovine serum within different flow rates in the 6-20 mm s^{-1} range. Our experimental results demonstrate the ability to navigate the USHD inside both a 1-D blood vessel phantom and a blood vessel phantom with a bifurcation with maximum position error of 1.99 ± 0.55 mm.

3.1 Introduction

Untethered small-scale helical devices (USHDs) have potential in medical applications, such as targeted drug delivery [147]–[149], thrombus removal [83], [113], and biosensing [150], [151]. Compared with traditional surgery, USHDs are expected to enable interventions with minimal trauma and relatively fast post-operative recovery. For medical USHDs, many proposed actuation mechanisms have been studied, such as magnetic fields [80], [152], [153], chemical fuels [154], [155], light energy [156], enzymatic [157], and acoustic wave [158]. Among these actuation mechanisms, USHDs driven by magnetic fields have been extensively studied for two key reasons. First, the effect of the magnetic field on the body is negligible. Second, the magnetic field is not influenced by the physical surroundings inside the body. Recently, Wang *et al.* have proposed a closed-loop control method based on ultrasound guidance to control a colloidal microswarm in three-dimensional (3-D) space using fields generated by electromagnetic coils, and localization of the microswarm at different penetration depths have been demonstrated [159]. Yan *et al.* have proposed a control strategy through the use of integrated ultrasound and photoacoustic images to track a USHD, which allows for accurate real-time control and manipulation in optically non-transparent biological tissues [160]. However, in these studies [159], [160], the workspace is limited, due to the use of the Helmholtz coils surrounding the workspace. As a result, scaling up for clinical trials is not viable.

The precise control of the intravascular USHDs is critical inside the complex vascular network of the human body, which is similar to that in tissue. Lee *et al.* have driven the USHDs to a designated lesion inside

a 3-D coronary artery phantom through an external magnetic field, and demonstrated thrombus removal [161]. Pane *et al.* have implemented real-time visualization, position tracking, and motion control of a USHD in the lumen of a tissue-mimicking phantom using ultrasound phase analysis [162], [163], both in static and dynamic flow conditions [164]. Arcese *et al.* have implemented control of a magnetically guided microrobotic system in blood vessels, and they have proposed an adaptive backstepping control law that ensures a Lyapunov stable and accurate control of a USHD [165]. Regardless of whether USHDs are controlled inside a complex blood vessel network or tissue, the noninvasive localization technology of USHDs is critical to construct a corresponding closed-loop control system for medical applications. Salerno *et al.* have presented a magnetic field triangulation algorithm for localization of the capsule inside the gastrointestinal tract [166]. Son *et al.* have developed real-time localization method using 2-D array of mono-axial Hall-effect sensors, and this method has been used to accurately estimate the position and orientation of a USHD [167]. Khalil *et al.* have also developed magnetic field-based localization method to localize USHDs inside an *ex vivo* model of a rabbit aorta [83]. In addition, magnetic resonance imaging (MRI) has been used to localize nanoparticles and steer them to follow a reference path [168]. Computed tomography (CT) system has also been used to scan an intestinal tract, so that USHDs can move to the target area under the influence of an external magnetic field [63].

Compared with MRI, CT, X-ray, and other imaging systems, ultrasound images are radiation-free and have a wider range of applications due to its low cost and relatively high frame rate [129]. Ultrasound imaging system operates at frequencies between 1 MHz and 100 MHz and provides a spatial and temporal resolution of a millimeter to micrometers [11]. Ultrasound waves are able to penetrate into and move through tissue and bodily fluid inside the body for scanning at different depths using various frequencies. For instance, a 1-MHz-ultrasound wave penetrates the body to 4 cm in muscle and 15 cm in fat. Therefore, ultrasound system represents a viable option to visualize human tissue and provide visual feedback for motion control of the USHDs [14], [73]. However, the contrast-to-noise ratio (CNR) of ultrasound images has not been taken into account during the design of control systems, and the USHD localization within ultrasound images is crucial for constructing closed-loop control system. Therefore, we first use

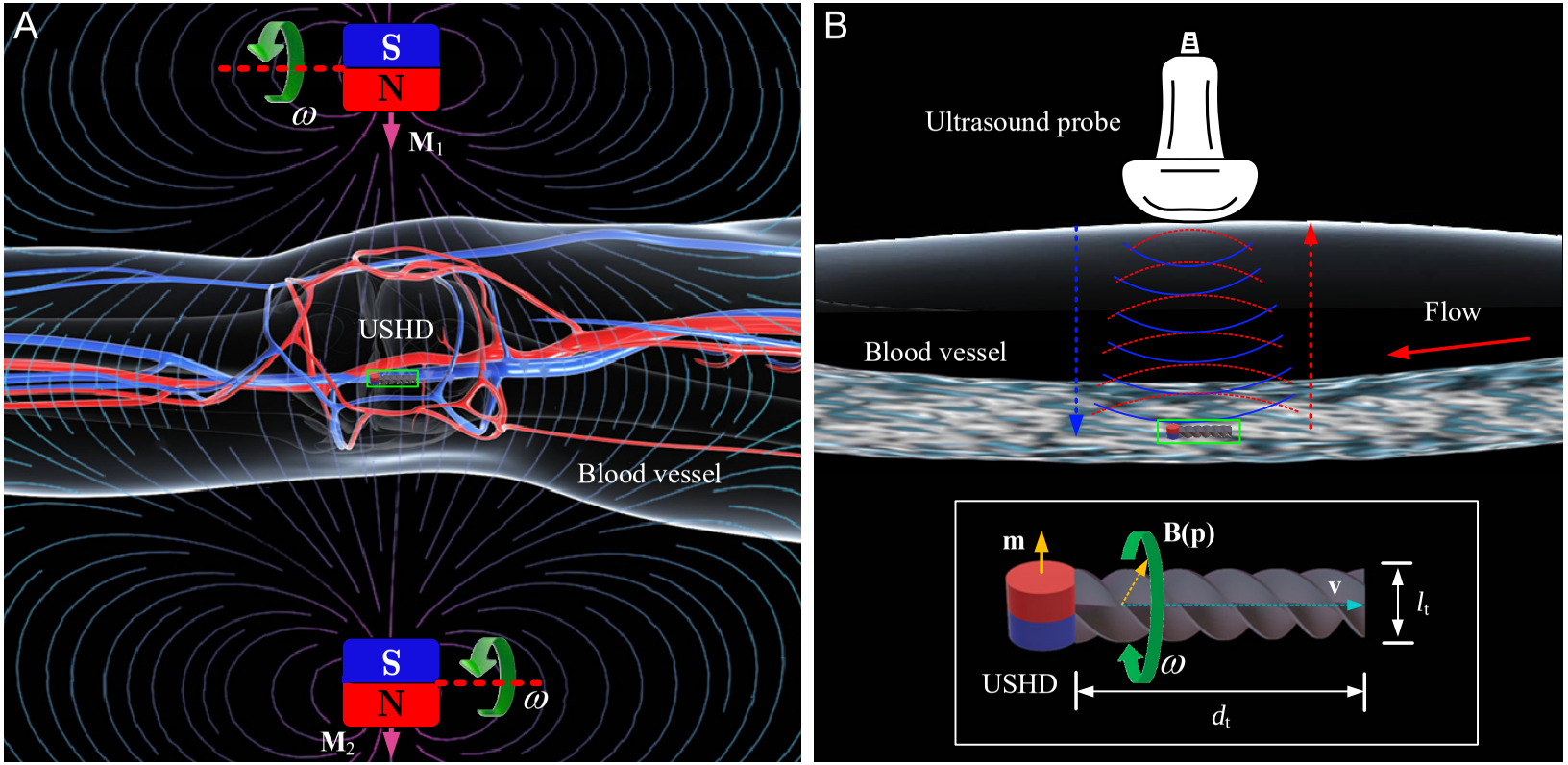

Figure 3.1: Magnetic fields $\mathbf{B}(\mathbf{p})$ generated by two synchronously rotating permanent magnets with angular frequency of ω, which can actuate untethered helical magnetic device (USHD) inside the blood vessel phantom of the leg under the guidance of ultrasound images. (A) $\mathbf{M}_1$ and $\mathbf{M}_2$ are the magnetic dipole moments of the permanent magnets. (B) The position of the USHD is determined using ultrasound images. The blue curve and red dashed curves indicate the direction of the original ultrasound waves and the reflected waves via the USHD, respectively. $\mathbf{m}$ is the magnetic dipole moment of the USHD.

the CNR to quantify visibility of the USHD at different penetration depths, and design a closed-loop motion control system to quantify the control characteristics of the USHD (Fig. 3.1) at different penetration depths in the 15-35 mm range. Compared with existing systems [161], [163], [169], our permanent-magnet robotic (PMR) system has an open configuration and unobstructed large workspace, as shown in Fig. 3.2(A). In the structural design of the PMR system, the collision between the ultrasound probe and the permanent magnets is avoided. We do not need to consider the issue of coil heating since the rotating magnetic field is generated by two rotating permanent magnets. Therefore, we can use the PMR system for exceptionally long periods of time. In addition, the position of the USHD converges asymptotically to the target position when the angular velocity of two rotating permanent magnets is applied as a function of the position and velocity of the USHD. Further, we achieve the following:

(a) Modeling of the USHD inside a blood vessel phantom to predict the influence of the localization gap, flow rates, and CNR on the closed-loop control behavior.

(b) *In vitro* characterization of the frequency response of the USHD against and along physiological fluid inside a blood vessel phantom with different flow rates to determine the bounded behavior of the closed-loop control system.

(c) Point-to-point closed-loop control using ultrasound feedback and the PMR system (Fig. 3.2(A)).

(d) Characterization of the closed-loop control system inside a blood vessel phantom at different penetration depths with dynamic flow rates, and motion control of the USHD inside a blood vessel phantom with a bifurcation.

The remainder of this paper is organized as follows: Section 3.2 describes the mathematical modeling and control problem statement of the USHD to understand how experimental results are affected by the localization depth, flow rate, and CNR of the localization system. The PMR system is described, and the CNR and frequency response experimental results are presented in Section 3.3. Section 3.4 provides discussions about the limitation of experiments and potential applications of the USHD and the PMR system. Finally, Section 3.5 concludes and provides directions for future work.

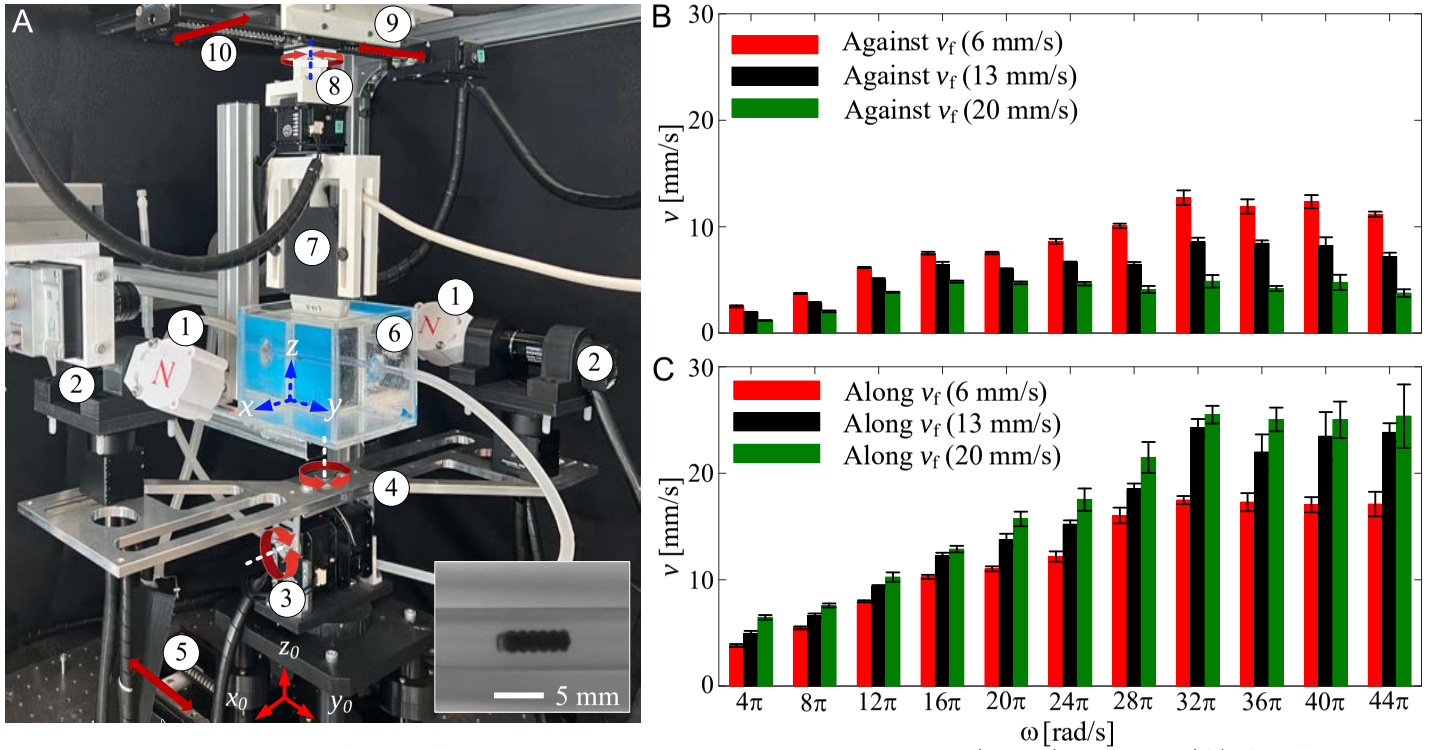

Figure 3.2: Frequency response of the USHD under a permanent-magnet robotic (PMR) system. (A) A USHD is controlled using a PMR system, which comprises two dipole fields ① fixed to two DC motors ②. The motors are fixed on robotic bases with three degree-of-freedom (3-DOF) (pitch ③, yaw ④, and a linear motion stage ⑤). The blood vessel phantom is fixed in the container ⑥ of the soft-tissue phantom. Motion of the USHD is tracked using ultrasound images, and the ultrasound probe ⑦ is fixed on another robotic base with 3-DOF. The motor ⑧ can rotate the ultrasound probe, and two linear motion stages (⑨ and ⑩) can translate the ultrasound probe along the x_0-axis and the y_0-axis of the global coordinate system $\{x_0, y_0, z_0\}$. The phantom frame of reference is indicated by $\{x, y, z\}$. Frequency response of a 6-mm-long USHD is characterized inside a blood vessel phantom with flow rate of 6 mm/s to 20 mm/s. (B) The frequency response of the USHD is tested when the USHD swims against fluid flow with different flow rates. (C) The frequency response of the USHD is tested when the USHD swims along fluid flow with different flow rates. The magnitude of the magnetic field at the position of the USHD is 5 mT. Average speed of the USHD is calculated from 5 trials at each frequency.

3.2 Problem Formulation

For USHDs that swim against and along the flow inside fluid-filled blood vessels and are localized using ultrasound images, designing a control system is a critical component of motion planning. The purpose of the control system is to render a certain compact set positively invariant and asymptotically attractive under the influence of bounded fluid drag and bounded measurement noise. We consider the fluid drag as a uniformly bounded disturbance force on the USHD. We also consider that the relationship between the penetration depth of the blood vessel phantom and the CNR affects the measured output of the USHD.

3.2.1 System Description

The USHD is controlled using the PMR system with three degree-of-freedom (3-DOF), which can control the field rotation-axis of the rotating magnetic field. In the PMR system, a time-periodic magnetic field is applied to the USHD, and the magnetization of the USHD ultimately aligns with the magnetic field. During experiments, the USHD translates by propulsive force combined with a magnetic pulling force, and the translation velocity of the USHD can be controlled by adjusting the angular frequency of the rotating magnetic field. When a USHD swims inside a confined environment, it is subjected to different forces, where a magnetic force and propulsive force will be produced and balanced by hydrodynamic drag force and friction force. This nonlinear system can be described by the following state-space representation:

$$\dot{\boldsymbol{x}} = \mathbf{A}\boldsymbol{x} + \mathbf{B}\phi(\boldsymbol{x}, d, u), \tag{3.1}$$

$$\boldsymbol{y} = \mathbf{C}\boldsymbol{x} + \zeta, \tag{3.2}$$

$$u = \gamma(\boldsymbol{x}), \tag{3.3}$$

where $\boldsymbol{x} = [x_1\ x_2]^T$ is the USHD state vector. Further, x_1 and x_2 represent the position and velocity of the USHD, $\boldsymbol{y}$ is the measured output, and u is the control input. $\mathbf{A} \in \Re^{2\times 2}$ is coefficient matrix, $\mathbf{B} \in \Re^{2\times 1}$ is input distribution vector, and $\mathbf{C} \in \Re^{1\times 2}$ is output vector. The input d represents the exogenous signal [170] caused by bounded flow rate, and ζ is the measurement noise caused by noise in ultrasound images (Fig. 3.3(A)). It is crucial to precisely control the USHD to reach the desired target position under

the influence of external signals and noise in ultrasound images. [171]. To quantify the noise of the USHD within ultrasound images, we calculate the CNR [172] of the USHD in blood vessel phantom at different penetration depths. The function ϕ includes magnetic, hydrodynamic, and mechanical dynamics of the USHD during motion inside the blood vessel phantom, as follows:

$$\phi(\boldsymbol{x}, d, u) = f_{\mathrm{m}} + f_{\mathrm{d}} + f_{\mathrm{p}} + f_{\mathrm{f}}, \tag{3.4}$$

where the magnetic force along 1-D blood vessel phantom scales as $f_{\mathrm{m}} \sim 3\mu_0\|\mathbf{m}\|\|\mathbf{M}\|/2\pi x_1^4$, μ_0 is the permeability of free space, $\mathbf{m}$ is the magnetic dipole moment of the USHD, and $\mathbf{M}$ is the magnetic dipole moment of the permanent magnet in the PMR system [173]. Note that f_{m} changes sign with x_1, and qualitatively the contribution of the magnetic force is not expected to assist propulsion when the USHD swims past the between two permanent magnets (Fig. 3.1(A)). The drag force is expressed as $f_{\mathrm{d}} = \frac{1}{2}\rho_{\mathrm{f}} A C_{\mathrm{d}} (x_2 - v_{\mathrm{f}})^2$, where C_{d} is the drag coefficient of the USHD, ρ_{f} is the density of fetal bovine serum (FBS), v_{f} is the flow rate of FBS, and A is the cross-sectional area [14]. In the case of locomotion of the USHD, we calculate the Reynolds number ($R_e = \frac{\rho_{\mathrm{f}} x_2 l_{\mathrm{t}}}{\mu}$) in the range of 1-10, where μ is the viscosity of FBS and l_{t} is the length of the USHD [174]. At this level of R_e, C_{d} is asymptotically proportional to ${R_e}^{-1}$. The propulsive force along axis of rotation is given by $f_{\mathrm{p}} = k_{\mathrm{t}}\omega$, where k_{t} is the thrust coefficient [169], and f_{p} is valid below the step-out frequency of the USHD, and the step-out frequency is directly proportional to the magnetic moment and the magnetic field strength and inversely proportional to the viscosity of fluid. The friction force $f_{\mathrm{f}} = \mu_{\mathrm{f}} f_{\mathrm{w}}$ is proportional to the apparent weight $f_{\mathrm{w}} = (\rho_{\mathrm{r}} - \rho_{\mathrm{f}}) g V_{\mathrm{r}}$, where μ_{f} is the friction coefficient, ρ_{r} is the density of the USHD, V_{r} is the volume of the USHD, and g is acceleration due to gravity [14].

In 1-D blood vessel phantom, the proportional-derivative (PD) controller $u = \gamma(\boldsymbol{x}) = -k_{\mathrm{p}}(x_1 + \zeta) - k_{\mathrm{d}}(x_2 + \dot{\zeta})$ is used so that it can control the USHD inside the blood vessel phantoms. When the USHD swims between two rotating permanent magnets, the magnetic force does not play a role because it is located in the uniform field region. By the setting $\dot{x}_1 = \dot{x}_2 = 0$, we can obtain the equilibrium point [175], as follows:

$$(x_1, x_2) = \left(\frac{\rho_{\mathrm{f}} A C_{\mathrm{d}} {v_{\mathrm{f}}}^2}{2k_{\mathrm{p}}} - \zeta - \frac{k_{\mathrm{d}}}{k_{\mathrm{p}}}\dot{\zeta} + \mu_{\mathrm{f}} \frac{(\rho_{\mathrm{r}} - \rho_{\mathrm{f}}) g V_{\mathrm{r}}}{k_{\mathrm{p}}},\ \ 0 \right). \tag{3.5}$$

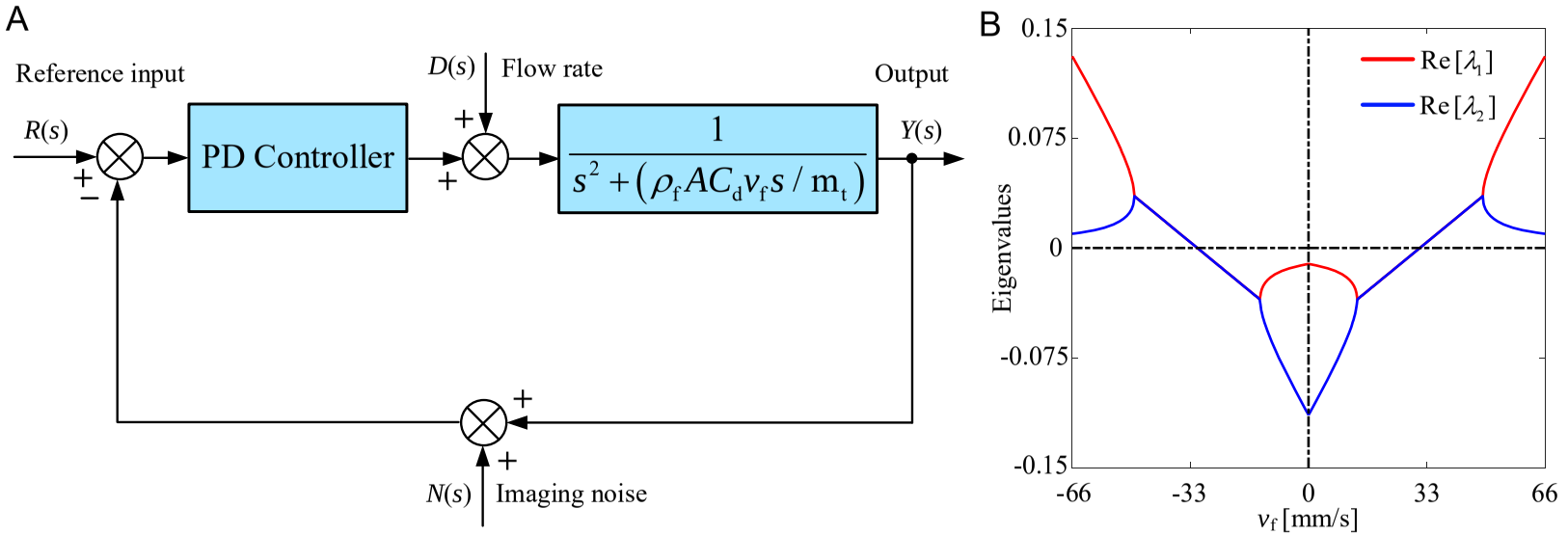

Figure 3.3: The closed-loop control of the USHD. (A) The USHD dynamics is obtained by balancing the drag force, magnetic force, propulsive force and friction force. $R(s)$ and $Y(s)$ represent the system reference input and system output, respectively. The fluid drag is modeled as a uniformly bound disturbance input $D(s)$, and $N(s)$ is the measurement noise due to ultrasound imaging. $\mathrm{m_t}$ is the mass of the USHD. (B) Bifurcation diagram for the real part of eigenvalues of closed-loop control system. At the equilibrium point of the closed-loop control system, the eigenvalues of Jacobian matrix can be calculated. In a small neighborhood of the equilibrium point, the closed-loop control system is stable, when the flow rate is less than a certain value. The upper bound of the disturbance caused by the fluid drag can be estimated. The positive flow rates show that the USHD swims against the flow, and the negative flow rates show that the USHD swims along the flow.

Equation (3.5) shows the influence of the fluid flow and the measurement noise in ultrasound images at the equilibrium point. The equilibrium point can also be shifted using the gains of the control system. At the equilibrium point of the closed-loop control system, we can calculate the eigenvalues of the Jacobian matrix of the closed-loop control system, as shown in Figure 3B. Within a specific flow rate in the range of 31 mm/s, the real part of the eigenvalues of the Jacobian matrix is negative. Therefore, the equilibrium point is stable in a certain compact set. Further, we implement the closed-loop control of the USHD in physiological fluid with dynamic flow rates based on eigenvalue analysis. Note that the structure for model (3.1)-(3.3) includes magnetically actuated devices immersed in a fluid and the characteristics of the actuating field and the surrounding fluid are known a priori. However, the input signals d and ζ may not be known. Therefore, the response of the USHD is characterized against and along the flow to determine its bounded behavior. Likewise, the localization gap between the USHD and the ultrasound probe is varied to increase the noise in the ultrasound images.

3.3 Characterization and Motion Control Experimental Results

A PMR system is used to actuate the USHD inside the blood vessel phantoms, and a pulsation pump is utilized to provide different flow rates. In addition, the ultrasound imaging system is employed to track the USHD inside the blood vessel phantoms, and closed-loop control system is constructed based on ultrasound feedback. Characterization of the frequency response and closed-loop motion control experiments are conducted using the above mentioned systems.

3.3.1 Experimental Setup

Three servo motors (MX-106R Dynamixel, Robotics, South Korea) are used to control the pitch angle, yaw angle, and translational DOF of the mobile platform, as shown in Fig. 3.2(A). Two permanent magnets (NdFeB, R750F, Amazing Magnetic LLC, California, U.S.A) with diameter of 45 mm and thickness of 30 mm, are fixed to two DC motors (Maxon 47.022.022-0019-189 DC Motor, Sachseln, Switzerland). The orientation and position

Table 3.1: Specification of the Untethered small-scale helical device (USHD) and the permanent-magnet robotic (PMR) system. d_{t} and l_{t} are diameter and length of the USHD, respectively. $\mathbf{m}$ is the magnetic dipole moments of the USHD. L_{d} is the distance between the two permanent magnets, H_{m} is the vertical distance between the pitch joint and the two permanent magnets, and H_{b} is the vertical distance from the pitch joint to the mobile platform. $\mathbf{M}_{1,2}$ is magnetic dipole moments of two permanent magnets. f is frequency of ultrasound waves, and Gn is gain of ultrasound system. d_{v} is the diameter of the blood vessel phantom. $\mathbf{B}_{\mathrm{m}}$ is magnetic strength between two permanent magnets. ρ_{f} and μ are the density and viscosity of physiological fluid, respectively. C_{d} is the drag coefficient, and R_e is Reynolds number. f_{m}, f_{d}, f_{p} and f_{f} are the magnetic force, drag force, propulsive force and friction force.

Parameter	Value	Parameter	Value	Parameter	Value	Parameter	Value
$d_{\mathrm{t}} \times l_{\mathrm{t}}$ [mm]	1.5×6	$\mathbf{m}$ [A.m^2]	6.23×10^{-4}	Pitch [mm]	1	Helicity [$\circ$]	71
L_{d} [mm]	350	H_{m} [mm]	164	H_{b} [mm]	240	$\mathbf{M}_{1,2}$ [A.m^2]	52.26
f [MHz]	13.3	Gn	42	d_{v} [mm]	4	$\mathbf{B}_{\mathrm{m}}$ [mT]	5
ρ_{f} [kg/m^3]	906	μ [mPa.s]	1.105	C_{d}	0.02	R_e	1-10
f_{m} [N]	$\mathcal{O}(10^{-6})$	f_{d} [N]	$\mathcal{O}(10^{-7})$	f_{p} [N]	$\mathcal{O}(10^{-6})$	f_{f} [N]	$\mathcal{O}(10^{-7})$

of the two DC motors are controlled independently to change the pitch angle and yaw angle of the USHD. The USHD (Fig. 3.1(B)) with length of 6 mm and diameter of 1.5 mm is fabricated through 3D printing using polylactic acid filament (PrimaValue, 3D Printers, The Netherlands). A cylindrical NdFeB magnet with diameter of 1 mm and length of 1 mm is attached to the USHD. A transducer (SonixTouch Q+, BK Medical, Quickborn, Germany) is mounted to another robotic base with 3-DOF, which can change the position of ultrasound probe based on the centerline of blood vessel phantoms. In addition, a pulsation pump (HV-77910-55, Masterflex, Illinois, U.S.A) is used to provide fluid flow with different rates, and the physiological fluid is FBS (F7524–500ML, Sigma-Aldrich, U.S.A). Demineralized water and gelatine powder (Ec Nnr: 232-554-6, Boom BV, Rabroekenweg, The Netherlands) are used to prepare the agar gel [176], and the mixture is contained inside a reservoir. Specifications of the USHD and the PMR system are described in Table 3.1.

3.3.2 Frequency Response Characterization

Frequency response characterization is implemented to understand the relation between the locomotion speed and actuation frequency of the PMR system, which is influenced by fluid flow. In the frequency response characterization, flow rates of 6 mm/s to 20 mm/s are tested, which is greater than the minimum flow rate in the venous system [131]. In the cases of locomotion against flow rates of 6 mm/s, 13 mm/s, and 20 mm/s, the locomotion speed of the USHD increases linearly with the actuation angular frequency within a certain range, as shown in Fig. 3.2(B). However, the speed of the USHD will not increase when the angular frequency increases to 32π rad/s. We attribute this phenomenon to the USHD does not follow the magnetic field lines at high angular frequencies. Therefore, the step-out angular frequency is 32π rad/s when the USHD swims against flow. The similar response characterizations are observed when the USHD swims along flow rates of 6 mm/s, 13 mm/s, and 20 mm/s, as shown in Fig. 3.2(C). The frequency response characterization of the USHD indicates its capability to achieve bidirectional locomotion in maximum flow rate of 20 mm/s. In the closed-loop control system, the actuation angular frequency is limited below step-out frequency.

3.3.3 Motion Control Results

In motion control experiments, the feedback provided by the ultrasound system is used to track the USHD. The ultrasound system is set to B-mode to display a sequence of rapidly acquired images at frame rate of 18 Hz, and the gain of the ultrasound system and frequency of the propagating waves are set to 42 and 13.3 MHz in all motion control trials. The communication between the PMR system and the ultrasound system is implemented in real-time using open-source libraries OpenIGTLink (version 3.1.0) [177].

Before implementing the closed-loop motion control of the USHD, the blood vessel phantom centerline is determined so that we can plan the motion path of the USHD. We accomplish centerline registration of the blood vessel phantoms using ultrasound images, during which the position of the ultrasound probe is controlled to scan the cross-section of the blood vessel phantom, as shown in Fig. 3.4(A,B,C). Therefore, we can obtain the centerline based on the position of the ultrasound probe and the cross-section of the blood vessel phantom with a bifurcation, as shown in Fig. 3.4(D). Further, a PD controller is used to calculate the angular speed ω of the dipole

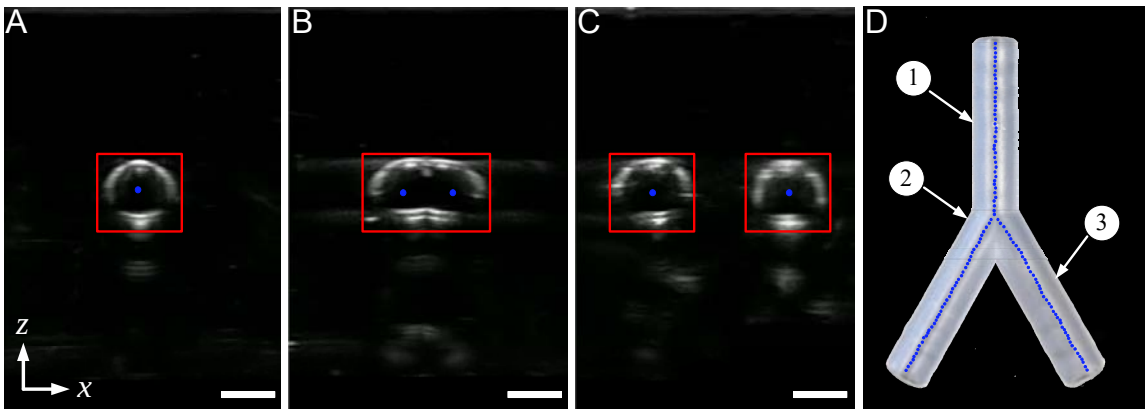

Figure 3.4: Acquisition of the USHD motion path. (A) The ultrasound probe is used to scan the cross-section of position ① in the blood vessel phantom. (B) The ultrasound probe is used to scan the cross-section of position ② in the blood vessel phantom. (C) The ultrasound probe is used to scan the cross-section of position ③ in the blood vessel phantom. (D) The motion path of the blood vessel phantom with a bifurcation is constructed using the cross-section of the blood vessel phantom and the position of the ultrasound probe. All scale bars are 4 mm.

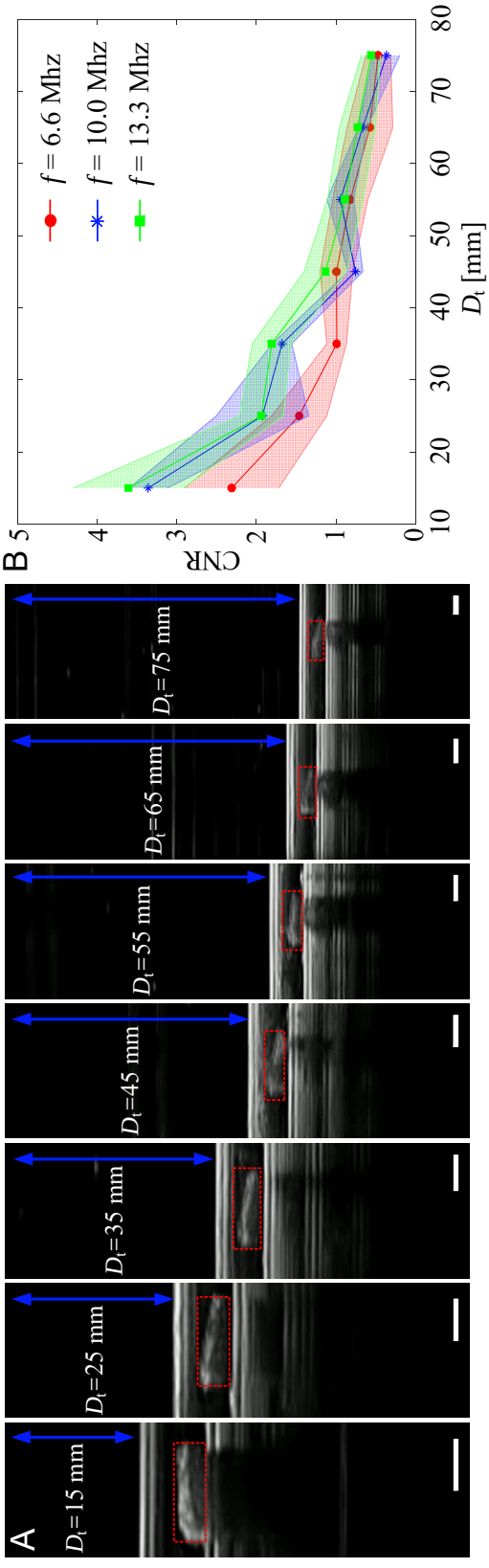

Figure 3.5: The USHD visibility in the ultrasound images. (A) At different penetration depths (D_t), the B-mode of ultrasound system is used to observe the USHD. All scale bars are 5 mm. (B) The contrast-to-noise ratio (CNR) is calculated for the USHD at different penetration depths and different ultrasound waves frequencies. All error bars denote the standard deviation from 5 trials.

fields. The angle $\angle\mathbf{B}^{\mathrm{d}}(\mathbf{p})$ of the desired rotating magnetic fields is constructed using the point-dipole approximation (3.6) and the homogenous transformation (3.7), when the USHD swims inside a blood vessel phantom with a bifurcation (Please refer to Appendix). Therefore, the direction of the magnetic dipole moment of two permanent magnets is constructed using the joint space coordinates. Further, we implement an OpenCV (version 3.4.9) image processing library to detect and track the USHD in each ultrasound system frame, and the template image is updated in real-time during each trial [178]. The control strategy is implemented in C++ on a computer running Linux Ubuntu 16.04.

The CNR is used to quantify the USHD visibility in the ultrasound images, as shown in Fig. 3.5(A). The CNR decreased with the increase of penetration depths in the ultrasound images. Note that the high CNR is measured when high-frequency ultrasound waves are used, as shown in Fig. 3.5(B). In order to localize the position of the USHD and then construct a closed-loop control system, a high CNR is required. Therefore, a closed-loop control system is constructed to navigate the USHD in the 1-D blood vessel phantom with different dynamic flow rates under the condition of penetration depth 15 mm, 25 mm and 35 mm, as shown in Fig. 3.6. For different flow rates and different penetration depths, we observe that all states of the closed-loop control system asymptotic converge to the reference position, as shown in Fig. 3.6(A,D,G). We also observe that the position errors and the measured x_2-component of the closed-loop control system increase with the penetration depths, as shown in Fig. 3.6(B,E,H). The measured position error and x_2-component increase for different flow rates owing to the decrease of the CNR with penetration depths. In upstream and downstream fluid, Fig. 3.6(C,F,I) show motion of the USHD from starting point toward a reference position at different penetration depths. During the experiments, the ultrasound images are acquired at a rate of 18 fps, and the execution time of the template matching method for a single ultrasound image is 0.24 ± 0.09 s [179]. Therefore, we need to control the swimming velocity of the USHD by adjusting the gain of the controller, which is essential for ultrasound system tracking because an over-fast navigation velocity impairs tracking accuracy. In dynamic flow conditions, experimental results demonstrate that our proposed control system can stably navigate the USHD to the reference position under the interference of external bounded flow rate and ultrasound image noise.

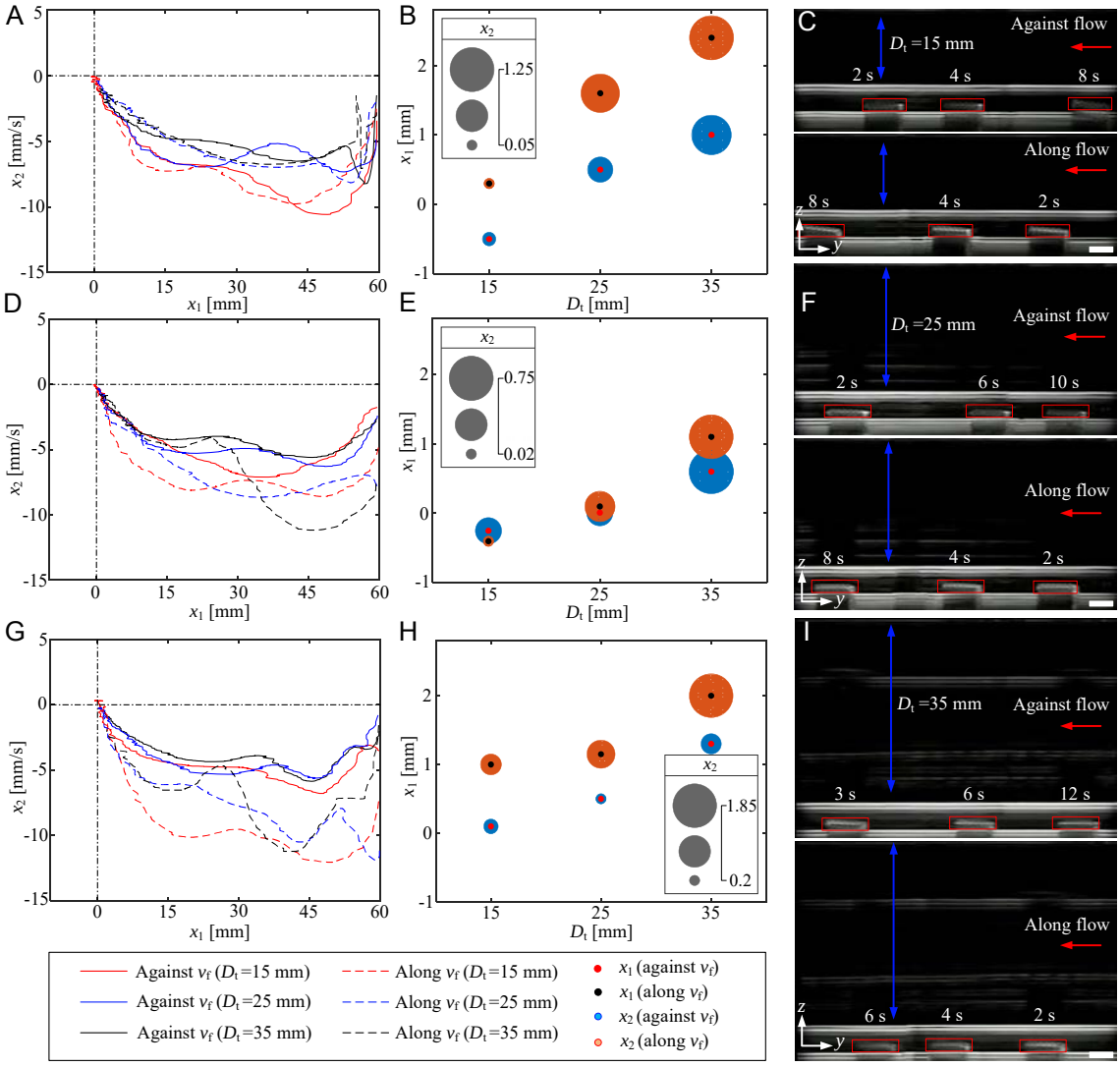

Figure 3.6: Closed-loop control characterization of the USHD against and along the flow. (A) At different penetration depths (D_t), the state of closed-loop control system is convergent when the flow rate is 6 mm/s. (B) For $v_f = 6$ mm/s, closed-loop control system state deviation. (C) For $v_f = 6$ mm/s, the USHD swims against and along the flow toward the reference position at penetration depth of 15 mm. (D) At different penetration depths, the state of closed-loop control system is convergent when the flow rate is 13 mm/s. (E) For $v_f = 13$ mm/s, closed-loop control system state deviation. (F) For $v_f = 13$ mm/s, the USHD swims against and along the flow toward the reference position at penetration depth of 25 mm. (G) At different penetration depths, the state of closed-loop control system is convergent when the flow rate is 20 mm/s. (H) For $v_f = 20$ mm/s, closed-loop control system state deviation. (I) For $v_f = 20$ mm/s, the USHD swims against and along the flow toward the reference position at penetration depth of 35 mm. The red arrow indicates the direction of fluid flow. All scale bars are 5 mm. *Please refer to the supplementary video.*

The closed-loop control results inside the 1-D blood vessel phantom are summarized in Table 3.2.

Fig. 3.7 shows that the USHD can be controlled to navigate inside a blood vessel phantom with a bifurcation under ultrasound image noise and bounded flow rate. In the case of the flow rate of 20 mm/s and penetration depth of 25 mm, the USHD swims upstream along paths 1 and 2, as shown in Fig. 3.7(A). For path 1, the angle of the rotating magnetic field can be changed using the joint space coordinates of the PMR system, as shown in Fig. 3.7(B), and the motion of the USHD at this moment is shown in Fig. 3.7(E). In the motion of locomotion upstream, the mean position errors along paths 1 and 2 are measured as 0.86 ± 0.44 mm and 1.52 ± 0.17 mm, respectively. Similarly to Fig. 3.7(A), the USHD is controlled in the downstream fluid along paths 1 and 2, as shown in Fig. 3.7(C). For path 2, the angle of the rotating magnetic field can be changed when the USHD swims along flow rate inside the bifurcation blood vessel phantom, as shown in Fig. 3.7(D), and the motion of the USHD at this moment is shown in Fig. 3.7(F). In the case of motion of locomotion downstream, the mean position errors along paths 1 and 2 are measured as 1.78 ± 0.19 mm and 0.87 ± 0.53 mm, respectively. With the proposed control strategy, we can overcome the disturbance and accurately navigate the USHD to the correct path under ultrasound guidance. The closed-loop control results in a blood vessel phantom with a bifurcation are summarized in Table 3.3.

Regardless of the 1-D blood vessel phantom or a blood vessel phantom with a bifurcation, our experimental results demonstrate that the proposed strategy allows us to control the motion of the USHD without any additional computational burden, and can be used readily to perform feedback control algorithms. By applying the proposed closed-loop motion control, we can navigate the USHD inside the blood vessel phantoms, indicating that the medical imaging guided the USHD has great potential for performing automated delivery and targeted therapy in dynamic environments.

3.4 Discussion

Motion control of the USHDs has the potential for improved biomedical applications. In this work, we report a closed-loop control strategy to navigate the USHD in physiological fluid with dynamic flow rates using ultrasound imaging. Compared with other USHD in the blood vessel phantom [14],

Table 3.2: At different penetration depths (D_t), closed-loop control of the USHD is implemented inside a 1-D blood vessel phantom against and along fluid flow of 6 mm/s, 13 mm/s, and 20 mm/s. The mean position error (MPE) in each case is calculated from 5 motion control trials.

Flow rate	Navigation	$D_t = 15$ mm	$D_t = 25$ mm	$D_t = 35$ mm
6 mm/s	Against flow MPE [mm]	0.66 ± 0.18	0.92 ± 0.50	0.74 ± 0.56
	Along flow MPE [mm]	0.43 ± 0.21	1.26 ± 0.42	1.99 ± 0.55
13 mm/s	Against flow MPE [mm]	0.26 ± 0.14	0.59 ± 0.52	0.85 ± 0.63
	Along flow MPE [mm]	0.51 ± 0.30	0.55 ± 0.18	1.13 ± 0.43
20 mm/s	Against flow MPE [mm]	0.30 ± 0.21	0.71 ± 0.16	0.96 ± 0.51
	Along flow MPE [mm]	0.79 ± 0.43	1.20 ± 0.36	1.90 ± 0.37

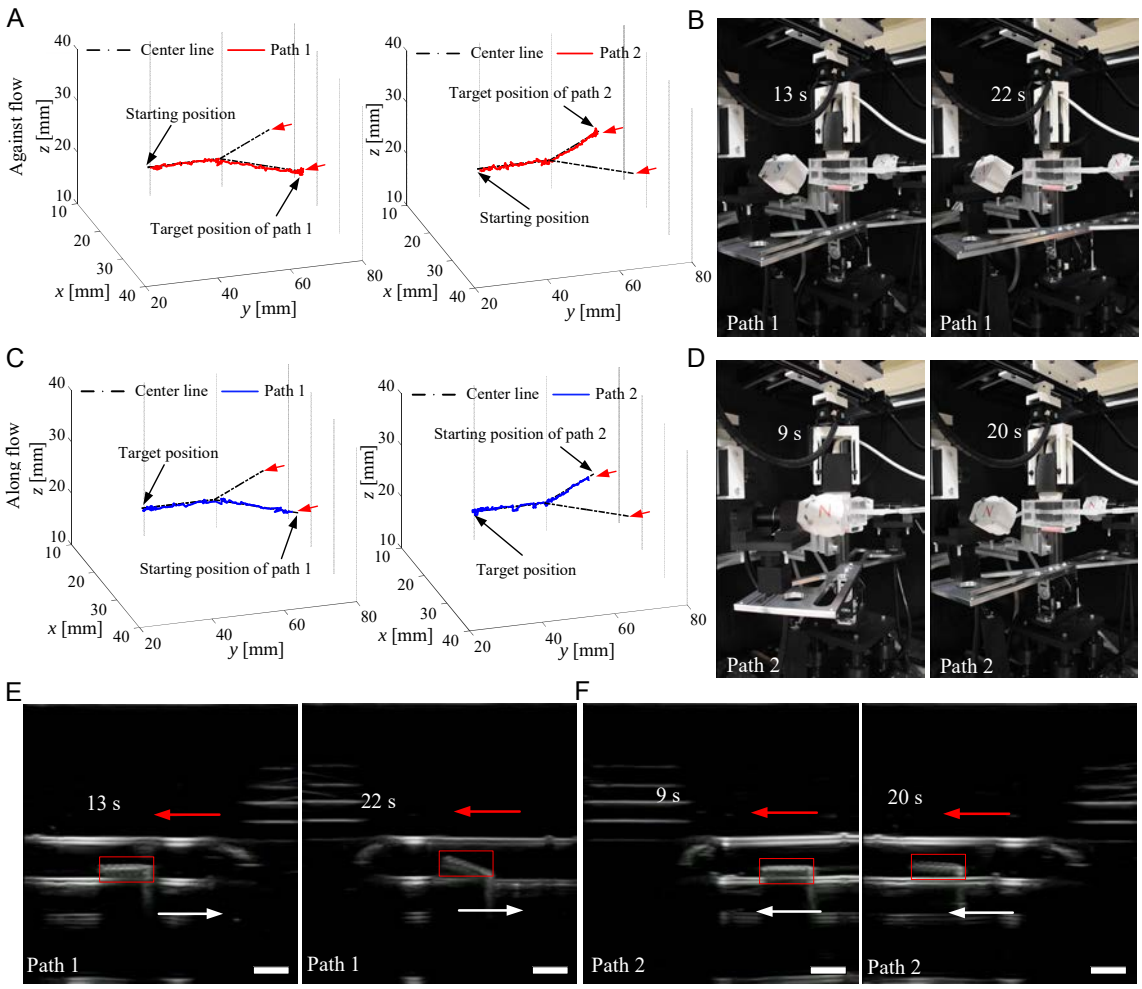

Figure 3.7: The USHD is controlled inside a blood vessel phantom with a bifurcation, when the flow rate is 20 mm/s and the penetration depth is 25 mm. (A) In the upstream physiological fluid, the USHD swims towards the target position along paths 1 and 2, respectively. (B) The PMR system configurations at two time instants during the navigation in path 1: 13 s and 22 s. (C) In the downstream physiological fluid, the USHD swims towards the target position along paths 1 and 2, respectively. (D) The PMR system configurations at two time instants during the navigation in path 2: 9 s and 20 s. (E) The USHD is controlled against the flow to swim toward the target position inside path 1. (F) The USHD is controlled along the flow to swim toward the target position inside path 2. The white arrow indicates the direction of motion of the USHD, and the red arrow indicates the direction of fluid flow. All scale bars are 5 mm. *Please refer to the supplementary video.*

Table 3.3: At penetration depths of 25 mm and flow rate of 20 mm/s, closed-loop control of the USHD is implemented inside the bifurcation blood vessel phantom against and along fluid. The MPE in each path is calculated from 5 motion control trials.

Flow rate	Navigation	Path 1	Path 2
20 mm/s	Against flow MPE [mm]	0.86 ± 0.44	1.52 ± 0.17
	Along flow MPE [mm]	1.78 ± 0.19	0.87 ± 0.53

[80], [161], we model the dynamic flow as the bounded exogenous disturbance signal and quantify the ultrasound images noise using CNR, and then we analyze closed-loop control characterization of the USHD inside a blood vessel phantom at different penetration depths with dynamic flow. In addition, our PMR system has large workplace, and we don't need to consider the problem of electromagnetic coil heating, so it can be used to drive the USHD for a long time. However, motion control and the localization and biomedical applications of the USHD remain challenging for the *in vivo* condition. The biological hybrid USHD seems an ideal choice considering the need for biocompatibility and biodegradability for *in vivo* tasks. The USHD could be fabricated by combining magnetic nanoparticles and biocompatible materials, such as gelatin methacryloyl and hyaluronic acid-methacryloyl, thus showing promising potential for biomedical applications. In the venous environment, average flow rates of blood are approximately in the range from 5 mm/s to 50 mm/s, and blood flow rates of aorta and medium artery system are greater than venous blood flow rates [131]. In our experiments, the maximum flow rate of a blood vessel phantom is 20 mm/s, which is four times as large as the minimum flow rate in the venous system. However, under high flow rate conditions, the propulsive thrust generated by rotating of helical body is not sufficient to move against high flow rates. Therefore, it is essential to improve the performance of the magnetic system by incorporating permanent magnets with relatively large magnetic field. A large rotation magnetic field is able to increase the torque on the USHD, thereby improving the frequency response characteristics of the USHD. In addition, the large magnet could increase the magnetic force, which could

be managed to improve the propulsion of the USHD. The USHD could be designed with more magnetic material to improve its magnetic moment, further increasing the USHD's thrust against high flow rates.

In ultrasound system, the tunning of the frequency of the ultrasound waves depends on a trade-off between the penetration depth and the axial resolution. High-frequency ultrasound waves give greater axial resolution than low-frequency ultrasound waves. In contrast, high-frequency ultrasound waves do not allow adequate penetration. In our experiments, the selected penetration depths are 15 mm, 25 mm, and 35 mm, as shown in Fig. 3.5, which are similar to depths of superficial veins of the legs. Their depths are estimated to vary from 2 mm to 30 mm in the region of the anterior thigh in adults [180]. In addition, the diameter of blood vessel phantom is 4 mm, and the diameter and length of the USHD are 1.5 mm and 6 mm, respectively. Under this condition, 13.3 MHz ultrasound wave is used to localize a magnetic USHD in the millimeter scale. However, if we navigate the USHD inside small diameter vessels such as venules and capillaries, smaller dimensions must be used for the USHD. Therefore, the ultrasound waves with high-frequency will be utilized to detect the micrometer scale USHD. Further, the microrobot will not be able to be localized, when the penetration depth is increased to 80 mm [159]. We can also observe that CNR decreases with increasing penetration depth, as shown in Fig. 3.4. Therefore, the penetration depth and the size of the USHD could represent limitations for minimally invasive ultrasound localization techniques.

Motion control of the USHD has been validated inside blood vessel phantoms with dynamic flow rates. Therefore, in venous systems with low flow rates, the USHD has the potential to be used for medical applications. The formation of blood clots could cause local ischemia, which causes tissue to lack oxygen, and irreversible damages could occur quickly. Therefore, mechanical removal of blood clots is a promising approach using the USHD, which could provide high removal rates of blood clots compared to pharmacological thrombus dissolution [83]. Additionally, targeted drug delivery using the USHD is a promising technique capable of overcoming the limitations of conventional chemotherapy that relies on body circulation [181].

3.5 Conclusions and Future Work

Closed-loop motion control system of the USHD is designed using the PMR system and an ultrasound imaging system. By means of this control system, we are able to study the closed-loop control characteristics of the USHD in a physiological fluid with dynamic flow rates, and achieve asymptotic convergence inside the blood vessel phantoms. The frequency response results show that the locomotion speed of the USHD varies linearly with the actuation frequency below the step-out frequency, regardless of the direction of flow fluid. In addition, the USHD can overcome flow rate of 20 mm/s, which is four times as large as the minimum flow rate in the venous system. The experimental results demonstrate that ultrasound imaging can detect and track the USHD inside both a blood vessel phantom at different penetration depths and a blood vessel phantom with a bifurcation. In all closed-loop control experiments, the maximum position error of the USHD is 1.99 ± 0.55 mm.

As part of future studies, the USHD will be controlled inside a 3-D vascular network phantom, and *ex vivo* experiments will be implemented. Our closed-loop control experiments are conducted against and along fluid flow with flow rate of 6 mm/s, 13 mm/s, and 20 mm/s. This flow rate is greater than blood-flow in small arterioles, capillaries, and venules. However, blood-flow in veins with higher flow rates, the aorta, and arteries are higher than the flow rate used in this study. If the USHD can move against greater flow rates, it is necessary to improve the performance of our the PMR system by incorporating permanent magnets with relatively large magnetic field.

3.6 Appendix

The USHD is driven by two synchronized rotating dipole fields. These fields are produced by rotating permanent magnets that are position controlled using a robotic system, as shown in Fig. 3.2(A). The PMR system has 3-DOF, pitch angle (θ) that describes the rotation about the intersection of the plane ($y_0 = 0$ mm) and the plane ($z_0 = 240$ mm), and yaw angle (α) that describes the rotation about the z_0-axis, and these 2-DOF are fixed to a linear mobile platform that translates along the y_0-axis. The moving distance of the mobile platform is represented by L in the global reference

frame, $\{x_0, y_0, z_0\}$. Therefore, motion of the permanent magnet is defined using the joint space coordinates, $\mathbf{q} = (\theta,\ \alpha,\ L)^T$. Each field is modeled according to the following point-dipole approximation [84]:

$$\mathbf{B}_i(\mathbf{p}) = \frac{\mu_0}{4\pi|\mathbf{p}|^3}\left(\frac{3(\mathbf{M}_i \cdot \mathbf{p})\mathbf{p}}{|\mathbf{p}|^2} - \mathbf{M}_i\right) \qquad i = 1,\ 2, \tag{3.6}$$

where $\mathbf{p}$ is the position vector of the USHD with respect to the rotating permanent magnet, and $\mathbf{p}$ can be obtained by the output $\boldsymbol{y}$ of the system, and $\mathbf{M}_i$ denotes the magnetic dipole moment of ith permanent magnet.

To control the magnetic field in Equation (3.6), the direction of the magnetic dipole moment $\mathbf{M}_i$ of the permanent magnet is periodically varied and its rotation axis is controlled. The magnetic moment $\mathbf{M}_i$ can be constructed using the joint space variable $\mathbf{q}$ as follows:

$${}^0\mathbf{T}_i^3(\mathbf{q}) = \begin{pmatrix} {}^0\mathbf{R}_i^3 & {}^0\mathbf{p}_i^3 \\ 0_{1\times 3} & 1 \end{pmatrix} \qquad i = 1,\ 2, \tag{3.7}$$

where ${}^0\mathbf{T}_i^3(\mathbf{q})$ represents ith homogenous transformation matrix from the frame of reference of the ith permanent magnet to the global reference frame. Note that ${}^0\mathbf{T}_i^3(\mathbf{q})$ completely characterize the position and orientation of the ith permanent magnet based on the joint variables of the system. In Equation (3.7), the rotation matrix of the ith permanent magnet with respect to the global reference frame is given by

$${}^0\mathbf{R}_i^3 = \begin{pmatrix} \cos\alpha & -\sin\alpha\cos\theta & -\sin\alpha\sin\theta \\ \sin\alpha & \cos\alpha\cos\theta & \cos\alpha\sin\theta \\ 0 & -\sin\theta & \cos\theta \end{pmatrix}. \tag{3.8}$$

The position vector of the ith permanent magnet with respect to the global reference frame is given by

$${}^0\mathbf{p}_i^3 = \begin{pmatrix} (-1)^i L_\mathrm{d}\cos\alpha/2 - H_\mathrm{m}\sin\alpha\sin\theta \\ L + (-1)^i L_\mathrm{d}\sin\alpha/2 + H_\mathrm{m}\cos\alpha\sin\theta \\ H_\mathrm{b} + H_\mathrm{m}\cos\theta \end{pmatrix}, \tag{3.9}$$

where L_d indicates the distance between the rotating permanent magnets. If the magnetic force is required to be increased to assist actuation, then this distance can be decreased. Note that decreasing this distance will also

affect the magnetic torque and the step-out frequency of the USHD will be increased. In Equation (3.9), H_{m} is the vertical distance between the joint that controls the pitch and the two permanent magnets, and H_{b} represents the vertical distance from the joint that controls the pitch to the mobile platform. In contrast to L_{d} which can be used to increase the magnetic force and magnetic torque, H_{m} and H_{b} do not change the magnitude of the magnetic field and gradient in the workspace.

We assume that the magnetization of the USHD ultimately aligns with the magnetic field. Consequently, the relationship between the magnetization of the USHD and the magnetic field is as follows:

$$\angle \mathbf{m} := \angle \mathbf{B}(\mathbf{p}). \tag{3.10}$$

The relationship between the applied field and the orientation of the USHD can be used to design a closed-loop control system to change field rotation axis and orients it toward the desired reference position. In this case, a prescribed trajectory along the vessel will provide waypoints. Further, a position error vector is defined as follows:

$$\mathbf{e} = \mathbf{p}_{\mathrm{ref}} - \mathbf{p}, \tag{3.11}$$

where $\mathbf{p}_{\mathrm{ref}}$ is the reference position of the blood vessel phantom, and the PD controller $u = -k_{\mathrm{p}}|\mathbf{e}| - k_{\mathrm{d}}|\dot{\mathbf{e}}|$ is further used to drive the USHD. Now, we turn to the direction of the field rotation axis to achieve directional control of the USHD. According to the point-dipole approximation3.6 and the direction error of the USHD inside a blood vessel phantom, the direction of the desired magnetic field is calculated using

$$\angle \mathbf{B}^{\mathrm{d}}(\mathbf{p}) = \tan^{-1}\left(\frac{|\mathbf{p}_{\mathrm{ref}} - \mathbf{p}|_x}{|\mathbf{p}_{\mathrm{ref}} - \mathbf{p}|_y}\right), \tag{3.12}$$

where $\angle \mathbf{B}^{\mathrm{d}}(\mathbf{p})$ represents the angle of the desired magnetic field, and $e_x = |\mathbf{p}_{\mathrm{ref}} - \mathbf{p}|_x$ and $e_y = |\mathbf{p}_{\mathrm{ref}} - \mathbf{p}|_y$ are the position error along the x- and y-axis, respectively. We can construct desired magnetic field $\mathbf{B}^{\mathrm{d}}(\mathbf{p})$ based on the angle of desired magnetic field $\angle \mathbf{B}^{\mathrm{d}}(\mathbf{p})$, and calculate the desired magnetic dipole moment $\mathbf{M}_i^{\mathrm{d}}$ using Equation (3.6). Then, the desired magnetic moment $\mathbf{M}_i^{\mathrm{d}}$ can be constructed using the joint control variable $\mathbf{q}$. Since the direction of the dipole moment $\mathbf{M}_i$ is perpendicular to the direction of the rotation axis of the magnetic field, the rotation axis is determined. The

desired control input $(\theta^{\mathrm{d}},\ \alpha^{\mathrm{d}},\ L^{\mathrm{d}})^T$ is controlled and updated based on the position of the waypoints along the prescribed centerline of the blood vessel phantom with a bifurcation.

Chapter Overview

By utilizing ultrasound guidance, the USHD demonstrates the capability to be controlled inside a 1-D vascular model with varying penetration depths, as well as in a 2-D model featuring bifurcations. While previous research has effectively showcased the movement of the USHD along these 1-D and 2-D paths, it's important to note that these paths do not accurately replicate the geometry of real blood vessels. Therefore, it becomes crucial to consider vascular models that faithfully represent anatomical structures. Furthermore, for achieving precise navigation of USHDs inside complex vascular networks, the reconstruction of intricate 3-D vascular geometry emerges as an indispensable foundational element.

In light of these considerations, **Chapter 4** introduces a novel closed-loop control strategy for the USHD using a PMR system inside a 3-D vascular model containing blood. The strategy involves reconstructing the 3-D vascular model from 2-D ultrasound images, extraction of regions of interest inside the 3-D vascular models, and implementing point-to-point closed-loop control of the USHD guided by real-time ultrasound images. The USHD then successfully navigates the pathways of the 3-D vascular model using the proposed control strategy. In addition, we evaluate the effectiveness and robustness of our system and the proposed control method.

4

Navigation of Untethered Small-Scale Helical Devices Using Magnetic System Under Ultrasound Guidance

Note: *Following chapter is adapted from the article "Navigation of Untethered Small-Scale Helical Devices Using Magnetic System Under Ultrasound Guidance" by* ***C. Li****, S. Misra, and I.S.M. Khalil, published in "IEEE Transactions on Medical Robotics and Bionics", vol. 5, no. 4, pp. 1093-1104, November 2023.*

Abstract

Magnetic actuation of untethered small-scale helical devices (USHDs) shows great potential for targeted drug delivery or as minimally invasive surgical tools in the human body. However, ensuring the success of therapeutic interventions in anatomically challenging regions, such as neck vascular networks with winding pathways and branching, demands the incorporation of precise image feedback and a robust control method. How to construct a control method with precise navigation ability in complex and hard-to-reach body districts is still a challenging work. In this paper, we propose a closed-loop control strategy for the USHD based on a permanent-magnet robotic (PMR) system inside a three-dimensional (3-D) vascular model with blood. First, the 3-D vascular model is reconstructed using 2-D ultrasound images. Second, the point-to-point closed-loop control of the USHD is performed under ultrasound guidance, and the control input is obtained to act

on both the PMR system and the ultrasound system. Next, the USHD navigates the different pathways of the 3-D vascular model under the proposed control strategy. Finally, our *in vitro* experimental results indicate that the maximum mean absolute position error between the target point of each branch and the actual position reached by the USHD (length and diameter of 6 mm and 1.5 mm, respectively) is 6.4±3.8 mm and 4.2±2.8 mm when the blood flow rate is 16.6 mL/min, which corresponds to 28% of the maximum venous flow rate.

4.1 Introduction

Vascular diseases are highly prevalent conditions, such as strokes and arteriosclerosis, which pose significant threats to human health [182]. Current treatments for vascular diseases, including drug therapy, vascular bypass graft, and carotid angioplasty, have adverse effects such as invasiveness, and potential complications [183]–[186]. To overcome the limitations of current treatments for vascular diseases, innovative devices such as untethered small-scale helical devices (USHDs) have been developed [81], [187], [188]. These miniature devices have potential impact in targeted and minimally invasive interventions, enabling precise navigation through intricate vascular networks and providing more effective and safer treatment than traditional methods [132], [189]. One promising approach to achieving the capabilities mentioned above is through the use of magnetically-driven USHDs [190]. By an externally applied rotating magnetic field, these USHDs can be controlled and guided inside the blood vessels, enabling them to navigate with high precision and maneuverability [175], [191]. The use of magnetism as a magnetic force or torque eliminates the need for tethers or external wires, allowing for minimally invasive procedures and reducing the risk of complications [192].

Recently, several studies have explored the potential of magnetic control of the USHD in various medical applications. For instance, Abbott *et al.* have showcased a method to generate a rotating magnetic field with any desired rotation axis using a single rotating magnet actuator to actuate a magnetic device [142]. They have also presented the kinematic model of a magnetic microrobot swarm operating within a single rotating magnetic field [86]. This model provides valuable insights into the motion state of the microrobot swarm, allowing us to better understand its collective

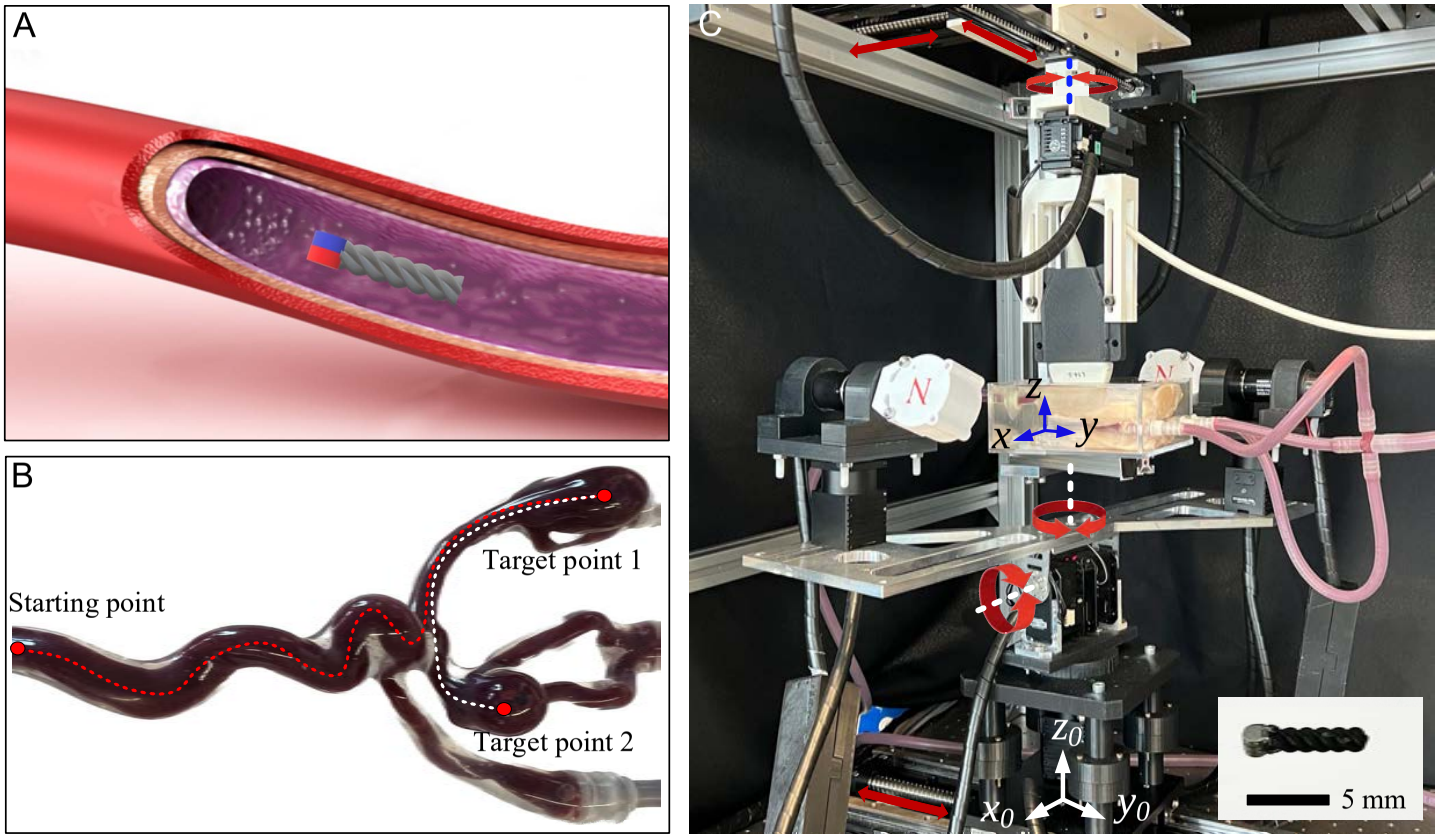

Figure 4.1: A permanent-magnet robotic (PMR) system for an untethered small-scale helical device (USHD) inside a 3-D vascular model. (A) The USHD is actuated inside the 3-D vascular model. (B) Two paths are planned in the 3-D vascular model, where the first path is from the starting point to the target point 1, and the second path is from the target point 1 to the target point 2. (C) The PMR system is used to actuate the USHD toward the target position in the 3-D vascular model, there are six degree of freedom (6-DOF) in the PMR system, where 3-DOF (pitch, yaw, and a linear motion stage) are used to control the position of two synchronously rotating permanent magnets fixed to two DC motors, and other 3-DOF (rotation and two linear motion stages) can control the position of the ultrasound probe in the global coordinate system $\{x_0, y_0, z_0\}$. The 3-D vascular model is fixed in the container and the phantom frame is indicated by $\{x, y, z\}$.

behavior. In addition, Alshafeei *et al.* have proposed a method by using synchronously rotating two permanent magnets to control a helical robot in a glass tube, resulting in the establishment of a relationship between the movement speed of the helical robot and the rotation frequency of the permanent magnet [193]. Furthermore, Mahdy *et al.* have utilized a helical robot to verify its characteristics of helical propulsion inside *in vitro* and *ex vivo* models of a rabbit aorta [194]. Moreover, Tan *et al.* have proposed a novel fabrication method to enhance the swimming performance of helical robots by leveraging the benefits of a robust magnetic head and a flexible deformable tail [195]. Liu *et al.* have proposed a closed-loop sliding mode control method by using electromagnetic actuation and visual feedback to enable the miniature helical swimmer to track the corresponding path and avoid obstacles, thereby improving the robustness of the entire system [196]. For the application of helical robots in medical treatment, Khalil *et al.* have proposed the use of a helical robot to clear blood clots and established the corresponding mathematical model and further used *in vitro* verification [114]. This research group has employed the helical robot to clear blood clots under ultrasound guidance [118]. Leclerc *et al.* also have proposed a control apparatus [197] to perform three-dimensional (3-D) path following and clear blood clots by using a miniature magnetic swimmer [113].

Although the above works have proposed many advanced methods and equipment, there is still room for improvement. For instance, the only basic screw characteristics of helical propulsion of the robot under two synchronously rotating permanent magnets have been studied [193], [194]. Furthermore, the researcher only has studied the 1-D motion of the helical robot and implemented a clear experiment of thrombus [114], [118]. Despite some previous work successfully showcasing the movement of helical robots along simplified 3-D paths and their related applications, these paths do not capture the geometry of the blood vessels. Hence, the vascular models that accurately represent anatomical structures should be considered. Moreover, to achieve precise navigation of USHDs inside blood vessels, the reconstruction of complex 3-D vascular geometry is an indispensable foundational element. In this context, ultrasound stands as the preferred imaging modality due to its non-invasive nature, ease of operation, and cost-effectiveness. Yang *et al.* have used an ultrasound system to scan cross-sectional views of the vascular model [80]. By utilizing the positional information obtained from the ultrasound probe and the 2-D ultrasound images, they have suc-

cessfully derived the centerline of the 3-D vascular model. Zhang *et al.* have also utilized an ultrasound system to scan the vascular model, thereby obtaining 2-D ultrasound images [178]. Subsequently, speckle noise within the subsequent ultrasound images has been removed using blur, dilation, and erosion filters, and then a 3-D point cloud of the vascular model has been generated by integrating the position of the ultrasound probe. Ruijter *et al.* have developed a general, robust, and accurate approach for segmenting the lumen-wall boundary of both healthy central and peripheral vessels within extensive field-of-view freehand ultrasound datasets [198]. This has been achieved by employing Convolutional Neural Networks, subsequently leading to the reconstruction of the vascular geometry. Taking inspiration from these works, we also employ an ultrasound system to reconstruct the 3-D vascular models, subsequently obtaining reference paths for the navigation of the USHD. In addition, performing minimally invasive surgery inside complex vascular networks requires a certain amount of space to ensure precision and effectiveness. Therefore, there is a need for advanced control strategies and devices that can navigate the complex and irregular paths of blood vessel networks, while providing sufficient working space for minimally invasive procedures.

In this paper, we investigate the movement of a USHD inside the 3-D vascular model using a permanent-magnet robotic (PMR) system guided by the ultrasound system, as shown in Fig. 4.1. In our experiments, the construction of a closed-loop feedback control system allows for real-time adjustments of the PMR system based on medical ultrasound images and predefined paths. This ensures that the USHD can accurately follow a predetermined trajectory inside the 3-D vascular model, minimizing the risk of deviation from the intended path. Compared to manual navigation of the USHD by interventional physicians, the use of the PMR system has the potential to provide more stable and consistent control for the USHD's movements, reducing the potential for errors caused by human factors such as fatigue or hand tremors. In addition, the use of a feedback control robotic approach also has the potential to reduce the burden on the interventionalist or radiologist while ensuring guidance precision. The main contributions of this paper are as follows:

(a) The integration of a mobile ultrasound imaging device with the PMR system allows for simultaneous localization and control of the USHD. This integration enhances the precision and accuracy of the navigation process

by providing real-time imaging feedback.

(b) A control method with robustness is constructed using the PMR system and the reconstructed 3-D vascular model based on 2-D ultrasound images, and the proposed approach is able to drive the USHD through complex and winding paths inside the 3-D vascular model.

(c) The research evaluates the locomotion performance of the USHD inside the 3-D vascular model under various blood flow velocities. This assessment provides insights into how the USHD behaves in different flow conditions, contributing to the understanding of the capabilities and limitations of the control method proposed.

The remainder of this paper is organized as follows: The blood flow field is analyzed and the 3-D vascular network model is reconstructed in Section 4.2. The PMR system is described, and closed-loop control of the USHD inside the 3-D vascular network model and experimental results are analyzed in Section 4.3. Section 4.4 provides discussions pertaining to the limitations and potential applications of the USHDs. Finally, Section 4.5 concludes and provides directions for future work.

4.2 3-D Vascular Model

The 3-D vascular model used in the experiment is described, as shown in Fig. 4.1(B). Two paths are planned in the 3-D vascular model. The first path is from starting point to target point 1 in path 1, the other path is from target point 1 to target 2. Our objective is to guide the USHD through path toward the target position. During the motion control experiment of the USHD, chicken tissue is used to cover the surface of the 3-D vascular model and the direction of blood flow in the 3-D vascular model is from right to left, as shown in Fig. 4.2(A).

4.2.1 Characterization of the Flow Field Inside the 3-D Vascular Model

In medical applications, Color-flow Doppler mode can be used to calculate the velocity of the fluid within the target area by measuring the Doppler frequency shift [199]. Therefore, we characterize the pulsatile blood flow field based on Doppler ultrasound imaging. The velocity of blood flow can vary throughout the vascular model. It typically follows a parabolic pro-

Figure 4.2: Blood flow field analysis inside the 3-D vascular model. (A) Chicken tissue covers the 3-D vascular model during closed-loop control of the USHD. (B) Ultrasound Doppler mode is used to measure blood flow velocity at locations ①, ②, and ③ when the flow rate of 33.3 mL/min is provided to the 3-D vascular model. (C) The blood velocity at position ① is measured. (D) The blood velocity at position ② is measured. (E) The blood velocity at position ③ is measured. Fw, forward; Bw, backward.

file [200], with the highest velocity occurring at the center of the vessels and gradually decreasing towards the vessel walls, as shown in Fig. 4.2(C,D,E). In the 3-D vascular model, when the blood flow velocity is low, it is usually in a state of laminar flow, and the Reynolds number $R_e = \frac{\rho_f |v_b| L}{\mu}$ ($O(10^{-1})$) is small at this time, where ρ_f is the density of the blood, v_b is the blood flow velocity, and μ is the viscosity of the blood, and L is the characteristic length. In the laminar flow state, the blood flow is relatively stable, the streamlines are arranged in an orderly manner, and there is no obvious disorder or turbulence [201]. In this case, the Reynolds number is small, the inertial effect of the blood is relatively small, and the viscous force plays a dominant role. However, when blood velocity increases, a transition may occur in the vascular model, from a laminar to a turbulent state of flow. In the turbulent state, the streamlines are chaotic and randomly arranged, and there are eddies and turbulent eddies. At this time, the Reynolds number becomes larger, and the inertial effect of the blood begins to be significant, playing a leading role in the flow. In actual human veins, the blood flow is usually in a state of laminar flow [202], due to the relatively

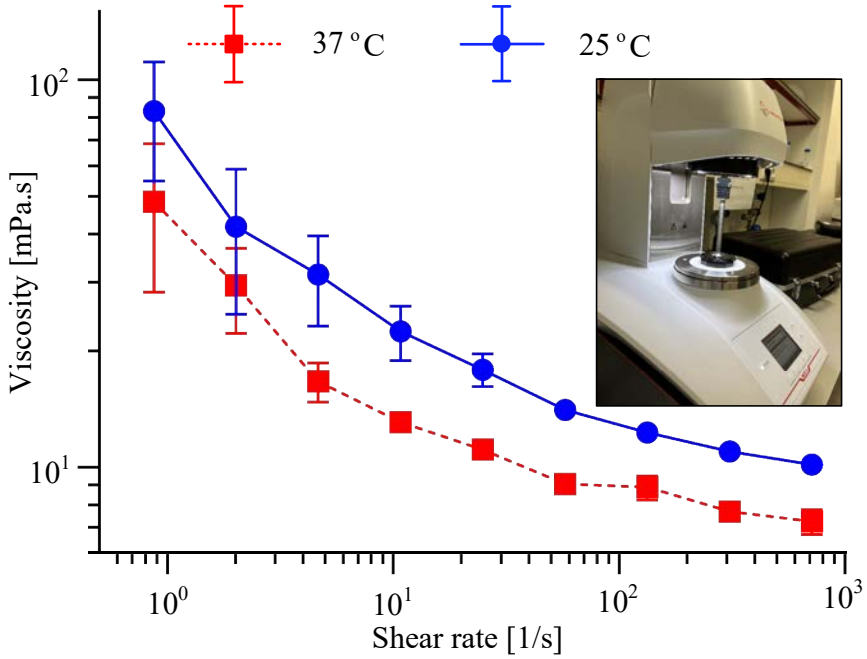

Figure 4.3: The mechanical properties of the blood are characterized using a rheometer. The viscosity of blood is measured at room temperature (25°C) and body temperature (37°C), respectively.

large diameter of the vein and the relatively slow speed of blood flow. It should be noted that venous blood flow may also be turbulent in certain situations, such as in narrowed veins or at the confluence of vascular branches or when disturbed by external pressure. This turbulent state can lead to non-uniform blood flow velocity, increased vortices and mixing phenomena, exerting additional pressure and shear forces on the vein wall.

In addition, the Reynolds number is inversely proportional to blood viscosity. When the blood viscosity increases, the Reynolds number decreases if other parameters remain constant. This is because higher viscosity increases the resistance of blood, causing a change in the balance of inertial and viscous forces during flow [203]. From Fig. 4.3, we can obtain that the blood viscosity decreases with the shear rate. Therefore, when the USHD swims through blood vessels at different rotational frequencies, it also changes the viscosity of the surrounding blood. Furthermore, variations in the velocity and viscosity of blood flow cause constant changes in resistance to the USHD, which can have implications for the USHD's stability, control, and navigation. Therefore a robust control method should be considered.

4.2.2 Ultrasound Volume Reconstruction of the 3-D Vascular Model

As shown in Fig. 4.4(A), this is a regular *in vitro* model of the 3-D vascular network which is fixed in a transparent container with a length, width, and height of 140 mm, 120 mm, and 50 mm. We define the width, length, and height of the container as the axis of the *in vitro* model coordinate system $\{x, y, z\}$. Additionally, the 3-D vascular model is a real-sized, silicone vascular model that replicates a particular neck anatomy, and target points 1 and 2 (Fig. 4.1(B)) are two angiomas. Before the motion control of the USHD inside the 3-D vascular model, the environment reconstruction of the 3-D vascular model is critical to plan the navigation path of the USHD. In the reconstruction process, the probe of the ultrasound system is automatically controlled to scan the 3-D vascular model along the y_0-axis in the global coordinate system, and equal interval ultrasound images are obtained. Further, these ultrasound images are processed to reconstruct the 3-D vascular model. A region of interest (ROI) is selected (Fig. 4.4(B)) so that the high region and the lower region with a strong reflection of

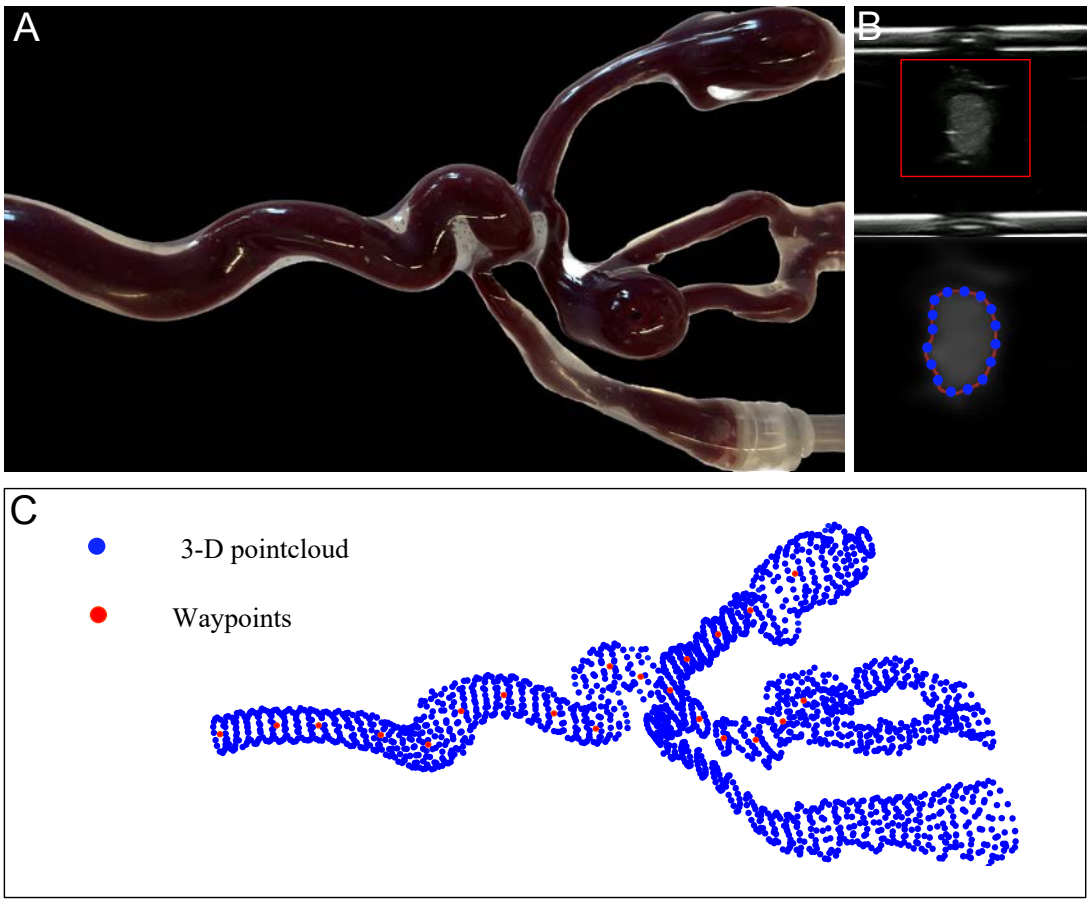

Figure 4.4: The environment reconstruction of the 3-D vascular model based on the ultrasound imaging system. (A) A 3-D vascular model is scanned by the ultrasound system. (B) The ultrasound B-mode obtains equal interval ultrasound images, and a region of interest (ROI) is extracted in the origin ultrasound image. The Gaussian blur is applied to the ultrasound image. After applying the Gaussian blur, the adaptive thresholding technique is used on the ROI. Following the adaptive thresholding step, edge extraction is performed on the ROI of the ultrasound image. (C) Based on the 2-D ultrasound images and the position of the ultrasound probe, the 3-D vascular model is reconstructed using the 3-D point cloud.

the ultrasound image are cropped. Then, the speckle noise is removed by using Gaussian blur, we binarize the gradient on the ultrasound image and extract the edges of the image, and then extract the corresponding points, as shown in Fig. 4.4(B). The 3-D point cloud can be obtained by combining

the position of the ultrasound probe and corresponding 2-D ultrasound images, and the waypoints are further extracted by image processing in each slice, as shown in Fig. 4.4(C). Therefore, the coordinates $\{\xi_v\}$ of the 3-D vascular model can be obtained as follows:

$$\xi_v = \begin{bmatrix} q_1 - x_o - l_p(p_c - p_x) \\ q_2 - y_o \\ h_p - l_p p_y \end{bmatrix}^T, \tag{4.1}$$

where q_1 and q_2 are the positions of ultrasound probe along the x_0-axis and y_0-axis directions. x_o and y_o are the position of the origin of the vascular model coordinate system in the x_0-axis and y_0-axis directions of the global coordinate system. p_x and p_y denote the coordinates of each point after extraction in the 2-D ultrasound image plane, and p_c represents the midpoint pixel coordinate in the horizontal direction of the 2-D ultrasound image plane. h_p represents the vertical distance from the ultrasound probe to the xy-plane. l_p represents the size of each pixel. This procedure is performed during the preoperative stage, and the generated path will serve as a reference for motion control of the USHD inside the 3-D vascular model.

For the objective assessment of ultrasound-based reconstruction of the 3-D vascular model, manually labeled ground-truth is used. In accordance with our methodology for the vascular model reconstruction, an analysis of cross-sectional 2-D ultrasound images of the vascular model leads to the computation of the Dice Coefficient, yielding a value of 0.905±0.037. Furthermore, the Euclidean distance between corresponding points within the two point clouds is determined to be 2.388±0.623 mm. Additionally, from the reconstructed 3-D vascular model, it is observed that path 1 exhibits a greater curvature compared to path 2. The maximum curvature along path 1 is measured at 19.6 mm^{-1}, while path 2 reaches a maximum curvature of 1.9 mm^{-1}. The degree of curvature of the vascular model will impact the control of the USHD during the closed-loop control experiments. Note that in the process of ultrasound guiding the USHD, the selection of the dynamic ROI of the 3-D vascular model is also based on the reconstructed vascular model.

4.3 Motion Control of the USHD

The PMR system of 6-DOF is used to guide a USHD inside the 3-D vascular model. Two DC motors are used to rotate the permanent magnets to generate the rotating magnetic field and the axis of the rotating magnetic field is controlled to guide the USHD inside the 3-D vascular model, as shown in Fig. 4.1(C).

4.3.1 System Description

In the PMR system, there are 6-DOF, three of which are utilized to adjust the position of the transducer (SonixTouch Q+, BK Medical, Quickborn, Germany). The motion of the ultrasound probe along the x_0-axis, the motion along the y_0-axis, and its own rotational motion are denoted as q_1, q_2, and q_3, respectively. The remaining 3-DOF are employed to control the pitch, motion along the y_0-axis of the rotating magnetic field, and yaw denoted as q_4, q_5, and q_6. These 6-DOF are controlled by six servo motors (MX-106R Dynamixel, Robotis, South Korea) respectively, as shown in Fig. 4.1(C). Two permanent magnets (NdFeB, R750F, Amazing Magnetic LLC, California, U.S.A) with diameter and height of 40 mm and 35 mm, are respectively installed on two DC motors (Maxon 47.022.022-0019-189 DC Motor Maxon Motors, Sachseln, Switzerland), which has a magnetization of 1.72 x 10^{-4} A.m^2, and the distance between the two permanent magnets is 35 cm. The field strength at the midpoint of the two magnets is approximately 5 mT. The orientation and location of the two DC motors are controlled independently using q_4, q_5, and q_6 to change the pitch and yaw angles of the USHD in different locations. The USHD (Fig. 4.1(C)) with length of 6 mm and diameter of 1.5 mm is fabricated through 3-D printing using polylactic acid filament (PrimaValue, 3-D Printers, The Netherlands). A cylindrical NdFeB magnet with diameter of 1.5 mm and length of 1.5 mm is attached to the USHD. In addition, a pulsation pump (HV-77910-55, Masterflex, Illinois, U.S.A) is used to provide blood flow at different flow rates into the anatomical vascular model (HN-S-A-006, Neck model, Elastrat, Switzerland). In our experiments, pig blood is used and a rheometer (MCR 92, Modular Compact Rheometer, Anton Paar, Austria) is used to measure the viscosity of the blood at room temperature and body temperature, respectively. The 3-D vascular model is covered by

Table 4.1: Specification of the untethered small-scale helical device (USHD) and a permanent-magnet robotic (PMR) system. d_t and l_t are the diameter and length of the USHD, respectively. $\mathbf{M}_{1,2}$ and $\mathbf{m}$ are magnetic dipole moments of two rotating permanent magnets and the USHD. ρ_f is the density of the blood, and R_e is Reynolds number. f_r is frequency of ultrasound waves, and Gn is gain of ultrasound system. TIS is the thermal index score, and MI is the mechanical index.

Parameter	Value	Parameter	Value
d_t [mm]	1.5	l_t [mm]	6
Pitch [mm]	1	Helicity [°]	71
$\mathbf{M}_{1,2}$ [A.m^2]	52.26	$\mathbf{m}$ [A.m^2]	6.23×10^{-4}
ρ_f [kg/m^3]	1050	R_e	O(10^{-1}) : O(10)
f_r [MHz]	14	Gn	42
TIS	0.21	MI	0.72

chicken breast tissue, and demineralized water is poured into the container so that there are no gaps between the 3-D vascular model and the tissues, as shown in Fig. 4.2(A). Specifications of the USHD and the PMR system are described in Table 4.1.

4.3.2 Control Strategy

We propose a point-to-point closed-loop control method that ensures the USHD reaches the predetermined target position under ultrasound imaging guidance. The navigation strategy consists of two key steps: the USHD recognition and the rotating magnetic field direction adjustment.

4.3.2.1 Identification and Tracking of the USHD

During the USHD movement, the ultrasound probe needs to be moved according to the position of the reconstructed 3-D vascular model and the po-

sition of the USHD. Therefore, before the closed-loop control of the USHD, we need to predefine the position of the ultrasound probe based on the reconstructed 3-D vascular model using q_1, q_2, and q_3.

$$\frac{q_1 - x_j}{q_2 - y_j} = \frac{q_1 - x_{j+1}}{q_2 - y_{j+1}}, \tag{4.2}$$

where $\mathbf{p}_j = (x_j,\ y_j,\ z_j)^T \in \Re^{n\times 3}$ is the waypoint of the 3-D vascular model in the global coordinate frame. Furthermore, q_3 can be defined using

$$q_3 = \tan^{-1}\left(\frac{x_{j+1} - x_j}{y_{j+1} - y_j}\right). \tag{4.3}$$

In order to ensure that the imaging of the vascular model is within the 2-D ultrasound plane, q_1 and q_2 need to be constrained using

$$\begin{cases} \sqrt{(q_1 - x_j)^2 + (q_2 - y_j)^2} \le \frac{l_u}{2} \\ \sqrt{(q_1 - x_{j+1})^2 + (q_2 - y_{j+1})^2} \le \frac{l_u}{2} \end{cases}, \tag{4.4}$$

where l_u is the width of the ultrasound image. Hence, q_1, q_2, and q_3 can be predefined before the closed-loop control experiment of the USHD. In order to achieve accurate control of the USHD, the recognition of the USHD in 2-D ultrasound images is crucial. Since the chicken breast tissue covers the 3-D vascular model in our experiment, it would bring noise to the ultrasound image. To reduce the effect of image noise, dynamic ROIs are selected based on the reconstructed model and the position of the ultrasound probe. Further, we binarize the ROI, the USHD is detected due to the different reflections of ultrasonic sound waves between the USHD and blood. Therefore, based on the position of the ultrasound probe and the position of the USHD in the ultrasound image, the position ($\mathbf{p}_g$) of the USHD in the global coordinate frame can be obtained using

$$\mathbf{p}_g = \begin{bmatrix} q_1 - (p_c - u)l_p \sin q_3 \\ q_2 - (p_c - u)l_p \cos q_3 \\ h_g - l_p v \end{bmatrix}, \tag{4.5}$$

where u and v represent the pixel coordinates of the USHD's position in the 2-D ultrasound image, and h_g represents the vertical distance from the ultrasound probe to the x_0y_0-plane.

4.3.2.2 Construction of an Ideal Rotating Magnetic Field

The two synchronously rotating permanent magnets are used to control the USHD in the 3-D vascular model, and the rotation axis of the permanent magnet is adjusted to construct the ideal rotating magnetic field. In the PMR system, each field is modeled according to the following point-dipole approximation [84], [85]:

$$\mathbf{B}_i(\mathbf{p}) = \frac{\mu_0}{4\pi|\mathbf{p}|^3}\left(\frac{3(\mathbf{M}_i \cdot \mathbf{p})\mathbf{p}}{|\mathbf{p}|^2} - \mathbf{M}_i\right) \qquad i = 1,\ 2, \tag{4.6}$$

where $\mathbf{B}_1$ and $\mathbf{B}_2$ respectively represent the magnetic field generated by two permanent magnets, μ_0 represents the penetration constant, and $\mathbf{p}$ is the position vector of the USHD with respect to the rotating permanent magnet, and $\mathbf{M}_i$ denotes the magnetic dipole moment of ith permanent magnet. We assume that enough torque is provided using the external rotating magnetic field, and the magnetization of the USHD ultimately aligns with the magnetic field lines. Consequently, the motion direction of the USHD can be changed using the direction of the external driving magnetic field at the position of the USHD.

According to the point-dipole approximation model (4.6) and the direction error of the USHD in the 3-D vascular model, the angles of the ideal rotating magnetic field can be obtained using

$$\angle\mathbf{B}_{\mathrm{p}}(\mathbf{p}) = \tan^{-1}\left(\frac{\sqrt{(\mathbf{p}_i - \mathbf{p})_x{}^2 + (\mathbf{p}_i - \mathbf{p})_y{}^2}}{(\mathbf{p}_i - \mathbf{p})_z}\right), \tag{4.7}$$

where $\angle\mathbf{B}_{\mathrm{p}}(\mathbf{p})$ represents the ideal angles of the rotating magnetic field in the pitch direction, $\mathbf{p}_i \in \Re^{n\times 3}$ is the waypoint of the 3-D vascular model. Furthermore, we can calculate the ideal angles of the rotating magnetic field in yaw direction using

$$\angle\mathbf{B}_{\mathrm{y}}(\mathbf{p}) = \tan^{-1}\left(\frac{(\mathbf{p}_i - \mathbf{p})_x}{(\mathbf{p}_i - \mathbf{p})_y}\right). \tag{4.8}$$

Therefore, we can obtain desired magnetic field $\mathbf{B}^{\mathrm{d}}(\mathbf{p})$ based on the angle ($\angle\mathbf{B}_{\mathrm{p}}(\mathbf{p})$ and $\angle\mathbf{B}_{\mathrm{y}}(\mathbf{p})$) of the desired magnetic field, and then calculate the desired magnetization $\mathbf{M}^{\mathrm{d}}$ using Equation (4.6) [188]. Then an ideal

Table 4.2: Pseudocode of the closed-loop control of the USHD inside the 3-D vascular model using the PMR system and ultrasound guidance.

Algorithm: Control algorithm for the USHD

Input:

waypoint group $\mathbf{p}_i \in \Re^{n\times 3}$;

position of the ultrasound probe $\mathbf{p}_b = (q_1,\ q_2,\ q_3)^T \in \Re^{j\times 3}$;

ROI of the 3-D vascular network model;

real-time 2D ultrasound images $\mathbf{U}_f \in \Re^{u\times v}$;

error thresholds ε;

Output:

position $\mathbf{p}$ of the USHD;

input of the PMR system (q_1-q_6);

angular frequency of the rotating magnetic field ω;

Initialization:

i:=1, b:=1, and $(q_1(0) - q_6(0))$;

while $i \leq n$ **do**

$|\mathbf{e}| = |\mathbf{p}_i - \mathbf{p}|$;

$\omega = k_{\mathrm{p}}|\mathbf{e}| + k_{\mathrm{i}} \int_0^t |\mathbf{e}|dt + k_{\mathrm{d}}|\dot{\mathbf{e}}|$;

if $|\mathbf{e}| < \varepsilon$;

$i \leftarrow i + 1$;

$b \leftarrow b + 1$;

$\angle\mathbf{B}_{\mathrm{p}}(\mathbf{p}) = \tan^{-1}\left(\frac{\sqrt{(\mathbf{p}_i-\mathbf{p})_x{}^2+(\mathbf{p}_i-\mathbf{p})_y{}^2}}{(\mathbf{p}_i-\mathbf{p})_z}\right)$;

$\angle\mathbf{B}_{\mathrm{y}}(\mathbf{p}) = \tan^{-1}\left(\frac{(\mathbf{p}_i-\mathbf{p})_x}{(\mathbf{p}_i-\mathbf{p})_y}\right)$;

$\mathbf{B}^{\mathrm{d}}(\mathbf{p}) \leftarrow \angle\mathbf{B}_{\mathrm{p}}(\mathbf{p})$ and $\angle\mathbf{B}_{\mathrm{y}}(\mathbf{p})$;

$\mathbf{M}^{\mathrm{d}} \leftarrow \mathbf{B}^{\mathrm{d}}(\mathbf{p})$;

$(q_4,\ q_5,\ q_6) \leftarrow \mathbf{M}^{\mathrm{d}}$;

end

end

rotating magnetic field can be constructed by changing joint space coordinates (q_4, q_5, q_6). In addition, a proportional-integral-derivative controller $\omega = k_\mathrm{p}|\mathbf{e}| + k_\mathrm{i}\int_0^t |\mathbf{e}|dt + k_\mathrm{d}|\dot{\mathbf{e}}|$ is used to control the rotation angular frequency of the magnetic field, where $|\mathbf{e}| = |\mathbf{p}_i - \mathbf{p}|$ is the position error, and k_p, k_i, and k_d all non-negative, denote the coefficients for the proportional, integral, and derivative terms respectively. Note that the selection of these coefficients depends on the velocity of the blood flow and the geometry of the 3-D vascular model. Further, the rotation frequency of the magnetic field is less than the step-out frequency. Finally, we implement an OpenCV (version 3.4.9) image processing library to detect and track the USHD in the ultrasound system frame. The control strategy is implemented in C++ on a computer running Linux Ubuntu 16.04. A pseudocode of the closed-loop control implementation is provided in Table 4.2.

4.3.3 Experimental Results

The USHD is controlled to swim toward the target point inside the 3-D vascular model under the proposed control strategy. During the closed-loop control experiments of the USHD, the ultrasound B-mode is applied to obtain ultrasound images at frame rate of 28 Hz, and the different blood flow rates are provided in the 3-D vascular model.

We first perform navigation experiments of the USHD inside the 3-D vascular model encased in chicken tissue. In path 1 (Fig. 4.1(B)) of the 3-D vascular model, the USHD swims from starting point toward target point 1, as shown in Figs. 4.5 and 4.6. During the motion control of the USHD in path 1, the joint space coordinate of the PMR system can be obtained ($n = 5$) under the proposed control method, when the blood flow rates are 0 mL/min, 16.6 mL/min, and 33.3 mL/min, as shown in Fig. 4.5. q_1, q_2, and q_3 are updated based on the reconstructed 3-D vascular model and the current position of the USHD, and q_4, q_5, and q_6 can be calculated based on the current position of the USHD and the position of the waypoints in path 1 under the proposed control strategy. For path 1, the angle of the rotating magnetic field and the position of the ultrasound probe can be changed using the joint space coordinate (q_1-q_6) of the PMR system, when the blood flow rate is 16.6 mL/min, as shown in Fig. 4.6(A). Furthermore, five ultrasound tracking instants are shown in Fig. 4.6(B), demonstrating that, although there is noise in the ultrasound image due to the wrapping of

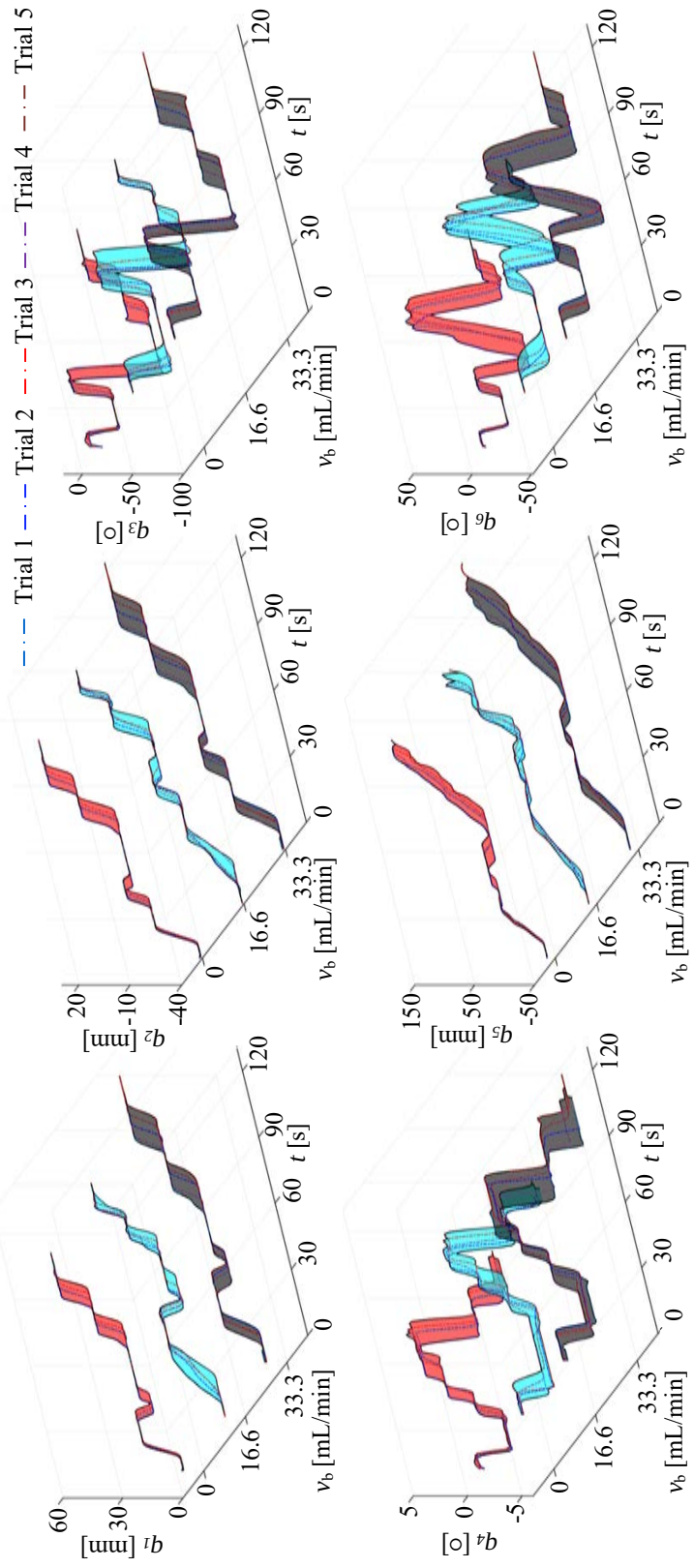

Figure 4.5: The control input of the PMR system for path 1 of the 3-D vascular model. Under blood flow rate (v_b) of 0 mL/min, 16.6 mL/min, and 33.3 mL/min, control input of the PMR system can be obtained using proposed control method when the USHD swims toward target point 1 (n=5).

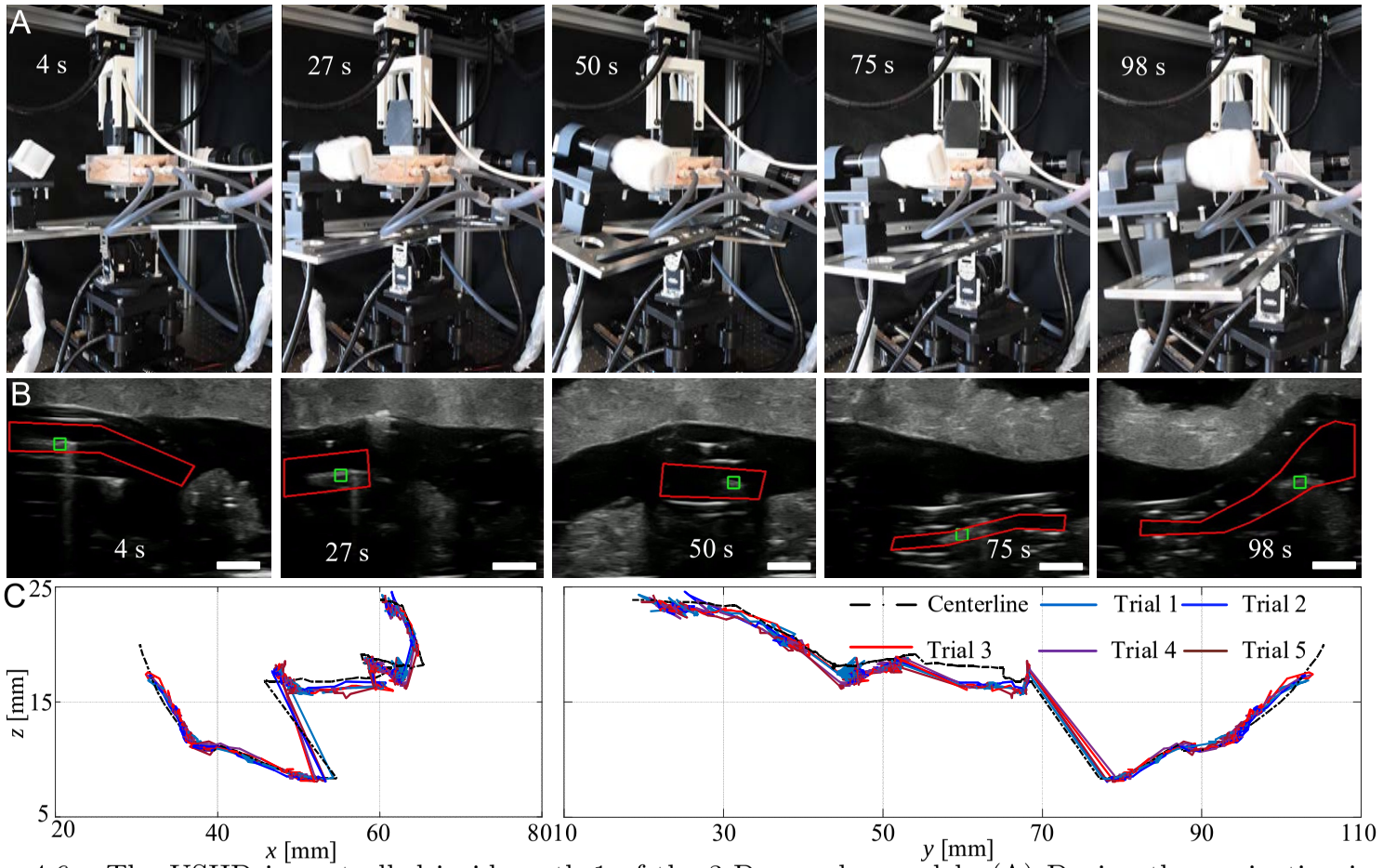

Figure 4.6: The USHD is controlled inside path 1 of the 3-D vascular model. (A) During the navigation in path 1, the PMR system is configured at five time instants when the blood flow rate is 16.6 mL/min. (B) For $v_b = 16.6$ mL/min, the 2-D ultrasound images are used to track the USHD in different positions during the closed-loop control experiments. (C) In path 1, the USHD swims toward target point 1 under ultrasound guidance when the blood flow rate is 16.6 mL/min (n=5). The scale bar is 5 mm. *Please refer to the supplementary video.*

chicken tissue and the vascular model wall, the USHD can be identified and tracked stably under our proposed method. Fig. 4.6(C) plots the USHD navigation results and shows the position of the USHD and centerline of path 1 of the 3-D vascular model ($n = 5$) when the flow rate of blood is 16.6 mL/min. *Please refer to the accompanying video.*

Similar to path 1, the USHD swims toward target point 2 along path 2 of the 3-D vascular model, as shown in Figs. 4.7 and 4.8. Fig. 4.7 demonstrates the control input obtained for path 2 ($n = 5$) when flow rates of 0 mL/min, 16.6 mL/min, and 33.3 mL/min are provided in the 3-D vascular model. Fig. 4.8(A) illustrates five instances of the PMR system configurations when the blood flow rate is 16.6 mL/min, while Fig. 4.8(B) displays the corresponding five instances of ultrasound tracking along path 2 at these instances. The motion trajectories of the USHD inside path 2 of the 3-D vascular model are extracted ($n = 5$), as shown in Fig. 4.8(C). By examining the control inputs (q_1-q_6) depicted in Fig. 4.5 and Fig. 4.7 for paths 1 and 2 respectively, we observe that the control inputs remain similar across the 5 trials, indicating the stable performance of the PMR system and the effectiveness of the proposed control method. *Please refer to the accompanying video.*

In order to further evaluate the stability performance of the PMR system, we continue to repeat closed-loop control experiments of the USHD at blood flow rates of 0 mL/min, 16.6 mL/min, and 33.3 mL/min respectively, where the blood flow rate of 33.3 mL/min corresponds to 56% of the maximum venous flow rate [131]. For each path and each blood flow rate, we perform 30 consecutive trials ($n = 30$). From experiments, we observed that when the flow rate is 0 mL/min, regardless of path 1 or path 2, the success rate of the USHD reaching the target point is extremely high under our proposed control method, as shown in Fig. 4.9(A). In this case, the success rate of path 1 is slightly lower than that of path 2 due to the higher curvature of path 1. However, when the blood flow rate increases, the success rate of the USHD for paths 1 and 2 to the target position decreases, because the pulsating blood flow (Fig. 4.2(C,D,E)) brings external disturbances in the motion control of the USHD. In the presence of blood flow, the success rate of path 2 is lower than that of path 1. This outcome can be attributed to the intersection of path 1 and path 2. Due to the influence of blood flow, the USHD might mistakenly enter path 1 instead of swimming towards the intended target point 2, and the USHD enters

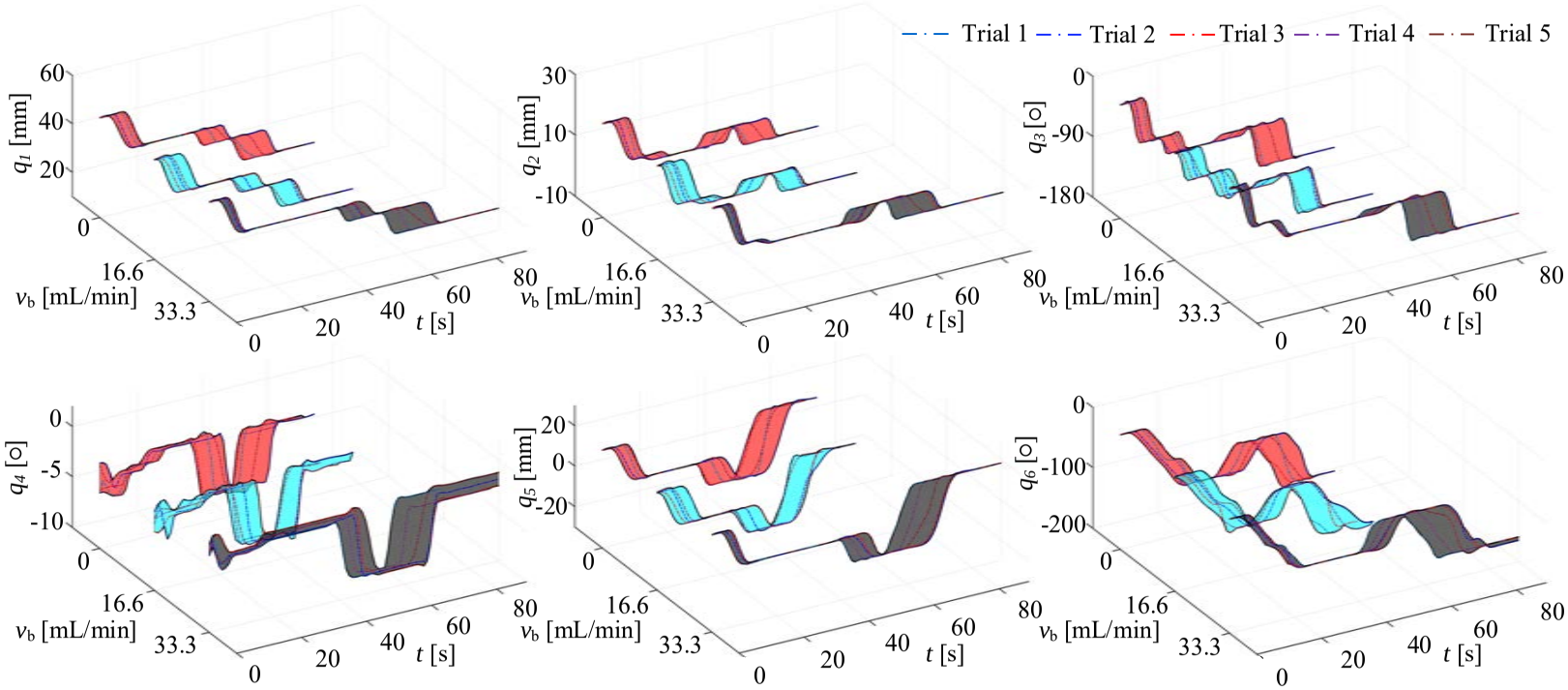

Figure 4.7: The control input of the PMR system for path 2 of the 3-D vascular model. Under blood flow rate (v_b) of 0 mL/min, 16.6 mL/min, and 33.3 mL/min, control input of the PMR system can be obtained using proposed control method when the USHD swims toward target point 2 (n=5).

Figure 4.8: The USHD is controlled inside path 2 of the 3-D vascular model. (A) During the navigation in path 2, the PMR system is configured at five time instants when the blood flow rate is 16.6 mL/min. (B) For $v_b = 16.6$ mL/min, the 2-D ultrasound images are used to track the USHD in different positions during the closed-loop control experiments. (C) In path 2, the USHD swims toward target point 2 under ultrasound guidance when the blood flow rate is 16.6 mL/min (n=5). The scale bar is 5 mm. *Please refer to the supplementary video.*

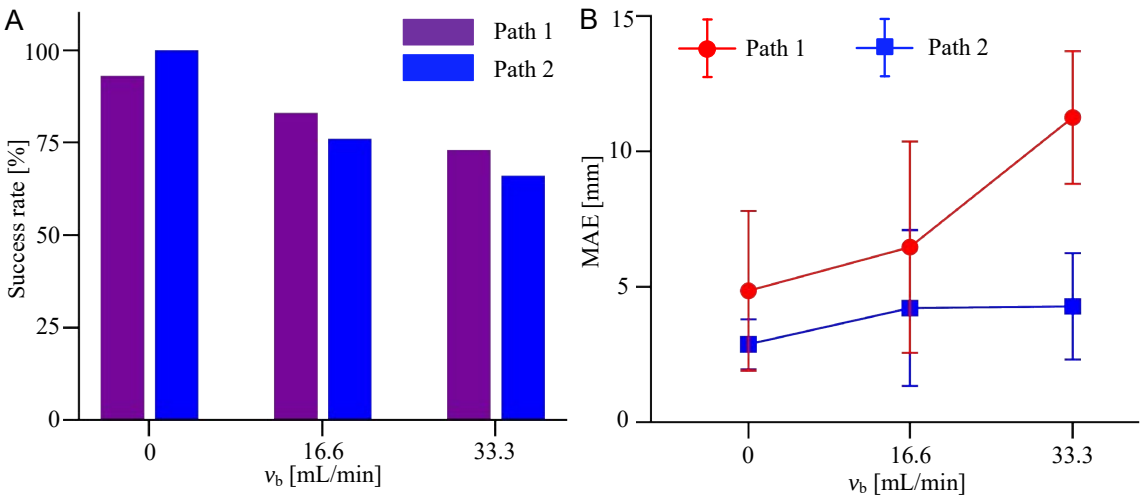

Figure 4.9: The USHD is controlled inside paths 1 and 2, when blood flow rates (v_b) are 0 mL/min, 16.6 mL/min, and 33.3 mL/min, respectively. (A) The success rate can be calculated from the 30 consecutive trials (n=30) for the different paths and different flow rates. (B) The mean absolute error can be calculated from successful trials under different paths and different flow rates.

the wrong vascular model branch and then loses the target, which leads to the failure of the USHD's navigation. From the experimental results, it can be seen that when the blood flow rate is 16.6 mL/min, the success rate of the PMR system controlling the USHD in the 3-D vascular model is higher than 75%. Further, in the experimental trials with successful navigation, we calculated that as the blood flow rate increases, the mean absolute error of the USHD reaching the target position increases under our proposed control method, as shown in Fig. 4.9(B). In addition, the target position in path 1 exhibits a steeper inclination compared to the target position in path 2, resulting in a greater mean absolute error of the USHD in path 1.

4.4 Discussion

In this paper, we investigate the motion control of a USHD driven by rotating magnetic fields inside a 3-D vascular model. The use of such USHDs holds great promise for minimally invasive procedures in the field of interventional medicine [131]. One of the major advantages of the helical body

is its ability to navigate through tortuous blood vessels. The helical shape allows the USHD to propel itself forward by utilizing the principle of helical motion. By controlling the rotation and translation of the USHD using rotating magnetic fields, precise and controlled movements can be achieved inside the 3-D vascular network. This capability facilitates the targeted delivery of therapeutic agents, such as drug-loaded nanoparticles, to specific regions. However, there are still many factors that must be considered if this technology is to be successfully transferred to the clinic. First, there is room for further improvement in the choice of materials for the USHD. The utilization of soft and biocompatible materials, such as hydrogels, can be advantageous in minimizing tissue impact and reducing potential toxicity associated with the USHD's presence. Second, it is imperative to assess the size of the USHD to prevent potential blockages, as the diameter of the blood vessel is variable and uncertain. Therefore, careful consideration should be given to the USHD's dimensions to ensure unobstructed passage through these narrow and delicate vessels, minimizing the risk of complications. Thirdly, the stability of the system and the robustness of the proposed control method are crucial for clinical operations. It can be seen from our experiments that when the flow rate increases, the success rate of the experiment decreases. Developing more advanced and smarter navigation and control mechanisms is crucial to ensure the USHD can effectively maneuver through the complex and dynamic vascular network. Integration of sensing technologies, imaging guidance, and advanced control algorithms may be necessary to enable accurate and real-time navigation. Lastly, in our current PMR system, the separation between the two permanent magnets measures 35 cm. We recognize that this operational space falls short of meeting the demands of real clinical applications. One potential enhancement is to increase the distance between the two permanent magnets, thereby obtaining a larger operational area. Additionally, we are exploring the utilization of permanent magnets with higher magnetic moments to further enhance system performance. These improvements are anticipated to provide our PMR system with a broader range of operation, better aligning with the demands of clinical applications.

During the navigation of the USHD, ultrasound imaging is widely used in conjunction with the USHD for real-time visualization and guidance [80], [163], [204]. It provides valuable information about the blood vessel anatomy, including vessel diameter, tortuosity, and potential obstacles.

Furthermore, the measurement of blood flow velocity using the ultrasound imaging system plays a crucial role in the context of the USHD's navigation inside blood vessels. The flow velocity of blood can significantly influence the motion of the USHD. By incorporating real-time blood flow velocity measurements, the USHD can adapt its navigation and motion control strategies accordingly. For instance, high blood flow velocity areas may require the USHD to adjust its speed and propulsion force by changing the frequency of the rotating magnetic field to ensure stable and precise movement. By integrating ultrasound-based flow velocity feedback into the control algorithm, the USHD can optimize its trajectory planning and motion control to effectively maneuver through varying flow conditions. This integration may enable the USHD to navigate more safely and efficiently, improving its overall performance and reducing the risk of potential complications during intravascular procedures. Additionally, in our experiments, the alignment between the USHD's trajectory and the reconstructed path is also influenced by the diameter of the vascular model. The maximum diameter of the vascular model we used is approximately 4 mm. In such cases, we ensure precise alignment between the ultrasound probe's position and the reconstructed path, which allows the ultrasound system to effectively detect and navigate the USHD. However, it's worth noting that our proposed approach might encounter challenges in larger blood vessels. The potential for losing control arises due to disparities between the USHD's movement trajectory and the reconstructed path inside these wider vessels.

In actual clinical surgeries, achieving successful navigation of USHD to the targeted pathological region inside blood vessels relies on the prerequisite of 3-D vascular reconstruction. In our experiments, the reconstruction error of the vascular model reaches the millimeter level, which is larger compared to previous state-of-the-art approaches [205]–[207] where errors are in the sub-millimeter range. The likely reason behind this is that our segmentation method is not sufficiently accurate. Additionally, our vascular model is flexible, and even minor displacements during the reconstruction process may introduce errors. Further, for real blood vessels in the body, the presence of other tissues and surrounding vessels may impact the accurate reconstruction of the target vessel. Therefore, the combination of advanced medical image segmentation methods [207]–[209] becomes crucial to improve the accuracy of the vascular reconstruction. Once the vascular reconstruction is ensured, ROIs pertaining to the vessel can be established,

consequently reducing the influence of noise from surrounding structures on tracking of the USHD.

Overall, our study demonstrates the potential of USHDs controlled by rotating magnetic fields for intravascular procedures. The combination of magnetic control, ultrasound imaging, and motion control strategies provides a promising platform for navigating and performing interventions inside blood vessels.

4.5 Conclusions and Future Work

This study demonstrates the successful control of a USHD inside a 3-D vascular model using a PMR system under ultrasound guidance. Before the closed-loop control of the USHD, the centerline of the 3-D vascular model is accurately determined based on 2-D ultrasound images and the position of the ultrasound probe, providing precise waypoints for the USHD. By employing ultrasound guidance, motion control of the USHD is achieved at various blood flow rates. The proposed method enables the determination of joint space coordinates of the PMR system. Analysis of these coordinates reveals that the USHD can be accurately guided to reach the target position within a certain range of control input. These results highlight the effectiveness and robustness of our system in navigating the USHD through a complex vascular network model.

As part of future studies, a biodegradable USHD will be considered, and then we will use this USHD to perform thrombus removal experiments and targeted drug delivery experiments inside the 3-D vascular model under ultrasound imaging guidance. Furthermore, sensor faults will be considered in the closed-loop control experiments of the USHD, and a fault-tolerant control method based on sensor faults will be studied. In addition, we also plan to combine ultrasound images to perform *ex vivo* experiments to verify our PMR system in a time-varying fluid flow rate environment.

5

Conclusions

This doctoral thesis primarily delves into the control and navigation of USHDs inside vascular models, spanning various dimensions of vascular complexity (from 1-D to 2-D and even 3-D models). This extensive exploration of motion control not only serves as a testament to the effectiveness of the PMR system but also provides critical insights into the maneuverability and adaptability of USHDs within different vascular scenarios. Additionally, an essential aspect of this research is the evaluation of how different flow rates impact the motion of USHDs inside vascular network models. The goal of this study is to identify real-world challenges that USHDs face in dynamic vascular environments, such as disturbances from varying flow rates. It also aims to address challenges posed by the complexity of vascular geometric structures. By grasping the influence of flow rates, this research offers valuable insights that enhance the motion performance and control precision of USHDs in endovascular procedures. This knowledge can also be used to develop strategies for enhancing system stability and navigation performance when dealing with fluctuations in flow dynamics. Furthermore, the thesis investigates the development of a closed-loop motion control system for USHDs. By integrating the PMR system and ultrasound imaging system, a magnetic actuation system with real-time feedback is established to guide the USHD inside vascular models. The analysis of closed-loop motion control adds a layer of precision and accuracy to the manipulation of USHDs, paving the way for controlled and targeted interventions. In summation, this doctoral thesis not only presents a promising cutting-edge approach to minimally inva-

sive surgery in the field of vascular diseases but also offers comprehensive insights into various critical aspects of the technology. From the initial design and modeling of USHDs to their precise localization and control inside vascular models, this research enriches our understanding of these essential components, providing a foundation for the development of minimally invasive surgery. This chapter summarizes the key findings derived from this research. Moreover, recommendations for enhancing the system's performance and potential avenues for future research are presented, indicating the path forward for continued innovation and improvement in minimally invasive surgical techniques for vascular diseases.

5.1 Helical Propulsion

Magnetically-actuated USHDs have been extensively researched for medical applications. Despite numerous studies conducted on USHDs, there is still a lack of comprehensive characterization regarding the motion of the USHD inside blood vessels and its relationship with blood flow rate, especially under the influence of a PMR system. Therefore, the question (**RQ. 1**) involving how the flow of a physiological fluid affects the motion of the USHD is addressed. In **Chapter 2**, a 1-D hydrodynamic model is proposed to describe the helical propulsion of an externally actuated USHD against blood serum. This model takes into account the dynamics of the USHD and the influence of the surrounding fluid flow. Notably, an open-loop equilibrium point is identified within the uniform field region between two synchronously rotating permanent magnets. This equilibrium point undergoes a quadratic shift in response to changes in the flow rate. Furthermore, for the evaluation of the motion performance of the USHD under different flow conditions, experiments are conducted using both open-loop and closed-loop control strategies based on the proposed model. Remarkably, experimental results demonstrate asymptotic convergence, indicating that the USHD can achieve stable and precise propulsion even when subjected to varying flow rates, with the maximum flow rate tested being 1200 mL/hr. The findings from this study provide valuable insights into the behavior and control of USHDs in a fluid environment. The correspondence relationship between theoretical predictions and experimental outcomes further validates the effectiveness of the proposed model. These results lay a solid foundation for future research aiming to assess and optimize the perfor-

mance of USHDs under realistic physiological flow conditions encountered in clinical settings. By leveraging the knowledge gained from this study, our system holds significant potential for clinical applications of the USHD. Further research can focus on refining the model, exploring advanced control strategies, and conducting *in vivo* experiments to validate the feasibility and efficacy of USHDs in real-life scenarios.

5.2 Real-Time Ultrasound Guidance

Following the study conducted in **Chapter 2**, the subsequent focus centers on the motion control of the USHD inside the vascular model, incorporating dynamic flow rates using the PMR system and ultrasound guidance. **Chapter 3** provides the corresponding answer to the question (**RQ. 2**) concerning how the penetration depth of the vascular model impacts the CNR of ultrasound images during the ultrasound guidance process. Furthermore, the impact of CNR on the closed-loop motion characteristics of the USHD is analyzed. In **Chapter 3**, frequency response analysis reveals that the locomotion speed of the USHD exhibits a linear relationship with the actuation frequency below the step-out frequency, regardless of the direction of fluid flow. Moreover, a point-to-point closed-loop motion control system for the USHD is developed by integrating the PMR system and an ultrasound imaging system. This control system enables the study of closed-loop control characteristics of the USHD within a physiological fluid environment. This closed-loop control system achieves asymptotic convergence of the USHD's position and velocity inside blood vessel phantoms. Experimental results demonstrate the effectiveness of ultrasound imaging in detecting and tracking the USHD inside blood vessel phantoms at various penetration depths, as well as in a blood vessel phantom with a bifurcation. In all closed-loop control experiments, the maximum position error of the USHD is recorded at 1.99 ± 0.55 mm, which is less than the length of the USHD's body. These findings showcase the potential of the integrated PMR system and ultrasound imaging system for precise closed-loop control of the USHD in physiological fluid environments. In addition, the ability to accurately detect and track the USHD's position using ultrasound imaging enhances the safety and efficacy of the control system.

In **Chapter 2** and **Chapter 3**, the vascular models employed were limited to 1-D or 2-D representations, which could not fully capture the

complex geometry of real blood vessels. Therefore, in **Chapter 4**, the corresponding research on developing a control method with robust performance for the USHDs operating inside a 3-D vascular model closely resembling the human body is presented. **Chapter 4** also addresses how to design a robust control system for navigating a USHD within a 3-D vascular model using the PMR system under ultrasound guidance (**RQ. 3**). In **Chapter 4**, this study demonstrates the successful control of a USHD inside a 3-D vascular model using a PMR system under ultrasound guidance. Before the closed-loop control of the USHD inside the 3-D vascular model, the reconstruction of the 3-D vascular model is determined based on 2-D ultrasound images and the position of the ultrasound probe. This process provides waypoints for guiding the USHD through the vascular network model. With the utilization of ultrasound guidance, motion control of the USHD is achieved in the 3-D vascular model across various blood flow rates. The proposed method enables the determination of joint space coordinates of the PMR system. Analysis of these coordinates reveals that the USHD can be accurately guided to reach the target position within a specific range of control input. This research highlights the effectiveness and robustness of the PMR system in navigating the USHD through a complex 3-D vascular network model. Therefore, the successful integration of the PMR system with ultrasound guidance offers a reliable and precise approach for controlling the motion of the USHD inside the 3-D vascular model. This advancement contributes to the development of minimally invasive surgical techniques and enhances our understanding of how such devices can navigate and manipulate within realistic physiological environments.

5.3 Future Work

So far, this doctoral voyage has outlined the motion control of the PMR system-driven USHD inside vascular models that push the state-of-the-art in small-scale robotics. Although there have been significant advances in motion control for USHDs, most of these studies have been limited to laboratory settings. To translate this technology into real clinical applications, several important factors need to be considered, including the fabrication process of the USHD, actuation system, real-time imaging system, and biocompatibility of the USHD. Based on the research results presented in this thesis, valuable suggestions can be made for each of these fields, and

new research questions can be raised for future investigations. Next, we will discuss future work in three parts: actuation system optimization, biodegradability and safety, and *ex vivo* and *in vivo* experiments.

5.3.1 Actuation System Optimization

In our study, a PMR system with 6-DOF was utilized to control the motion of the USHD inside vascular models. These degrees of freedom were primarily allocated for controlling the direction of the rotating magnetic field and adjusting the position of the ultrasound probe. Exploring the addition of more degrees of freedom is worth considering to further improve the flexibility and versatility of the magnetic system. By carefully analyzing and integrating these additional degrees, we can design an optimal configuration that enhances the magnetic system's flexibility. This enhancement can broaden the range of applications and significantly enhance the overall maneuverability of the USHD, making it adaptable to various scenarios and challenges.

In addition, we conducted USHD swimming experiments with relatively low flow velocities in the blood vessel model, which may not fully represent the maximum flow velocities encountered in human veins and arteries. To address the challenge of enabling the USHD to swim against resistance generated by high flow velocities, several strategies can be considered. First and foremost, increasing the magnetic field strength is crucial. This elevated magnetic field strength can increase the step-out frequency of the USHD [104], [210], [211]. Consequently, it increases the thrust of the USHD, enabling it to overcome the drag induced by high flow rates. This capability allows the USHD to maintain its desired position inside blood vessels. In addition, by concentrating the force acting on the USHD, the use of magnetic field gradient force may enable more effective control and maneuverability, ensuring that the device remains precisely where it is needed despite the challenging flow conditions.

Addressing these considerations will be instrumental in advancing the capabilities of the PMR system and USHDs in the context of high-flow velocity environments, such as arterial and venous vessels. These enhancements not only expand the potential applications of USHDs in vascular interventions but also contribute to the overall effectiveness and reliability of this innovative technology in clinical settings. Additionally, for future

clinical applications, the biodegradability and safety of USHDs inside blood vessels must also be taken into account.

5.3.2 Biodegradability and Safety

In **Chapter 2-4**, the fabrication of USHD involved the use of 3-D printing with polylactic acid filament. In our study, we did not explicitly consider the biodegradability of USHD or its potential safety implications for human health. These factors must be considered in future clinical surgery. First, it is important to investigate the use of biocompatible materials [93], [103], [212]–[214] for constructing the USHD in clinical surgery. The materials should be non-toxic, non-immunogenic, and have suitable mechanical properties to withstand the forces and environment inside blood vessels. Furthermore, we should explore materials that have the potential for biodegradation over time, ensuring the safe and gradual elimination of the USHD from the body. Secondly, it is important to consider the development of helical structures that are specifically designed to be biodegradable. Not only does this feature ensure optimal swimming performance for the USHD, but it also incorporates a safe degradation mechanism. This involves exploring materials and fabrication techniques that allow for controlled degradation of the USHD over a desired period. We further need to consider the impact of the degradation by-products on the surrounding tissues and evaluate their biocompatibility. Third, we also need to investigate the degradation rate and behavior of the USHD in the blood vessels. Determining the optimal degradation profile ensures the USHD's functionality for the intended duration while minimizing any potential adverse effects on the blood vessels or surrounding tissues. Moreover, we will conduct *in vitro* and *in vivo* studies to assess the degradation characteristics. Finally, we will perform comprehensive safety assessments to evaluate the potential risks associated with the USHD, and assess its cytotoxicity, immunogenicity, and potential for thrombogenicity or embolization. We also need to consider the long-term effects of the USHD on the blood vessels and overall vascular health, and then assess potential changes in vascular morphology, endothelial function, and blood flow dynamics over extended periods.

By addressing these future aspects, these endeavors have the potential to significantly contribute to the development of biodegradable and safe USHDs suitable for use inside blood vessels. Moreover, this research also

carries the promise of advancing minimally invasive interventions and targeted therapies within the cardiovascular system. This not only ensures the safety of patients but also holds the potential to optimize treatment outcomes, ultimately improving the quality of healthcare in the field of cardiovascular medicine.

5.3.3 *Ex Vivo* and *In Vivo* Experiments

The development and application of the USHD in both *ex vivo* and *in vivo* settings hold significance for future human surgical procedures. The way forward for USHDs is inseparable from the comprehensive exploration of *ex vivo* experiments. *Ex vivo* experiments [215]–[217], conducted in controlled laboratory settings, offer researchers a unique opportunity to closely examine how USHDs interact with biological samples such as tissues or organs, all outside the confines of a living organism. *Ex vivo* experiments encompass an in-depth assessment of USHD maneuverability, imaging capabilities, and therapeutic potential within precisely controlled environments. Researchers can meticulously analyze and characterize the performance of USHDs, including their capacity to navigate intricate anatomical structures and deliver targeted interventions with unprecedented precision.

When researching USHDs and magnetic navigation systems, conducting *in vivo* experiments is crucial to assess their feasibility in real human environments. However, existing *in vivo* experiments face several challenges, including differences between animal models and humans, high costs, and the technical difficulties of generating sufficiently strong magnetic fields. To successfully introduce these technologies into clinical applications, the following issues need to be addressed. First, *in vivo* experiments should be conducted at the same scale as clinical applications, taking into account the challenges of the operating room environment, patient physiology, and the surgical process. Secondly, magnetic actuation systems must meet the criteria for installation in the operating room and compatibility with other equipment [182]. Overcoming the above challenges will facilitate the adoption of magnetically-driven USHD as a viable clinical tool, providing more precise and less invasive treatment options to enhance patient health and recovery experiences.

The future of USHDs is marked by a journey from controlled *ex vivo* experiments to real-world *in vivo* studies. The implementation of *ex vivo*

and *in vivo* experiments of USHDs has the potential to reshape the landscape of medical technology and enhance our capacity to diagnose, treat, and minimally invasive interventional surgery. Collaboration between researchers, clinicians, and the healthcare industry is pivotal in harnessing the full potential of USHDs for the future of human clinical surgery and beyond. The impact of these innovative devices extends across multiple domains, promising a brighter future for healthcare.

5.4 Outlook

One of the most exciting aspects of USHDs is the ability to operate without the need for external connections or wires. This untethered nature empowers them with better mobility and flexibility within confined medical spaces. This feature is particularly valuable in minimally invasive surgeries, where the limited space inside blood vessels or other vascular structures can pose significant challenges.

USHDs have great potential for the diagnosis and monitoring of vascular diseases. They can be designed for real-time blood flow imaging, enabling healthcare professionals to assess the condition and functionality of blood vessels with unprecedented precision. This capability can aid in the early detection of issues such as thrombosis, aneurysms, and vessel malformations. USHDs can play a pivotal role in vascular reconstruction and interventional treatments. In cases of vascular stenosis or occlusion, these devices can be expertly navigated to the affected site. Once the USHD reaches the target position, they can perform localized procedures such as dilation or clearing obstructions, effectively restoring blood flow. This opens up possibilities for a range of interventional treatments, including angioplasty, stent implantation, endovascular surgery, and thrombolysis, all of which can be performed with precision and minimal invasiveness. The capacity to load medications onto USHDs and precisely administer them to specific areas inside blood vessels represents a significant breakthrough in the field of pharmacotherapy. This precise drug delivery approach minimizes systemic concentrations and associated side effects while maximizing the efficacy of treatment. USHDs can serve as "smart carriers" for therapeutic agents, navigating them to specific locations inside blood vessels, such as areas with inflammation or plaque buildup. USHDs can also contribute significantly to the assessment of vascular wall health. By combining

microscopic or imaging techniques, these devices can detect structural and functional abnormalities or lesions in vessel walls. Early detection of vascular wall damage, atherosclerosis, and other vascular diseases is crucial for initiating timely and appropriate treatment measures.

In summary, USHDs represent a groundbreaking technology with vast potential for the diagnosis, monitoring, and treatment of vascular diseases. Their unique capabilities, including precise navigation, drug delivery functionalities, and advanced vascular imaging, position them as invaluable tools for managing various vascular conditions. As research and innovation in this field continue to advance, USHDs are expected to play a pivotal role in improving the prevention, treatment, and management of vascular diseases, ultimately enhancing the quality of healthcare for patients worldwide. The ongoing evolution of these devices holds the promise of further transforming the landscape of vascular medicine.

Bibliography

[1] R. S. Vasan, "Biomarkers of cardiovascular disease: molecular basis and practical considerations," *Circulation*, vol. 113, no. 19, pp. 2335–2362, 2006.

[2] E. by: the European Stroke Organisation (ESO), A. F. Members, M. Tendera, V. Aboyans, M.-L. Bartelink, I. Baumgartner, D. Clément, J.-P. Collet, A. Cremonesi, M. De Carlo *et al.*, "Esc guidelines on the diagnosis and treatment of peripheral artery diseases: document covering atherosclerotic disease of extracranial carotid and vertebral, mesenteric, renal, upper and lower extremity arteries the task force on the diagnosis and treatment of peripheral artery diseases of the european society of cardiology (esc)," *European heart journal*, vol. 32, no. 22, pp. 2851–2906, 2011.

[3] G. D. Flora and M. K. Nayak, "A brief review of cardiovascular diseases, associated risk factors and current treatment regimes," *Current pharmaceutical design*, vol. 25, no. 38, pp. 4063–4084, 2019.

[4] A. Zenych, L. Fournier, and C. Chauvierre, "Nanomedicine progress in thrombolytic therapy," *Biomaterials*, vol. 258, p. 120297, 2020.

[5] R. T. Higashida, P. M. Meyers, C. C. Phatouros, J. J. Connors III, J. D. Barr, and D. Sacks, "Reporting standards for carotid artery angioplasty and stent placement," *Stroke*, vol. 35, no. 5, pp. e112–e134, 2004.

[6] L. M. S. Pádua, L. C. Garcia, C. J. Rubira, and P. E. de Oliveira Carvalho, "Stent placement versus surgery for coarctation of the thoracic aorta," *Cochrane database of systematic reviews*, no. 5, 2012.

[7] C. R. Narins and K. A. Illig, "Patient selection for carotid stenting versus endarterectomy: a systematic review," *Journal of vascular surgery*, vol. 44, no. 3, pp. 661–672, 2006.

[8] G. J. Rodriguez and A. I. Qureshi, "Current status of carotid artery angioplasty and stent placement: impact of recent clinical studies,"

Current neurology and neuroscience reports, vol. 8, no. 1, pp. 20–28, 2008.

[9] A. V. Singh, M. H. D. Ansari, M. Mahajan, S. Srivastava, S. Kashyap, P. Dwivedi, V. Pandit, and U. Katha, "Sperm cell driven microrobots—emerging opportunities and challenges for biologically inspired robotic design," *Micromachines*, vol. 11, no. 4, p. 448, 2020.

[10] L. Hines, K. Petersen, G. Z. Lum, and M. Sitti, "Soft actuators for small-scale robotics," *Advanced materials*, vol. 29, no. 13, p. 1603483, 2017.

[11] S. Pané, J. Puigmartí-Luis, C. Bergeles, X.-Z. Chen, E. Pellicer, J. Sort, V. Počepcová, A. Ferreira, and B. J. Nelson, "Imaging technologies for biomedical micro-and nanoswimmers," *Advanced Materials Technologies*, vol. 4, no. 4, p. 1800575, 2019.

[12] M. Koleoso, X. Feng, Y. Xue, Q. Li, T. Munshi, and X. Chen, "Micro/nanoscale magnetic robots for biomedical applications," *Materials Today Bio*, vol. 8, p. 100085, 2020.

[13] D. Li, C. Liu, Y. Yang, L. Wang, and Y. Shen, "Micro-rocket robot with all-optic actuating and tracking in blood," *Light: Science & Applications*, vol. 9, no. 1, p. 84, 2020.

[14] Q. Wang, X. Du, D. Jin, and L. Zhang, "Real-time ultrasound doppler tracking and autonomous navigation of a miniature helical robot for accelerating thrombolysis in dynamic blood flow," *ACS nano*, vol. 16, no. 1, pp. 604–616, 2022.

[15] Y. Chen, P. Kosmas, P. S. Anwar, and L. Huang, "A touch-communication framework for drug delivery based on a transient microbot system," *IEEE transactions on nanobioscience*, vol. 14, no. 4, pp. 397–408, 2015.

[16] T. Li, S. Yu, B. Sun, Y. Li, X. Wang, Y. Pan, C. Song, Y. Ren, Z. Zhang, K. T. Grattan *et al.*, "Bioinspired claw-engaged and biolubricated swimming microrobots creating active retention in blood vessels," *Science Advances*, vol. 9, no. 18, p. eadg4501, 2023.

[17] F. Qiu and B. J. Nelson, "Magnetic helical micro-and nanorobots: Toward their biomedical applications," *Engineering*, vol. 1, no. 1, pp. 021–026, 2015.

[18] W. R. DiLuzio, L. Turner, M. Mayer, P. Garstecki, D. B. Weibel, H. C. Berg, and G. M. Whitesides, "Escherichia coli swim on the right-hand side," *Nature*, vol. 435, no. 7046, pp. 1271–1274, 2005.

[19] X. Yan, Q. Zhou, M. Vincent, Y. Deng, J. Yu, J. Xu, T. Xu, T. Tang, L. Bian, Y.-X. J. Wang *et al.*, "Multifunctional biohybrid magnetite microrobots for imaging-guided therapy," *Science robotics*, vol. 2, no. 12, p. eaaq1155, 2017.

[20] C. Wang, V. R. Puranam, S. Misra, and V. K. Venkiteswaran, "A snake-inspired multi-segmented magnetic soft robot towards medical applications," *IEEE Robotics and automation letters*, vol. 7, no. 2, pp. 5795–5802, 2022.

[21] V. K. Venkiteswaran, D. K. Tan, and S. Misra, "Tandem actuation of legged locomotion and grasping manipulation in soft robots using magnetic fields," *Extreme Mechanics Letters*, vol. 41, p. 101023, 2020.

[22] V. Magdanz, I. S. Khalil, J. Simmchen, G. P. Furtado, S. Mohanty, J. Gebauer, H. Xu, A. Klingner, A. Aziz, M. Medina-Sánchez *et al.*, "Ironsperm: Sperm-templated soft magnetic microrobots," *Science advances*, vol. 6, no. 28, p. eaba5855, 2020.

[23] Z. Zheng, J. Han, S. O. Demir, H. Wang, W. Jiang, H. Liu, and M. Sitti, "Electrodeposited superhydrophilic-superhydrophobic composites for untethered multi-stimuli-responsive soft millirobots," *Advanced Science*, p. 2302409, 2023.

[24] R. Sanchis-Gual, H. Ye, T. Ueno, F. C. Landers, L. Hertle, S. Deng, A. Veciana, Y. Xia, C. Franco, H. Choi *et al.*, "3d printed template-assisted casting of biocompatible polyvinyl alcohol-based soft microswimmers with tunable stability," *Advanced Functional Materials*, p. 2212952, 2023.

[25] Y. Dong, L. Wang, Z. Zhang, F. Ji, T. K. Chan, H. Yang, C. P. Chan, Z. Yang, Z. Chen, W. T. Chang *et al.*, "Endoscope-assisted magnetic

helical micromachine delivery for biofilm eradication in tympanostomy tube," *Science Advances*, vol. 8, no. 40, p. eabq8573, 2022.

[26] W. Hu, G. Z. Lum, M. Mastrangeli, and M. Sitti, "Small-scale soft-bodied robot with multimodal locomotion," *Nature*, vol. 554, no. 7690, pp. 81–85, 2018.

[27] R. Yin, D. Wang, S. Zhao, Z. Lou, and G. Shen, "Wearable sensors-enabled human–machine interaction systems: from design to application," *Advanced Functional Materials*, vol. 31, no. 11, p. 2008936, 2021.

[28] R. K. Katzschmann, J. DelPreto, R. MacCurdy, and D. Rus, "Exploration of underwater life with an acoustically controlled soft robotic fish," *Science Robotics*, vol. 3, no. 16, p. eaar3449, 2018.

[29] T. Honda, K. Arai, and K. Ishiyama, "Micro swimming mechanisms propelled by external magnetic fields," *IEEE Transactions on Magnetics*, vol. 32, no. 5, pp. 5085–5087, 1996.

[30] D. J. Bell, S. Leutenegger, K. Hammar, L. X. Dong, and B. J. Nelson, "Flagella-like propulsion for microrobots using a nanocoil and a rotating electromagnetic field," in *Proceedings 2007 IEEE international conference on robotics and automation.* IEEE, 2007, pp. 1128–1133.

[31] A. K. Singh, R. Awasthi, and R. Malviya, "Bioinspired microrobots: Opportunities and challenges in targeted cancer therapy," *Journal of controlled release*, vol. 354, pp. 439–452, 2023.

[32] M. Suhail, A. Khan, M. A. Rahim, A. Naeem, M. Fahad, S. F. Badshah, A. Jabar, and A. K. Janakiraman, "Micro and nanorobot-based drug delivery: an overview," *Journal of Drug Targeting*, vol. 30, no. 4, pp. 349–358, 2022.

[33] D. Liu, T. Wang, and Y. Lu, "Untethered microrobots for active drug delivery: from rational design to clinical settings," *Advanced Healthcare Materials*, vol. 11, no. 3, p. 2102253, 2022.

[34] T. Honda, T. Sakashita, K. Narahashi, and J. Yamasaki, "Swimming properties of a bending-type magnetic micro-machine," *Journal-magnetics Society of Japan*, vol. 25, no. 4/2, pp. 1175–1178, 2001.

[35] S. Sudo, S. Segawa, and T. Honda, "Magnetic swimming mechanism in a viscous liquid," *Journal of intelligent material systems and structures*, vol. 17, no. 8-9, pp. 729–736, 2006.

[36] F. Z. Temel and S. Yesilyurt, "Magnetically actuated micro swimming of bio-inspired robots in mini channels," in *2011 IEEE International Conference on Mechatronics*. IEEE, 2011, pp. 342–347.

[37] H. Zhou, G. Alici, T. D. Than, W. Li, and S. Martel, "Magnetic propulsion of a spiral-type endoscopic microrobot in a real small intestine," in *2012 IEEE/ASME International Conference on Advanced Intelligent Mechatronics (AIM)*. IEEE, 2012, pp. 63–68.

[38] F. Z. Temel, A. E. Bezer, and S. Yesilyurt, "Navigation of mini swimmers in channel networks with magnetic fields," in *2013 IEEE International Conference on Robotics and Automation*. IEEE, 2013, pp. 5335–5340.

[39] M. A. Zeeshan, R. Grisch, E. Pellicer, K. M. Sivaraman, K. E. Peyer, J. Sort, B. Özkale, M. S. Sakar, B. J. Nelson, and S. Pané, "Hybrid helical magnetic microrobots obtained by 3d template-assisted electrodeposition," *Small*, vol. 10, no. 7, pp. 1284–1288, 2014.

[40] K. E. Peyer, E. Siringil, L. Zhang, and B. J. Nelson, "Magnetic polymer composite artificial bacterial flagella," *Bioinspiration & biomimetics*, vol. 9, no. 4, p. 046014, 2014.

[41] T. Xu, C.-I. Vong, B. Wang, L. Liu, X. Wu, and L. Zhang, "Rotating soft-tail millimeter-scaled swimmers with superhydrophilic or superhydrophobic surfaces," in *2016 6th IEEE International Conference on Biomedical Robotics and Biomechatronics (BioRob)*. IEEE, 2016, pp. 502–507.

[42] S. Jeon, J. Nam, W. Lee, and G. Jang, "Selective navigating and unclogging motions of an intravascular helical magnetic millirobot actuated by external biaxial rotating magnetic fields," *IEEE/ASME Transactions on Mechatronics*, vol. 22, no. 3, pp. 1456–1464, 2017.

[43] R. Venezian and I. S. Khalil, "Understanding robustness of magnetically driven helical propulsion in viscous fluids using sensitivity anal-

ysis," *Advanced Theory and Simulations*, vol. 5, no. 4, p. 2100519, 2022.

[44] T. Xu, G. Hwang, N. Andreff, and S. Régnier, "Modeling and swimming property characterizations of scaled-up helical microswimmers," *IEEE/ASME Transactions on Mechatronics*, vol. 19, no. 3, pp. 1069–1079, 2013.

[45] F. Z. Temel, A. G. Erman, and S. Yesilyurt, "Characterization and modeling of biomimetic untethered robots swimming in viscous fluids inside circular channels," *IEEE/ASME Transactions on Mechatronics*, vol. 19, no. 5, pp. 1562–1573, 2013.

[46] S. Tottori, L. Zhang, K. E. Peyer, and B. J. Nelson, "Assembly, disassembly, and anomalous propulsion of microscopic helices," *Nano letters*, vol. 13, no. 9, pp. 4263–4268, 2013.

[47] T. Xu, H. Yu, H. Zhang, C.-I. Vong, and L. Zhang, "Morphologies and swimming characteristics of rotating magnetic swimmers with soft tails at low reynolds numbers," in *2015 IEEE/RSJ International Conference on Intelligent Robots and Systems (IROS)*. IEEE, 2015, pp. 1385–1390.

[48] L. Li and S. E. Spagnolie, "Swimming and pumping by helical waves in viscous and viscoelastic fluids," *Physics of Fluids*, vol. 27, no. 2, p. 021902, 2015.

[49] T. Xu, G. Hwang, N. Andreff, and S. Régnier, "Influence of geometry on swimming performance of helical swimmers using doe," *Journal of Micro-Bio Robotics*, vol. 11, pp. 57–66, 2016.

[50] L. Wang, H. Xu, W. Zhai, B. Huang, and W. Rong, "Design and characterization of magnetically actuated helical swimmers at submillimeter-scale," *Journal of Bionic Engineering*, vol. 14, no. 1, pp. 26–33, 2017.

[51] H. Sayyaadi and S. Bahmanyar, "Development of a new mechanism to change velocity in a helical swimmer robot at low reynolds number," *Scientia Iranica*, vol. 25, no. 5, pp. 2616–2627, 2018.

[52] N. Giuliani, L. Heltai, and A. DeSimone, "Predicting and optimizing microswimmer performance from the hydrodynamics of its components: the relevance of interactions," *Soft robotics*, vol. 5, no. 4, pp. 410–424, 2018.

[53] E. E. Hunter, E. W. Brink, E. B. Steager, and V. Kumar, "3d micromolding of small-scale biological robots," in *2018 International Conference on Manipulation, Automation and Robotics at Small Scales (MARSS)*. IEEE, 2018, pp. 1–6.

[54] C. Ye, J. Liu, X. Wu, B. Wang, L. Zhang, Y. Zheng, and T. Xu, "Hydrophobicity influence on swimming performance of magnetically driven miniature helical swimmers," *Micromachines*, vol. 10, no. 3, p. 175, 2019.

[55] J. Miao, X. Li, B. Liang, J. Wang, and X. Xu, "Enhancing swimming performance by optimizing structure of helical swimmers," *Sensors*, vol. 21, no. 2, p. 494, 2021.

[56] X. Wang, C. Hu, S. Pané, and B. J. Nelson, "Dynamic modeling of magnetic helical microrobots," *IEEE Robotics and Automation Letters*, vol. 7, no. 2, pp. 1682–1688, 2021.

[57] T. Xu, J. Yu, C.-I. Vong, B. Wang, X. Wu, and L. Zhang, "Dynamic morphology and swimming properties of rotating miniature swimmers with soft tails," *IEEE/ASME Transactions on Mechatronics*, vol. 24, no. 3, pp. 924–934, 2019.

[58] A. W. Mahoney, J. C. Sarrazin, E. Bamberg, and J. J. Abbott, "Velocity control with gravity compensation for magnetic helical microswimmers," *Advanced Robotics*, vol. 25, no. 8, pp. 1007–1028, 2011.

[59] R. Johnson and C. Brokaw, "Flagellar hydrodynamics. a comparison between resistive-force theory and slender-body theory," *Biophysical journal*, vol. 25, no. 1, pp. 113–127, 1979.

[60] A. F. Tabak and S. Yesilyurt, "Improved kinematic models for two-link helical micro/nanoswimmers," *IEEE Transactions on Robotics*, vol. 30, no. 1, pp. 14–25, 2013.

[61] A. G. Erman and A. F. Tabak, "Resistive force theory based modeling and simulation of surface contact for swimming helical micro robots with channel flow," in *Proceedings of the IEEE/ASME International Conference on Advanced Intelligent Mechatronics*, 2014, pp. 390–395.

[62] Y. Zhang, N. Wang, C. Du, Y. Sun, and D. Wang, "Control theorem of a universal uniform-rotating magnetic vector for capsule robot in curved environment," *Science China Technological Sciences*, vol. 56, pp. 359–368, 2013.

[63] Q. Fu, S. Guo, Y. Yamauchi, H. Hirata, and H. Ishihara, "A novel hybrid microrobot using rotational magnetic field for medical applications," *Biomedical microdevices*, vol. 17, pp. 1–12, 2015.

[64] Q. Wang, L. Yang, and L. Zhang, "Micromanipulation using reconfigurable self-assembled magnetic droplets with needle guidance," *IEEE Transactions on Automation Science and Engineering*, vol. 19, no. 2, pp. 759–771, 2021.

[65] T. Xu, G. Hwang, N. Andreff, and S. Régnier, "Characterization of three-dimensional steering for helical swimmers," in *2014 IEEE International Conference on Robotics and Automation (ICRA)*, 2014, pp. 4686–4691.

[66] Y. Guan, T. Xu, J. Liu, and X. Wu, "Image-based visual servoing of helical microswimmers for arbitrary planar path following at low reynolds numbers," in *2017 IEEE/RSJ International Conference on Intelligent Robots and Systems (IROS)*, 2017, pp. 1883–1888.

[67] T. Xu, Y. Guan, J. Liu, and X. Wu, "Image-based visual servoing of helical microswimmers for planar path following," *IEEE Transactions on Automation Science and Engineering*, vol. 17, no. 1, pp. 325–333, 2020.

[68] J. Liu, T. Xu, S. X. Yang, and X. Wu, "Navigation and visual feedback control for magnetically driven helical miniature swimmers," *IEEE Transactions on Industrial Informatics*, vol. 16, no. 1, pp. 477–487, 2020.

[69] X. Wu, J. Liu, C. Huang, M. Su, and T. Xu, "3-d path following of helical microswimmers with an adaptive orientation compensation model," *IEEE Transactions on Automation Science and Engineering*, vol. 17, no. 2, pp. 823–832, 2020.

[70] J. Liu, X. Wu, C. Huang, L. Manamanchaiyaporn, W. Shang, X. Yan, and T. Xu, "3-d autonomous manipulation system of helical microswimmers with online compensation update," *IEEE Transactions on Automation Science and Engineering*, vol. 18, no. 3, pp. 1380–1391, 2021.

[71] J. Leclerc, B. Isichei, and A. T. Becker, "A magnetic manipulator cooled with liquid nitrogen," *IEEE Robotics and Automation Letters*, vol. 3, no. 4, pp. 4367–4374, 2018.

[72] Z. Yang, L. Yang, and L. Zhang, "Eye-in-hand 3d visual servoing of helical swimmers using parallel mobile coils," in *2020 IEEE International Conference on Robotics and Automation (ICRA)*. IEEE, 2020, pp. 9223–9229.

[73] X. Du, Q. Wang, D. Jin, P. W. Y. Chiu, C. P. Pang, K. K. L. Chong, and L. Zhang, "Real-time navigation of an untethered miniature robot using mobile ultrasound imaging and magnetic actuation systems," *IEEE Robotics and Automation Letters*, vol. 7, no. 3, pp. 7668–7675, 2022.

[74] H. Zhao, J. Leclerc, M. Feucht, O. Bailey, and A. T. Becker, "3d path-following using mrac on a millimeter-scale spiral-type magnetic robot," *IEEE Robotics and Automation Letters*, vol. 5, no. 2, pp. 1564–1571, 2020.

[75] J. Leclerc, H. Zhao, D. Bao, and A. T. Becker, "In vitro design investigation of a rotating helical magnetic swimmer for combined 3-d navigation and blood clot removal," *IEEE Transactions on Robotics*, vol. 36, no. 3, pp. 975–982, 2020.

[76] H. Zhao, Y. Lu, A. T. Becker, and J. Leclerc, "Data-driven control for a milli-scale spiral-type magnetic swimmer using mpc," in *2022 International Conference on Robotics and Automation (ICRA)*, 2022, pp. 9823–9830.

[77] J. Leclerc, H. Zhao, D. Z. Bao, A. T. Becker, M. Ghosn, and D. J. Shah, "Agile 3d-navigation of a helical magnetic swimmer," in *2020 IEEE International Conference on Robotics and Automation (ICRA)*, 2020, pp. 7638–7644.

[78] J. Leclerc, Y. Lu, A. T. Becker, M. Ghosn, and D. J. Shah, "Resonating magnetic manipulation for 3d path-following and blood clot removal using a rotating swimmer," in *2020 IEEE/RSJ International Conference on Intelligent Robots and Systems (IROS)*, 2020, pp. 3083–3090.

[79] Y. Lu, H. Zhao, A. T. Becker, and J. Leclerc, "Steering rotating magnetic swimmers in 2.5 dimensions using only 2d ultrasonography for position sensing," *IEEE Robotics and Automation Letters*, vol. 7, no. 2, pp. 3162–3169, 2022.

[80] L. Yang, M. Zhang, Z. Yang, H. Yang, and L. Zhang, "Mobile ultrasound tracking and magnetic control for long-distance endovascular navigation of untethered miniature robots against pulsatile flow," *Advanced Intelligent Systems*, vol. 4, no. 3, p. 2100144, 2022.

[81] M. Zhang, L. Yang, C. Zhang, Z. Yang, and L. Zhang, "A 5-d large-workspace magnetic localization and actuation system based on an eye-in-hand magnetic sensor array and mobile coils," *IEEE Transactions on Instrumentation and Measurement*, vol. 72, pp. 1–11, 2023.

[82] Zhang, Moqiu and Yang, Lidong and Zhang, Chong and Yang, Zhengxin and Zhang, Li, "Simultaneous actuation and localization of magnetic robots using mobile coils and eye-in-hand hall-effect sensors," in *2021 IEEE/RSJ International Conference on Intelligent Robots and Systems (IROS)*. IEEE, 2021, pp. 8515–8521.

[83] I. S. M. Khalil, A. Adel, D. Mahdy, M. M. Micheal, M. Mansour, N. Hamdi, and S. Misra, "Magnetic localization and control of helical robots for clearing superficial blood clots," *APL Bioengineering*, vol. 3, no. 2, p. 026104, 2019.

[84] T. W. Fountain, P. V. Kailat, and J. J. Abbott, "Wireless control of magnetic helical microrobots using a rotating-permanent-magnet

manipulator," in *Proceedings of the IEEE International Conference on Robotics and Automation (ICRA)*, 2010, pp. 576–581.

[85] A. W. Mahoney, D. L. Cowan, K. M. Miller, and J. J. Abbott, "Control of untethered magnetically actuated tools using a rotating permanent magnet in any position," in *2012 IEEE International Conference on Robotics and Automation*. IEEE, 2012, pp. 3375–3380.

[86] B. Chaluvadi, K. M. Stewart, A. J. Sperry, H. C. Fu, and J. J. Abbott, "Kinematic model of a magnetic-microrobot swarm in a rotating magnetic dipole field," *IEEE Robotics and Automation Letters*, vol. 5, no. 2, pp. 2419–2426, 2020.

[87] R. Avaneesh, R. Venezian, C.-S. Kim, J.-O. Park, S. Misra, and I. S. M. Khalil, "Open-loop magnetic actuation of helical robots using position-constrained rotating dipole field," in *2021 IEEE/RSJ International Conference on Intelligent Robots and Systems (IROS)*. IEEE, 2021, pp. 8545–8550.

[88] L. J. W. Ligtenberg and I. S. M. Khalil, "Input-output boundedness of a magnetically-actuated helical device," in *2023 IEEE International Conference on Robotics and Automation (ICRA 2023)*. IEEE, 2023, pp. 5433–5438.

[89] A. Hosney, A. Klingner, S. Misra, and I. S. M. Khalil, "Propulsion and steering of helical magnetic microrobots using two synchronized rotating dipole fields in three-dimensional space," in *2015 IEEE/RSJ International Conference on Intelligent Robots and Systems (IROS)*, 2015, pp. 1988–1993.

[90] M. E. Alshafeei, A. Hosney, A. Klingner, S. Misra, and I. S. M. Khalil, "Magnetic-based motion control of a helical robot using two synchronized rotating dipole fields," in *5th IEEE RAS/EMBS International Conference on Biomedical Robotics and Biomechatronics*, 2014, pp. 151–156.

[91] A. Klingner, D. Mahdy, M. Hanafi, B. Adel, S. Misra, and I. S. M. Khalil, "Helical propulsion in a viscous heterogeneous medium," in *2020 International Conference on Manipulation, Automation and Robotics at Small Scales (MARSS)*, 2020, pp. 1–6.

[92] A. Vikram Singh and M. Sitti, "Targeted drug delivery and imaging using mobile milli/microrobots: A promising future towards theranostic pharmaceutical design," *Current pharmaceutical design*, vol. 22, no. 11, pp. 1418–1428, 2016.

[93] B. Wang, K. Kostarelos, B. J. Nelson, and L. Zhang, "Trends in micro-/nanorobotics: materials development, actuation, localization, and system integration for biomedical applications," *Advanced Materials*, vol. 33, no. 4, p. 2002047, 2021.

[94] L. Wang, Z. Meng, Y. Chen, and Y. Zheng, "Engineering magnetic micro/nanorobots for versatile biomedical applications," *Advanced Intelligent Systems*, vol. 3, no. 7, p. 2000267, 2021.

[95] M. Shojaeian, H. O. Caldag, A. Bozkurt, and S. Yesilyurt, "Fabrication of magnetic helical microribbons made of nickel thin films sandwiched between silicon nitride layers for microswimming applications," *Nanotechnology*, vol. 34, no. 1, p. 015301, 2022.

[96] H. Lee and S. Park, "Magnetically actuated helical microrobot with magnetic nanoparticle retrieval and sequential dual-drug release abilities," *ACS Applied Materials & Interfaces*, 2023.

[97] Y. Dong, L. Wang, V. Iacovacci, X. Wang, L. Zhang, and B. J. Nelson, "Magnetic helical micro-/nanomachines: Recent progress and perspective," *Matter*, vol. 5, no. 1, pp. 77–109, 2022.

[98] A. V. Singh, M. H. D. Ansari, P. Laux, and A. Luch, "Micro-nanorobots: important considerations when developing novel drug delivery platforms," *Expert opinion on drug delivery*, vol. 16, no. 11, pp. 1259–1275, 2019.

[99] F. Qiu, S. Fujita, R. Mhanna, L. Zhang, B. R. Simona, and B. J. Nelson, "Magnetic helical microswimmers functionalized with lipoplexes for targeted gene delivery," *Advanced Functional Materials*, vol. 25, no. 11, pp. 1666–1671, 2015.

[100] X. Wang, X.-Z. Chen, C. C. Alcântara, S. Sevim, M. Hoop, A. Terzopoulou, C. De Marco, C. Hu, A. J. de Mello, P. Falcaro *et al.*, "Mofbots: metal–organic-framework-based biomedical microrobots," *Advanced Materials*, vol. 31, no. 27, p. 1901592, 2019.

[101] K. T. Nguyen, S. Zheng, C.-S. Kim, B. Kang, D. Bang, J.-O. Park, E. Choi *et al.*, "A magnetically-controlled 3d-printed helical microrobot for application in photothermal treatment of cancer cells," in *2022 9th IEEE RAS/EMBS International Conference for Biomedical Robotics and Biomechatronics (BioRob)*. IEEE, 2022, pp. 1–5.

[102] Y. Sun, R. Pan, Y. Chen, Y. Wang, L. Sun, N. Wang, X. Ma, and G. P. Wang, "Efficient preparation of a magnetic helical carbon nanomotor for targeted anticancer drug delivery," *ACS Nanoscience Au*, 2022.

[103] Y. Liu, Y. Yang, X. Yang, L. Yang, Y. Shen, and W. Shang, "Multifunctionalized micro-helical capsule robots with superior loading and releasing capabilities," *Journal of Materials Chemistry B*, vol. 9, no. 5, pp. 1441–1451, 2021.

[104] J. Nam, W. Lee, J. Kim, and G. Jang, "Magnetic helical robot for targeted drug-delivery in tubular environments," *IEEE/ASME Transactions on Mechatronics*, vol. 22, no. 6, pp. 2461–2468, 2017.

[105] L. Zheng, S. Guo, and M. Kawanishi, "Magnetically controlled multifunctional capsule robot for dual-drug delivery," *IEEE Systems Journal*, vol. 16, no. 4, pp. 6413–6424, 2022.

[106] Y. Dong, L. Wang, J. Wang, S. Wang, Y. Wang, D. Jin, P. Chen, W. Du, L. Zhang, and B.-F. Liu, "Graphene-based helical micromotors constructed by "microscale liquid rope-coil effect" with microfluidics," *ACS nano*, vol. 14, no. 12, pp. 16 600–16 613, 2020.

[107] H. Ceylan, I. C. Yasa, O. Yasa, A. F. Tabak, J. Giltinan, and M. Sitti, "3d-printed biodegradable microswimmer for theranostic cargo delivery and release," *ACS nano*, vol. 13, no. 3, pp. 3353–3362, 2019.

[108] L. Xie, X. Pang, X. Yan, Q. Dai, H. Lin, J. Ye, Y. Cheng, Q. Zhao, X. Ma, X. Zhang *et al.*, "Photoacoustic imaging-trackable magnetic microswimmers for pathogenic bacterial infection treatment," *ACS nano*, vol. 14, no. 3, pp. 2880–2893, 2020.

[109] V. M. Kadiri, C. Bussi, A. W. Holle, K. Son, H. Kwon, G. Schütz, M. G. Gutierrez, and P. Fischer, "Biocompatible magnetic micro-and

nanodevices: fabrication of fept nanopropellers and cell transfection," *Advanced Materials*, vol. 32, no. 25, p. 2001114, 2020.

[110] L. Liu, B. Chen, K. Liu, J. Gao, Y. Ye, Z. Wang, N. Qin, D. A. Wilson, Y. Tu, and F. Peng, "Wireless manipulation of magnetic/piezoelectric micromotors for precise neural stem-like cell stimulation," *Advanced Functional Materials*, vol. 30, no. 11, p. 1910108, 2020.

[111] W. Zhuge, X. Ding, W. Zhang, D. Zhang, H. Wang, and J. Wang, "Microfluidic generation of helical micromotors for muscle tissue engineering," *Chemical Engineering Journal*, vol. 447, p. 137455, 2022.

[112] H. Zhang, B. Xu, Y. Ouyang, Y. Wang, H. Zhu, G. Huang, J. Cui, and Y. Mei, "Shape memory alloy helical microrobots with transformable capability towards vascular occlusion treatment," *Research*, vol. 2022, 2022.

[113] J. Leclerc, H. Zhao, D. Bao, and A. T. Becker, "In vitro design investigation of a rotating helical magnetic swimmer for combined 3-d navigation and blood clot removal," *IEEE Transactions on Robotics*, vol. 36, no. 3, pp. 975–982, 2020.

[114] I. S. Khalil, A. F. Tabak, K. Sadek, D. Mahdy, N. Hamdi, and M. Sitti, "Rubbing against blood clots using helical robots: Modeling and in vitro experimental validation," *IEEE Robotics and Automation Letters*, vol. 2, no. 2, pp. 927–934, 2017.

[115] K. T. Nguyen, S.-J. Kim, H.-K. Min, M. C. Hoang, G. Go, B. Kang, J. Kim, E. Choi, A. Hong, J.-O. Park *et al.*, "Guide-wired helical microrobot for percutaneous revascularization in chronic total occlusion in-vivo validation," *IEEE Transactions on Biomedical Engineering*, vol. 68, no. 8, pp. 2490–2498, 2020.

[116] J. Leclerc, Y. Lu, A. T. Becker, M. Ghosn, and D. J. Shah, "Resonating magnetic manipulation for 3d path-following and blood clot removal using a rotating swimmer," in *2020 IEEE/RSJ International Conference on Intelligent Robots and Systems (IROS)*. IEEE, 2020, pp. 3083–3090.

[117] L. Yang, M. Zhang, H. Yang, Z. Yang, and L. Zhang, "Hybrid magnetic force and torque actuation of miniature helical robots using mobile coils to accelerate blood clot removal," in *2021 IEEE/RSJ International Conference on Intelligent Robots and Systems (IROS)*. IEEE, 2021, pp. 7476–7482.

[118] I. S. Khalil, D. Mahdy, A. El Sharkawy, R. R. Moustafa, A. F. Tabak, M. E. Mitwally, S. Hesham, N. Hamdi, A. Klingner, A. Mohamed *et al.*, "Mechanical rubbing of blood clots using helical robots under ultrasound guidance," *IEEE Robotics and Automation Letters*, vol. 3, no. 2, pp. 1112–1119, 2018.

[119] Z. Yang, L. Yang, M. Zhang, C. Zhang, S. C. H. Yu, and L. Zhang, "Ultrasound-guided catheterization using a driller-tipped guidewire with combined magnetic navigation and drilling motion," *IEEE/ASME Transactions on Mechatronics*, vol. 27, no. 5, pp. 2829–2840, 2021.

[120] D. Mahdy, N. Hamdi, S. Hesham, A. El Sharkawy, and I. S. M. Khalil, "The influence of mechanical rubbing on the dissolution of blood clots," in *2018 40th Annual International Conference of the IEEE Engineering in Medicine and Biology Society (EMBC)*. IEEE, 2018, pp. 1660–1663.

[121] S. M. Jeon, G. H. Jang, and W. S. Lee, "Drug-enhanced unclogging motions of a double helical magnetic micromachine for occlusive vascular diseases," *IEEE Transactions on Magnetics*, vol. 50, no. 11, pp. 1–4, 2014.

[122] W. Lee, S. Jeon, J. Nam, and G. Jang, "Dual-body magnetic helical robot for drilling and cargo delivery in human blood vessels," *Journal of Applied Physics*, vol. 117, no. 17, p. 17B314, 2015.

[123] A. Hosney, J. Abdalla, I. S. Amin, N. Hamdi, and I. S. M. Khalil, "In vitro validation of clearing clogged vessels using microrobots," in *2016 6th IEEE International Conference on Biomedical Robotics and Biomechatronics (BioRob)*. IEEE, 2016, pp. 272–277.

[124] J. Kwon, J. Sa, D. Lee, and G. Jang, "Enhanced tunneling performance of magnetic helical robots utilizing pecking motion generated

by alternating rotating magnetic field," *IEEE Transactions on Magnetics*, pp. 1–1, 2023.

[125] F. Z. Temel, A. G. Erman, and S. Yesilyurt, "Characterization and modeling of biomimetic untethered robots swimming in viscous fluids inside circular channels," *IEEE/ASME Transactions on Mechatronics*, vol. 19, no. 5, pp. 1562–1573, 2014.

[126] S. Martel, "Microrobotics in the vascular network: present status and next challenges," *Journal of micro-nano mechatronics*, 2013.

[127] J. Zhang, "Evolving from laboratory toys towards life-savers: Small-scale magnetic robotic systems with medical imaging modalities," *Micromachines*, vol. 12, no. 11, p. 1310, 2021.

[128] B. Wang, Y. Zhang, and L. Zhang, "Recent progress on micro-and nano-robots: Towards in vivo tracking and localization," *Quantitative imaging in medicine and surgery*, vol. 8, no. 5, p. 461, 2018.

[129] Q. Wang and L. Zhang, "Ultrasound imaging and tracking of micro/nanorobots: From individual to collectives," *IEEE Open Journal of Nanotechnology*, vol. 1, pp. 6–17, 2020.

[130] G. C. Kagadis, K. Katsanos, D. Karnabatidis, G. Loudos, G. C. Nikiforidis, and W. R. Hendee, "Emerging technologies for image guidance and device navigation in interventional radiology," *Medical physics*, vol. 39, no. 9, pp. 5768–5781, 2012.

[131] B. J. Nelson, I. K. Kaliakatsos, and J. J. Abbott, "Microrobots for minimally invasive medicine," *Annual Review of Biomedical Engineering*, vol. 12, pp. 55–85, 2010.

[132] M. Sitti, H. Ceylan, W. Hu, J. Giltinan, M. Turan, S. Yim, and E. Diller, "Biomedical applications of untethered mobile milli/microrobots," *Proceedings of the IEEE*, vol. 103, no. 2, pp. 205–224, 2015.

[133] A. Ghosh and P. Fischer, "Controlled propulsion of artificial magnetic nanostructured propellers," *Nano Letters*, vol. 9, no. 6, pp. 2243–2245, 2009.

[134] L. Zhang, T. Petit, Y. Lu, B. E. Kratochvil, K. E. Peyer, R. Pei, J. Lou, and B. J. Nelson, "Controlled propulsion and cargo transport of rotating nickel nanowires near a patterned solid surface," *ACS Nano*, vol. 4, no. 10, pp. 6228–6234, 2010.

[135] S. Tottori, L. Zhang, F. Qiu, K. K. Krawczyk, A. Franco-Obregón, and B. J. Nelson, "Magnetic helical micromachines: fabrication, controlled swimming, and cargo transport," *Advanced Materials*, vol. 24, no. 6, pp. 811–816, 2012.

[136] A. Servant, F. Qiu, M. Mazza, K. Kostarelos, and B. J. Nelson, "Controlled in vivo swimming of a swarm of bacteria-like microrobotic flagella," *Advanced Materials*, vol. 27, no. 19, pp. 2981–2988, 2015.

[137] L. Arcese, M. Fruchard, and A. Ferreira, "Endovascular magnetically guided robots: navigation modeling and optimization," *IEEE Transactions on Biomedical Engineering*, vol. 59, no. 4, pp. 977–987, 2011.

[138] J.-B. Mathieu, G. Beaudoin, and S. Martel, "Method of propulsion of a ferromagnetic core in the cardiovascular system through magnetic gradients generated by an mri system," *IEEE Transactions on Biomedical Engineering*, vol. 53, no. 2, pp. 292–299, 2006.

[139] S. Martel, M. Mohammadi, O. Felfoul, Z. Lu, and P. Pouponneau, "Flagellated magnetotactic bacteria as controlled mri-trackable propulsion and steering systems for medical nanorobots operating in the human microvasculature," *The International Journal of Robotics Research*, vol. 28, no. 4, pp. 571–582, 2009.

[140] A. W. Mahoney and J. J. Abbott, "Managing magnetic force applied to a magnetic device by a rotating dipole field," *Applied Physics Letters*, vol. 99, no. 13, p. 134103, 2011.

[141] M. P. Kummer, J. J. Abbott, B. E. Kratochvil, R. Borer, A. Sengul, and B. J. Nelson, "Octomag: An electromagnetic system for 5-dof wireless micromanipulation," *IEEE Transactions on Robotics*, vol. 26, no. 6, pp. 1006–1017, 2010.

[142] A. W. Mahoney and J. J. Abbott, "Generating rotating magnetic fields with a single permanent magnet for propulsion of unteth-

ered magnetic devices in a lumen," *IEEE Transactions on Robotics*, vol. 30, no. 2, pp. 411–420, 2013.

[143] E. E. Niedert, C. Bi, G. Adam, E. Lambert, L. Solorio, C. J. Goergen, and D. J. Cappelleri, "A tumbling magnetic microrobot system for biomedical applications," *Micromachines*, vol. 11, no. 9, p. 861, 2020.

[144] A. Mahalingam, U. U. Gawandalkar, G. Kini, A. Buradi, T. Araki, N. Ikeda, A. Nicolaides, J. R. Laird, L. Saba, and J. S. Suri, "Numerical analysis of the effect of turbulence transition on the hemodynamic parameters in human coronary arteries," *Cardiovascular Diagnosis and Therapy*, vol. 6, no. 3, p. 208, 2016.

[145] A. Hosney, A. Klingner, S. Misra, and I. S. M. Khalil, "Propulsion and steering of helical magnetic microrobots using two synchronized rotating dipole fields in three-dimensional space," in *Proceedings of the IEEE/RSJ International Conference on Intelligent Robots and Systems (IROS)*, 2015, pp. 1988–1993.

[146] L. Arcese, A. Cherry, M. Fruchard, and A. Ferreira, "Dynamic behavior investigation for trajectory control of a microrobot in blood vessels," in *Proceedings of the IEEE/RSJ International Conference on Intelligent Robots and Systems (IROS)*, 2010, pp. 5774–5779.

[147] G. Dogangil, O. Ergeneman, J. J. Abbott, S. Pané, H. Hall, S. Muntwyler, and B. J. Nelson, "Toward targeted retinal drug delivery with wireless magnetic microrobots," in *Proceedings of the IEEE/RSJ International Conference on Intelligent Robots and Systems (IROS)*, 2008, pp. 1921–1926.

[148] A. T. Becker, S. P. Fekete, L. Huang, P. Keldenich, L. Kleist, D. Krupke, C. Rieck, and A. Schmidt, "Targeted drug delivery: algorithmic methods for collecting a swarm of particles with uniform, external forces," in *Proceedings of the IEEE International Conference on Robotics and Automation (ICRA)*, 2020, pp. 2508–2514.

[149] M. B. Akolpoglu, N. O. Dogan, U. Bozuyuk, H. Ceylan, S. Kizilel, and M. Sitti, "High-yield production of biohybrid microalgae for on-demand cargo delivery," *Advanced Science*, vol. 7, no. 16, p. 2001256, 2020.

[150] L. Yang, Y. Zhang, Q. Wang, and L. Zhang, "An automated microrobotic platform for rapid detection of c. diff toxins," *IEEE Transactions on Biomedical Engineering*, vol. 67, no. 5, pp. 1517–1527, 2019.

[151] J. Li, B. E.-F. de Ávila, W. Gao, L. Zhang, and J. Wang, "Micro/nanorobots for biomedicine: Delivery, surgery, sensing, and detoxification," *Science Robotics*, vol. 2, no. 4, 2017.

[152] E. Diller, J. Giltinan, and M. Sitti, "Independent control of multiple magnetic microrobots in three dimensions," *The International Journal of Robotics Research*, vol. 32, no. 5, pp. 614–631, 2013.

[153] J. J. Abbott, E. Diller, and A. J. Petruska, "Magnetic methods in robotics," *Annual Review of Control, Robotics, and Autonomous Systems*, vol. 3, pp. 57–90, 2020.

[154] K. Villa, J. Viktorova, J. Plutnar, T. Ruml, L. Hoang, and M. Pumera, "Chemical microrobots as self-propelled microbrushes against dental biofilm," *Cell Reports Physical Science*, vol. 1, no. 9, p. 100181, 2020.

[155] R. L. Truby and S. Li, "Integrating chemical fuels and artificial muscles for untethered microrobots," *Science Robotics*, vol. 5, no. 45, 2020.

[156] A.-I. Bunea, D. Martella, S. Nocentini, C. Parmeggiani, R. Taboryski, and D. S. Wiersma, "Light-powered microrobots: Challenges and opportunities for hard and soft responsive microswimmers," *Advanced Intelligent Systems*, vol. 3, no. 4, p. 2000256, 2021.

[157] H. Zhou, C. C. Mayorga-Martinez, and M. Pumera, "Microplastic removal and degradation by mussel-inspired adhesive magnetic/enzymatic microrobots," *Small Methods*, p. 2100230, 2021.

[158] N. Läubli, N. Shamsudhin, D. Ahmed, and B. J. Nelson, "Controlled three-dimensional rotation of single cells using acoustic waves," *Procedia CIRP*, vol. 65, pp. 93–98, 2017.

[159] Q. Wang, L. Yang, J. Yu, P. W. Y. Chiu, Y.-P. Zheng, and L. Zhang, "Real-time magnetic navigation of a rotating colloidal microswarm

under ultrasound guidance," *IEEE Transactions on Biomedical Engineering*, vol. 67, no. 12, pp. 3403–3412, 2020.

[160] Y. Yan, W. Jing, and M. Mehrmohammadi, "Submillimeter magnetic microrobot tracking using an integrated ultrasound and photoacoustic imaging system," in *Proceedings of the IEEE International Ultrasonics Symposium (IUS)*, 2019, pp. 1057–1060.

[161] S. Lee, S. Lee, S. Kim, C.-H. Yoon, H.-J. Park, J.-y. Kim, and H. Choi, "Fabrication and characterization of a magnetic drilling actuator for navigation in a three-dimensional phantom vascular network," *Scientific Reports*, vol. 8, no. 1, pp. 1–9, 2018.

[162] S. Pane, M. Zhang, V. Iacovacci, L. Zhang, and A. Menciassi, "Contrast-enhanced ultrasound tracking of helical propellers with acoustic phase analysis and comparison with color doppler," *APL bioengineering*, vol. 6, no. 3, p. 036102, 2022.

[163] S. Pane, G. Faoro, E. Sinibaldi, V. Iacovacci, and A. Menciassi, "Ultrasound acoustic phase analysis enables robotic visual-servoing of magnetic microrobots," *IEEE Transactions on Robotics*, vol. 38, no. 3, pp. 1571–1582, 2022.

[164] S. Pane, V. Iacovacci, E. Sinibaldi, and A. Menciassi, "Real-time imaging and tracking of microrobots in tissues using ultrasound phase analysis," *Applied Physics Letters*, vol. 118, no. 1, p. 014102, 2021.

[165] L. Arcese, M. Fruchard, and A. Ferreira, "Adaptive controller and observer for a magnetic microrobot," *IEEE Transactions on Robotics*, vol. 29, no. 4, pp. 1060–1067, 2013.

[166] M. Salerno, G. Ciuti, G. Lucarini, R. Rizzo, P. Valdastri, A. Menciassi, A. Landi, and P. Dario, "A discrete-time localization method for capsule endoscopy based on on-board magnetic sensing," *Measurement Science and Technology*, vol. 23, no. 1, p. 015701, 2011.

[167] D. Son, S. Yim, and M. Sitti, "A 5-D localization method for a magnetically manipulated untethered robot using a 2-D array of hall-effect sensors," *IEEE/ASME Transactions on Mechatronics*, vol. 21, no. 2, pp. 708–716, 2015.

[168] S. Martel, O. Felfoul, J.-B. Mathieu, A. Chanu, S. Tamaz, M. Mohammadi, M. Mankiewicz, and N. Tabatabaei, "Mri-based medical nanorobotic platform for the control of magnetic nanoparticles and flagellated bacteria for target interventions in human capillaries," *The International Journal of Robotics Research*, vol. 28, no. 9, pp. 1169–1182, 2009.

[169] J. Leclerc, H. Zhao, and A. T. Becker, "3d control of rotating millimeter-scale swimmers through obstacles," in *Proceedings of the IEEE International Conference on Robotics and Automation (ICRA)*, 2019, pp. 8890–8896.

[170] Z. Han, Z. Liu, W. Kang, and W. He, "Boundary feedback control of a nonhomogeneous wind turbine tower with exogenous disturbances," *IEEE Transactions on Automatic Control*, vol. 67, no. 4, pp. 1952–1959, 2021.

[171] W. He, X. Tang, T. Wang, and Z. Liu, "Trajectory tracking control for a three-dimensional flexible wing," *IEEE Transactions on Control Systems Technology*, 2022.

[172] M. Arif, A. Moelker, and T. van Walsum, "Needle tip visibility in 3d ultrasound images," *Cardiovascular and Interventional Radiology*, vol. 41, no. 1, pp. 145–152, 2018.

[173] M. I. González, "Forces between permanent magnets: experiments and model," *European Journal of Physics*, vol. 38, no. 2, p. 025202, 2016.

[174] K. E. Peyer, L. Zhang, and B. J. Nelson, "Bio-inspired magnetic swimming microrobots for biomedical applications," *Nanoscale*, vol. 5, no. 4, pp. 1259–1272, 2013.

[175] C. Li, F. R. Halfwerk, J. Arens, S. Misra, M. Warlé, and I. S. M. Khalil, "Controlled helical propulsion against the flow of a physiological fluid," in *2022 International Conference on Manipulation, Automation and Robotics at Small Scales (MARSS)*. IEEE, 2022, pp. 1–6.

[176] Z. Zhang, A. Klingner, S. Misra, and I. S. M. Khalil, "Control of magnetically-driven screws in a viscoelastic medium," in *2020 IEEE/RSJ International Conference on Intelligent Robots and Systems (IROS)*. IEEE, 2020, pp. 2840–2846.

[177] J. Tokuda, G. S. Fischer, X. Papademetris, Z. Yaniv, L. Ibanez, P. Cheng, H. Liu, J. Blevins, J. Arata, A. J. Golby *et al.*, "Openigtlink: an open network protocol for image-guided therapy environment," *The International Journal of Medical Robotics and Computer Assisted Surgery*, vol. 5, no. 4, pp. 423–434, 2009.

[178] Z. Yang, L. Yang, M. Zhang, Q. Wang, S. C. H. Yu, and L. Zhang, "Magnetic control of a steerable guidewire under ultrasound guidance using mobile electromagnets," *IEEE Robotics and Automation Letters*, vol. 6, no. 2, pp. 1280–1287, 2021.

[179] M. Kaya, E. Senel, A. Ahmad, and O. Bebek, "Visual tracking of biopsy needles in 2d ultrasound images," in *2016 IEEE International Conference on Robotics and Automation (ICRA)*. IEEE, 2016, pp. 4386–4391.

[180] O. Akkus, A. Oguz, M. Uzunlulu, M. Kizilgul *et al.*, "Evaluation of skin and subcutaneous adipose tissue thickness for optimal insulin injection," *J. Diabetes Metabolism*, vol. 3, no. 8, p. 1000216, 2012.

[181] K. T. Nguyen, G. Go, Z. Jin, B. A. Darmawan, A. Yoo, S. Kim, M. Nan, S. B. Lee, B. Kang, C.-S. Kim *et al.*, "A magnetically guided self-rolled microrobot for targeted drug delivery, real-time x-ray imaging, and microrobot retrieval," *Advanced Healthcare Materials*, vol. 10, no. 6, p. 2001681, 2021.

[182] B. J. Nelson, S. Gervasoni, P. W. Chiu, L. Zhang, and A. Zemmar, "Magnetically actuated medical robots: an in vivo perspective," *Proceedings of the IEEE*, vol. 110, no. 7, pp. 1028–1037, 2022.

[183] Z. Hosseinidoust, B. Mostaghaci, O. Yasa, B.-W. Park, A. V. Singh, and M. Sitti, "Bioengineered and biohybrid bacteria-based systems for drug delivery," *Advanced drug delivery reviews*, vol. 106, pp. 27–44, 2016.

[184] M. Calik, H. Y. Ozkan, O. Ethemoglu, B. Koca, H. Kazanasmaz, N. Karacan, and D. S. Dokumaci, "The measurement of both carotid intima-media thickness and epicardial adipose tissue thickness in children with epilepsy receiving antiepileptic drug therapy," *Epilepsy & Behavior*, vol. 85, pp. 110–114, 2018.

[185] J. S. Catapano, F. A. Frisoli, G. M. Paisan, K. A. Dunn, A. Bajaj, M. A. Labib, T. S. Cole, M. J. Lang, and M. T. Lawton, "Subclavian artery to internal carotid artery interpositional bypass for carotid artery occlusion: Technical case report," *Operative Neurosurgery*, vol. 20, no. 1, pp. E66–E71, 2020.

[186] E. Bae and T. D. Vo, "Carotid artery angioplasty and stenting for atherosclerotic plaque with mobile intimal flap," *Annals of vascular surgery*, vol. 49, pp. 310–e1, 2018.

[187] L. Yang, M. Zhang, Z. Yang, and L. Zhang, "Multimode control of a parallel-mobile-coil system for adaptable large-workspace microrobotic actuation," *IEEE/ASME Transactions on Mechatronics*, 2022.

[188] C. Li, S. Misra, and I. S. M. Khalil, "Closed-loop control characterization of untethered small-scale helical device in physiological fluid with dynamic flow rates," *Advanced Intelligent Systems*, p. 2200322, 2022.

[189] M. Cai, Q. Wang, Z. Qi, D. Jin, X. Wu, T. Xu, and L. Zhang, "Deep reinforcement learning framework-based flow rate rejection control of soft magnetic miniature robots," *IEEE Transactions on Cybernetics*, 2022.

[190] Y. Lu, H. Zhao, A. T. Becker, and J. Leclerc, "Steering rotating magnetic swimmers in 2.5 dimensions using only 2d ultrasonography for position sensing," *IEEE Robotics and Automation Letters*, vol. 7, no. 2, pp. 3162–3169, 2022.

[191] J. Sa, J. Park, E. Jung, N. Kim, D. Lee, S. Bae, Y. Lee, and G. Jang, "Separable and recombinable magnetic robot for robotic endovascular intervention," *IEEE Robotics and Automation Letters*, vol. 8, no. 4, pp. 1881–1888, 2023.

[192] P. E. Dupont, B. J. Nelson, M. Goldfarb, B. Hannaford, A. Menciassi, M. K. O'Malley, N. Simaan, P. Valdastri, and G.-Z. Yang, "A decade retrospective of medical robotics research from 2010 to 2020," *Science Robotics*, vol. 6, no. 60, p. eabi8017, 2021.

[193] M. E. Alshafeei, A. Hosney, A. Klingner, S. Misra, and I. S. M. Khalil, "Magnetic-based motion control of a helical robot using two synchronized rotating dipole fields," in *5th IEEE RAS/EMBS International Conference on Biomedical Robotics and Biomechatronics*. IEEE, 2014, pp. 151–156.

[194] D. Mahdy, S. Hesham, M. Mansour, A. Mohamed, I. Basla, N. Hamdi, I. S. M. Khalil, and S. Misra, "Characterization of helical propulsion inside in vitro and ex vivo models of a rabbit aorta," in *2019 41st Annual International Conference of the IEEE Engineering in Medicine and Biology Society (EMBC)*. IEEE, 2019, pp. 5283–8286.

[195] L. Tan and D. J. Cappelleri, "Design, fabrication, and characterization of a helical adaptive multi-material microrobot (hammr)," *IEEE Robotics and Automation Letters*, vol. 8, no. 3, pp. 1723–1730, 2023.

[196] J. Liu, T. Xu, S. X. Yang, and X. Wu, "Navigation and visual feedback control for magnetically driven helical miniature swimmers," *IEEE Transactions on Industrial Informatics*, vol. 16, no. 1, pp. 477–487, 2019.

[197] H. Zhao, J. Leclerc, M. Feucht, O. Bailey, and A. T. Becker, "3d path-following using mrac on a millimeter-scale spiral-type magnetic robot," *IEEE Robotics and Automation Letters*, vol. 5, no. 2, pp. 1564–1571, 2020.

[198] J. De Ruijter, J. J. Muijsers, F. N. Van de Vosse, M. R. Van Sambeek, and R. G. Lopata, "A generalized approach for automatic 3-d geometry assessment of blood vessels in transverse ultrasound images using convolutional neural networks," *IEEE Transactions on Ultrasonics, Ferroelectrics, and Frequency Control*, vol. 68, no. 11, pp. 3326–3335, 2021.

[199] A. Carovac, F. Smajlovic, and D. Junuzovic, "Application of ultrasound in medicine," *Acta Informatica Medica*, vol. 19, no. 3, p. 168, 2011.

[200] D. Katritsis, L. Kaiktsis, A. Chaniotis, J. Pantos, E. P. Efstathopoulos, and V. Marmarelis, "Wall shear stress: theoretical considerations and methods of measurement," *Progress in cardiovascular diseases*, vol. 49, no. 5, pp. 307–329, 2007.

[201] D. Lopes, H. Puga, J. Teixeira, and R. Lima, "Blood flow simulations in patient-specific geometries of the carotid artery: A systematic review," *Journal of Biomechanics*, vol. 111, p. 110019, 2020.

[202] X. Hu, Y. Li, J. Li, and H. Chen, "Effects of altered blood flow induced by the muscle pump on thrombosis in a microfluidic venous valve model," *Lab on a Chip*, vol. 20, no. 14, pp. 2473–2481, 2020.

[203] R. O. Amenya, J. K. Sigey, G. M. O. Maloiy, and D. M. Theuri, "Effect of head position angles on the blood flow in the jugular vein of giraffes," 2021.

[204] S. Pane, V. Iacovacci, M. H. D. Ansari, and A. Menciassi, "Dynamic tracking of a magnetic micro-roller using ultrasound phase analysis," *Scientific reports*, vol. 11, no. 1, pp. 1–10, 2021.

[205] S. Merouche, L. Allard, E. Montagnon, G. Soulez, P. Bigras, and G. Cloutier, "A robotic ultrasound scanner for automatic vessel tracking and three-dimensional reconstruction of b-mode images," *IEEE transactions on ultrasonics, ferroelectrics, and frequency control*, vol. 63, no. 1, pp. 35–46, 2015.

[206] Z. Jiang, Z. Li, M. Grimm, M. Zhou, M. Esposito, W. Wein, W. Stechele, T. Wendler, and N. Navab, "Autonomous robotic screening of tubular structures based only on real-time ultrasound imaging feedback," *IEEE Transactions on Industrial Electronics*, vol. 69, no. 7, pp. 7064–7075, 2021.

[207] G. Faoro, S. Maglio, S. Pane, V. Iacovacci, and A. Menciassi, "An artificial intelligence-aided robotic platform for ultrasound-guided transcarotid revascularization," *IEEE Robotics and Automation Letters*, vol. 8, no. 4, pp. 2349–2356, 2023.

[208] J. Ni, J. Wu, J. Tong, Z. Chen, and J. Zhao, "Gc-net: Global context network for medical image segmentation," *Computer methods and programs in biomedicine*, vol. 190, p. 105121, 2020.

[209] C. G. Morales, J. Yao, T. Rane, R. Edman, H. Choset, and A. Dubrawski, "Reslicing ultrasound images for data augmentation and vessel reconstruction," in *2023 IEEE International Conference on Robotics and Automation (ICRA)*. IEEE, 2023, pp. 2710–2716.

[210] A. W. Mahoney, N. D. Nelson, K. E. Peyer, B. J. Nelson, and J. J. Abbott, "Behavior of rotating magnetic microrobots above the step-out frequency with application to control of multi-microrobot systems," *Applied Physics Letters*, vol. 104, no. 14, 2014.

[211] X. Wang, C. Hu, L. Schurz, C. De Marco, X. Chen, S. Pané, and B. J. Nelson, "Surface-chemistry-mediated control of individual magnetic helical microswimmers in a swarm," *ACS nano*, vol. 12, no. 6, pp. 6210–6217, 2018.

[212] A. Halder and Y. Sun, "Biocompatible propulsion for biomedical micro/nano robotics," *Biosensors and Bioelectronics*, vol. 139, p. 111334, 2019.

[213] J. Park, C. Jin, S. Lee, J.-Y. Kim, and H. Choi, "Magnetically actuated degradable microrobots for actively controlled drug release and hyperthermia therapy," *Advanced healthcare materials*, vol. 8, no. 16, p. 1900213, 2019.

[214] Y. Hou, H. Wang, S. Zhong, Y. Qiu, Q. Shi, T. Sun, Q. Huang, and T. Fukuda, "Design and control of a surface-dimple-optimized helical microdrill for motions in high-viscosity fluids," *IEEE/ASME Transactions on Mechatronics*, vol. 28, no. 1, pp. 429–439, 2022.

[215] P. L. Venugopalan, R. Sai, Y. Chandorkar, B. Basu, S. Shivashankar, and A. Ghosh, "Conformal cytocompatible ferrite coatings facilitate the realization of a nanovoyager in human blood," *Nano letters*, vol. 14, no. 4, pp. 1968–1975, 2014.

[216] M. Pal, N. Somalwar, A. Singh, R. Bhat, S. M. Eswarappa, D. K. Saini, and A. Ghosh, "Maneuverability of magnetic nanomotors in-

side living cells," *Advanced Materials*, vol. 30, no. 22, p. 1800429, 2018.

[217] Z. Wang, Q. Li, P. Cao, J. Zhang, D. Wu, R. Xu, Y. Zhang, Y. Xu, T. Liang, W. Chen *et al.*, "A biomimetic helical robot actuated by rotating magnetic field for targeted navigation and in situ prodrug activation to treat intestinal diseases," *Device*, vol. 1, no. 3, 2023.

Acknowledgements

As I sit down to write this part, I'm already coming to terms with the fact that my wonderful time in the Netherlands is drawing to a close. In the past four-plus years, there have been so many wonderful memories that are worth cherishing.

About the author

Chuang Li was born on 15^{th} December 1992 in Liaoning province, China. He obtained his undergraduate degree in Communication Engineering, Bohai University, Jinzhou, Liaoning Province, China, in 2016. In the same year, he joined the College of Control Science and Engineering of Bohai University to study control science and engineering and obtained his master's degree in 2019. From September 2017 to September 2018, he was a visiting researcher studying control science and engineering at the Research Institute of Intelligent Control and Systems, School of Astronautics, Harbin Institute of Technology, Harbin, Heilongjiang Province, China. During his master, his research interests include nonlinear control system, adaptive control theory, and aircraft control.

In November 2019, he commenced his doctoral studies in the Surgical Robotics Laboratory at the Department of Biomedical Engineering, University of Groningen and University Medical Center Groningen, Groningen, the Netherlands, under the supervision of Prof. Dr. Sarthak Misra and Dr. Islam S. M. Khalil. His doctoral research centered on the modeling and motion control of untethered small-scale helical devices inside the vascular network model based on ultrasound guidance.